Laboratory For Atmospheric and Space Physics

LASP Engineering Division

University of Colorado

Boulder, Colorado

LASP Engineering

JSC-1a Geotechnical Properties Experiments

Tons 1, 2, 3

Document No. 105525

Approver's List

Prepared By	Haydar Arslan, Geotechnical Engineer
Approved By	Susan Batiste, Project Manager
Configuration Management	

Revision History

Rev	ECO #	Change Description	By	Initiation Date
A	C01446	Initial Release	Batiste	10-04-2007

Table of Contents

Introduction

Geotechnical engineering properties of the lunar soil simulant designated JSC-1A have been investigated experimentally. To better understand these soil properties, a variety of conventional and unconventional experiments were conducted on JSC-1A to determine its grain size distribution, cohesion, friction angle, dilatancy angle, tensile strength, and appropriate low strain elastic constants. These experiments were conducted on JSC-1A at a variety of densities prepared through tamping densification to quantify the response of the soil over a range of conditions.

Scott (1968 and 1969) equated walking on the Moon with the sensation one would have when walking on a trampoline. While the lunar surface in most locations is actually relatively firm the low gravity gives the impression that the surface is more flexible or compliant than it actually is. Impact crater rims and their vicinities seem to be the only locations where soft and unconsolidated regolith exists in abundance. Extensive measurements of surface and subsurface in-situ properties were made during the Apollo era. There are three Programs which have provided lunar samples for study on Earth: Luna, Surveyor, and Apollo.

Prior to 1969, when 13 kg of regolith fines were returned on Apollo 11, no lunar regolith was available to model a simulant after. Apollo missions brought back a total of approximately 115 kg of regolith by the end of 1972, and Luna missions brought back 321 g between 1970 and 1976. While these samples remain extremely significant, this is not sufficient for performing complete soil mechanics studies. Instead, the returned samples were used to evaluate physical, chemical, and limited geotechnical properties. That information was then used to select terrestrial soils, which would sufficiently mimic the lunar regolith. Data on tensile strength for lunar soil and key variables and parameters that affect the tensile strength are very limited.

Simulants with sufficiently accurate geotechnical properties are needed for the research and engineering of future lunar operations including spacecraft landing, mobility, construction, mining and resource utilization, and foundation design. Results of investigations can be used to assess hazards such as landslides and compressible soils for future landing site selection and to provide engineering input for the design of Moon landing vehicles, lunar rovers, sampling devices, and other equipment. The rovers planned for future missions have increased capability to travel further from the landing site and into more diverse terrain. The evaluation of soil mechanical properties of regolith simulant is of increased importance for these long distance or duration excursions.

1 Experimental Procedures

1.1 Grain Size Distribution

The major component of soil strength and deformability is derived from interparticle friction at particle contacts. These properties are highly dependent on the size, texture, and orientation of contacts. For cohesionless soils the density and grain size distribution are most indicative of behavior; variation in the soil's fabric leads to variations in the engineering properties of soil. A small amount of difference in grain size distribution can lead to a difference in shear behavior of soils. For instance, volumetric and deviatoric modulus properties as well as strength can vary significantly due to different grain size distributions.

Grain size distribution analyses are made not only to determine the size of the individual grains in soil, but also to determine the relative distribution of the sizes. The grain size distribution curve indicates the range of the size of particles present in a soil, and its shape can be used to indicate density. A uniform soil, one consisting of particles with a very narrow range in sizes, is liable to be loose. A well graded soil, on the other hand, tends to be dense and can be compacted even more with mechanical equipment (*Eden, 1963*).

The shear strength dependance on grain size distribution of soil has been shown by many researchers. Hayashi et al. (1992) developed a stress-strain curve relation with a hyperbola whose shape depends on a parameter which is function of the grain size distribution characteristics. They developed their model based on shear stress-strain curves obtained in a simple shear soil testing device. Subhash et al. (1991) and Tatsuoka (2000), showed grain size distribution curves affect the inherent anisotropy on the stress-strain properties of soil. They have illustrated the effects of inherent anisotropy on the angle of internal friction in plane strain compression of air-pluviated samples of sands. It was shown that having different grain size distribution curves leads to different peak stress.

1.1.1 Procedure for Grain Size Distribution Analysis

Grain size distribution JSC-1A was performed according to ASTM D422 (ASTM 1995a and 1995b) for particles greater than 0.075 mm in diameter (greater than the No. 200 sieve). The test procedure can be summarized as:

1. The mass of individual sieves and collection pan were recorded.

2. Sieves were stacked together with the largest-opening sieve (No. 4) at the top, with sieves of progressively smaller openings below (to No. 200), and a collection pan at the very bottom of the stack. The sieves used are as follows:

Sieve Number	Opening, mm
4	4.75
10	2.00
20	0.850
40	0.425
50	0.300
60	0.246
80	0.177
100	0.150
140	0.106
200	0.075

3. The entire soil sample was poured into the top of the sieve stack and a cover was placed tightly over top.
4. The sieve stack was shaken by hand for ten minutes.
5. Starting from the top and working downward, each sieve, with soil remaining on the sieve, was weighed and recorded in order to determine the amount of soil retained on each sieve.

Calculations are as follows:

1. The percent of soil retained on nth sieve is calculated:
   R_n = (Mass retained on sieve)*100/(Total sample mass)
2. Cumulative percent of soil retained on n_{th} sieve = $\sum_{i=1}^{n} R_n$
3. Cumulative percent passing through the nth sieves:
   Percent finer = 100% - $\sum_{i=1}^{n} R_n$

As a preliminary check, the mass retained on all sieves and bottom pan are summed and compared to the initial sample mass. According to ASTM D422 (ASTM 1995a and 1995b), the lost of mass should be within 1%. Table xx shows that mass loss of the sample was well within the allowed amount according to ASTM D422.

1.2 Strength and Volume Change Characteristics

Strength and volume change characteristics are key to understanding and predicting the mechanical behavior of the regolith simulant. The conventional triaxial compression test was used to evaluate the shear behavior of JSC-1A. The parameters that were found using the tests were apparent cohesion, friction angle, dilatancy, and Young's modulus. Apparent cohesion and friction angle are used in this case to compare with lunar regolith and earlier regolith simulants. If these two properties are similar, the material will behave similarly in situations such as engineering methods for estimating slope stability, bearing capacity, requirements for storage and excavation tools, and mobility design.

1.2.1 Triaxial Compression Experiment Sample Preparation

The triaxial test system, developed by Alshibli (1995), consisted of a standard Brainard-Kilman triaxial test cell, a standard loading frame, a fluid system comprised of pipes, connections and pressure reservoirs, controlled by air pressure regulators, and a control and data collection system (Figure 1). A Brainard Kilman 5600 Load Frame was used to compress the specimens, and a 5600 Electronics Module provided a user interface to control the displacement distance and rate. A linear voltage differential transducer (LVDT) hardmounted on the load frame recorded the axial displacement of the top test cell endcap. The confining pressure was controlled by an air regulator connected to a house air pressure supply, using a dial gauge for first order approximation setting. The regulated air was then routed to a sealed cylindrical Plexiglas pressure reservoir partially filled with water, which was connected by plastic pipes to a differential pressure transducer, with one side open to the atmosphere. This was used for fine pressure reading and was connected to the test cell which provided confining pressure to the specimen. The reservoir was divided into two sections, each connected to the test cell line, but with valves to open or close the connection. During experimentation, only one section of the reservoir remained open to the test cell, and allowed water to be provided to or collected from the cell as the volume decreased or measure the change in pressure between the two sides, and thus the change in height, which was then converted to volume, of the reservoir side open to the test cell. As the system worked by allowing the height of water in the reservoir to change in order to measure volume changes, the system did allow the confining pressure in the test cell to increase or decrease slightly (up to 1.75 kPa, or 0.25 psi) as the volume of the specimen increases or decreases, respectively.

A S-type load cell was used to measure the load on the specimen. The LVDT, differential pressure transducers, and load cell measurements were all recorded with the aid of a data collection system. All instruments were powered by a 2-channel power source providing both 10

and 15 V DC. Sensor data were routed through a multi-channel multimeter to a desktop Macintosh computer equipped with LabVIEW software, which converted voltage into engineering units, displayed data real-time, and saved both voltage and scaled data. An extensive discussion on the development of the system is discussed by Klosky (1997).

Sample preparation is described below. Figure 1, Figure 2, and Figure 3 show a series of images to further indicate the method.

Specimens tested were cylindrical in shape, 74.6 mm in diameter by 150 mm (Figure 1). In order to prepare a sand specimen for testing, a latex membrane was first folded around a six-piece mold with internal dimensions the size of the sample as stated above, with a small vacuum placed on the mold to assure the latex membrane conformed with the mold. This was then secured onto the bottom platen of the test cell.

Individual specimens were prepared dry in three lifts by compaction with drop hammer furnished with a 38 mm diameter circular tamping foot (Figure 2). The mass of soil needed to achieve the desired density was divided evenly into three portions. The first portion was place inside the mold, and tamped with the drop hammer. To use the hammer, the tamping foot is placed on the soil surface and the mass lifted to the top stop and dropped, landing on the bottom stop. This would be repeated, moving the tamping foot across the surface of the sample. For example, a 1000 g mass was dropped 5 times from a distance of 254 mm on the soil per lift to produce a density of 1.7 g/cm^3. It is recognized that preparation by tamping with the irregularly shaped particles of JSC-1A particles results in specimens that are neither perfectly homogeneous nor uniform. This results in some local instabilities causing some differences for the response of specimens to loading.

After the simulant was placed and leveled at the upper surface using a straightedge, the upper, exposed area of the membrane was cleaned to remove any particles, which may puncture the membrane or allow water through the seal. The top platen was placed over the sample. The membrane which was folded outside the mold was then folded up over the top platen and a seal was created with o-rings placed over and around the platen and membrane. The assembly was then cleaned and weighed.

Next, a small amount of vacuum was applied to the pore space inside the specimen, and the mold was removed. Six to twelve diameter measurements were then taken and averaged for the purpose of computing the volume and density of the specimen prepared. Once calculations confirmed that specimen preparation was satisfactory, the test cell's assembly was completed by

placing the polycarbonate sleeve and top plate, sealing the cell by placing the three external tension rods. The cell was then filled with water and pressurized it to the test pressure. The vacuum was then removed from the internal pore space, leaving the sample open to the atmosphere.

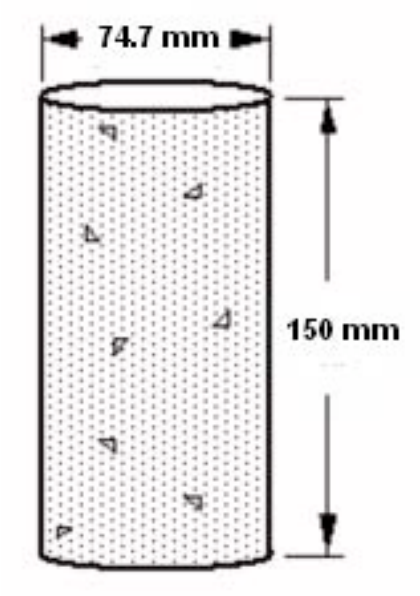

Figure 1. Triaxial Specimen Configuration

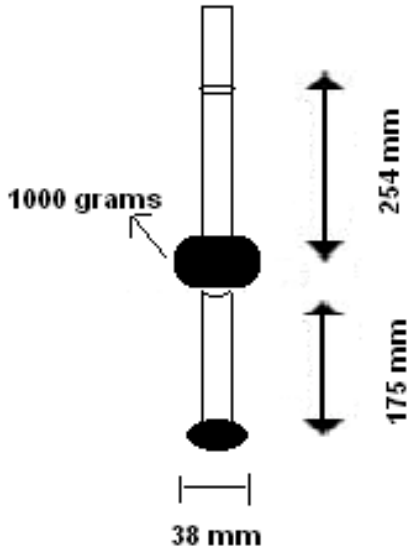

Figure 2. Compaction hammer configuration

Figure 3. Test Cell Preparation. The following 3 pages, 9 steps, show the basic method used to prepare a triaxial experiment specimen.

1) A plexiglass mold is used to support the latex membrane in its cylindrical test shape. The mold splits in half for easy removal later.

2) Membrane place in mold. A vacuum line is placed on mold to hold latex snug to the inside of the mold.

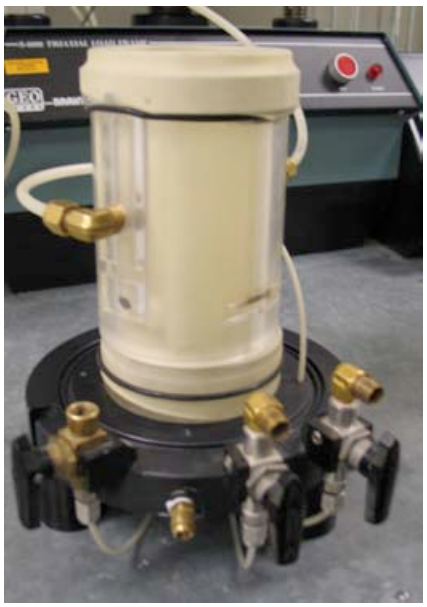

3) The mold with membrane is attached to the base of the test cell. The lower portion of the membrane is wrapped around the end platen on the base plate, and sealed with an o-ring.

4) The simulant is then place in the mold. This is done in 3 batches, or lifts. First, 1/3 of the material is placed in the mold (right) and then it is tamped (left). This is repeated until the third lift placed and tamped.

5) Once all three lifts are placed, the top of the material is assured flat with a straight edge and all surfaces are cleaned, paying particular attention to the latex membrane.

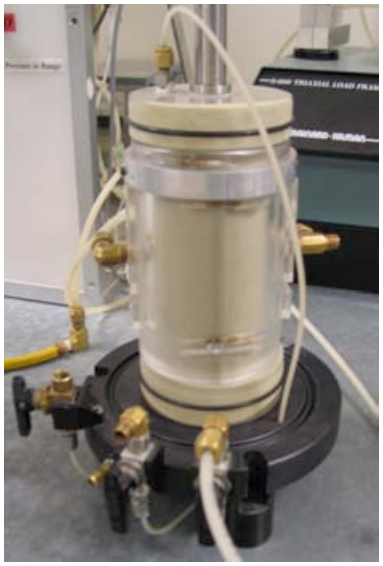

6) The top loading platen is then placed on the mold/sample. The membrane is folded up around the platen and sealed with an o-ring. A vacuum line is attached to the sample.

7) With the vacuum line attached, the mold is then removed.

8) The rest of the test cell is assembled (cylindrical water jacket, tie rods, upper plate) and the space between the specimen and the water jacket is filled with water and pressurized. The vacuum internal to the specimen is then removed (pore space is left open to the atmosphere, at gauge pressure), with the surrounding water left to support the specimen.

9) The test cell is then placed on the load frame, connected with measurement apparatuses and the experiment is started.

1.2.2 Triaxial Compression Experimental Procedure

The triaxial tests were conducted with a standard triaxial cell and loading frame using displacement control. Monotonic loading was performed at 0.0197 in/hour, up to a maximum of 25% axial strain. Confining stress was controlled at 15, 30 and 60 kPa. Bishop and Henkel (1962) have discussed in detail the general design and function of the triaxial apparatus.

The triaxial equipment' consisted of a standard loading frame, a fluid system comprised of pipes, connections and pressure reservoirs, controlled by air pressure regulators, and a control and data collection system. A Brainard Kilman 5600 Load Frame was used to compress the specimens, and a 5600 Electronics Module provided a user interface to control the displacement distance and rate. A linear voltage differential transducer (LVDT) hardmounted on the load frame recorded the axial displacement of the top test cell endcap. The confining pressure was controlled by an air regulator connected to a house air pressure supply, using a dial gauge for first order approximation setting. The regulated air was then routed to a sealed cylindrical Plexiglas pressure reservoir partially filled with water, which was connected by plastic pipes to a differential pressure transducer, with one side open to the atmosphere. This was used for fine pressure reading and was connected to the test cell which provided confining pressure to the specimen. The reservoir was divided into two sections, each connected to the test cell line, but with valves to open or close the connection. During experimentation, only one section of the reservoir remained open to the test cell, and allowed water to be provided to or collected from the cell as the volume changes. A differential pressure transducer was used to measure the change in pressure between the two sides, and thus the change in height, which was then converted to volume, of the reservoir side open to the test cell. As the system worked by allowing the height of water in the reservoir to change in order to measure volume changes, the system did allow the confining pressure in the test cell to increase or decrease slightly (up to 1.75 kPa, or 0.25 psi) as the volume of the specimen increases or decreases, respectively.

A load cell having a range of ± 890 N (± 250 lb.) and an adjustable gain was used to measure the load on the specimen. The LVDT, differential pressure transducers, and load cell measurements were all recorded with the aid of a data collection system. All instruments were powered by a 2-channel power source providing both 10 and 15 V DC. Sensor data were routed through a multi-channel multimeter to a desktop Macintosh computer equipped with LabVIEW software, which converted voltage into engineering units, displayed data real-time, and saved both voltage and scaled data.

1.3 Tensile Stress Characteristics

As Figure 4 illustrates, yield surface is defined by the tensile strength (T), cohesion (*C*) and friction angle (*Φ*) of the soil. In spite of the fact that the importance of tensile strength, it is generally either ignored or not given so much attention in geotechnical engineering. The purpose of the experiments was to obtain the tensile strength of lunar regolith simulant, and examine the variation as a function of density and height of the specimen. The experiments were conducted by using a direct tension device as shown in Figure 5. The direct tension device was built by Kim (2001) modified in this study to be able to investigate the tensile strength properties of JSC-1.

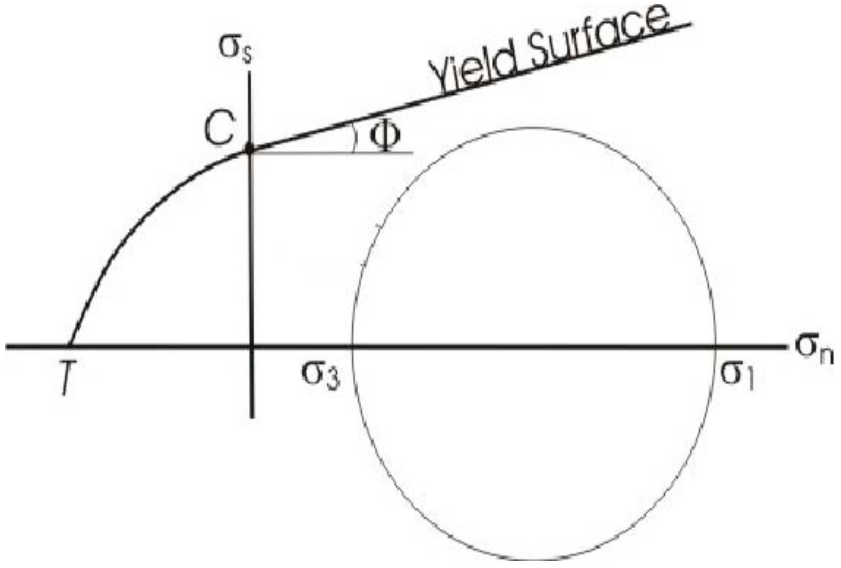

Figure 4. Yield surface definition in Mohr-Coulomb failure criteria

The specimen container (178-178-178 mm) is split into two equal halves. Inside the container, four triangular wedges were attached in order to facilitate contact between the specimen and container as tension is developed across the plane of separation. The wedges were provided with beveled angles larger than the dilatancy angle of the material to reduce movement of the soil particles relative to the container (when the specimen was split into two halves) and to achieve a uniform stress distribution on the plane of separation (Figure 5).

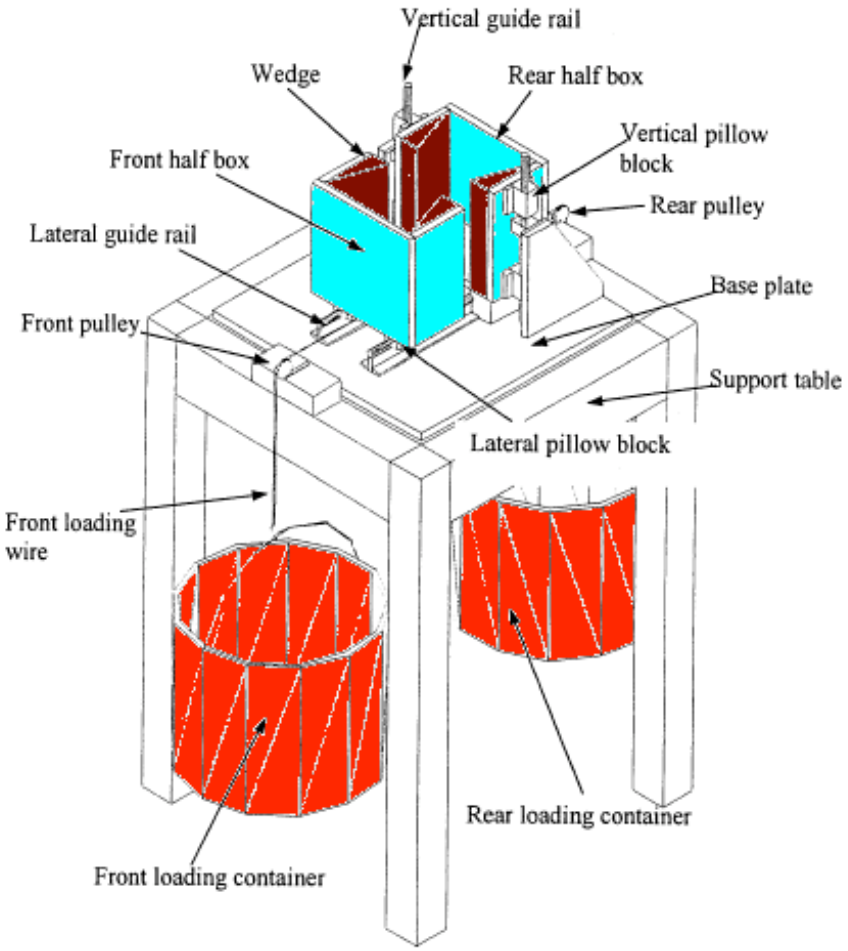

Figure 5.Direct tension apparatus.

1.3.1 Direct Tension Experimental Sample Preparation

The container consisting of two halves, a sliding front and stationary rear compartment was first tightly taped to prevent the movement of the container assembly during compaction. Individual specimens were prepared in three lifts within the container box by tamping with a drop hammer furnished with an angular foot, which facilitates compaction in corner regions (Figure 6). To achieve uniform specimen densities, the number of blows, the weight of the hammer and the drop height were controlled. For loose specimens, number of drops per layer was five and for denser specimen the number was twenty. No vibration has been applied to prepare the specimen. The test is conducted without any surcharge load or confinement.

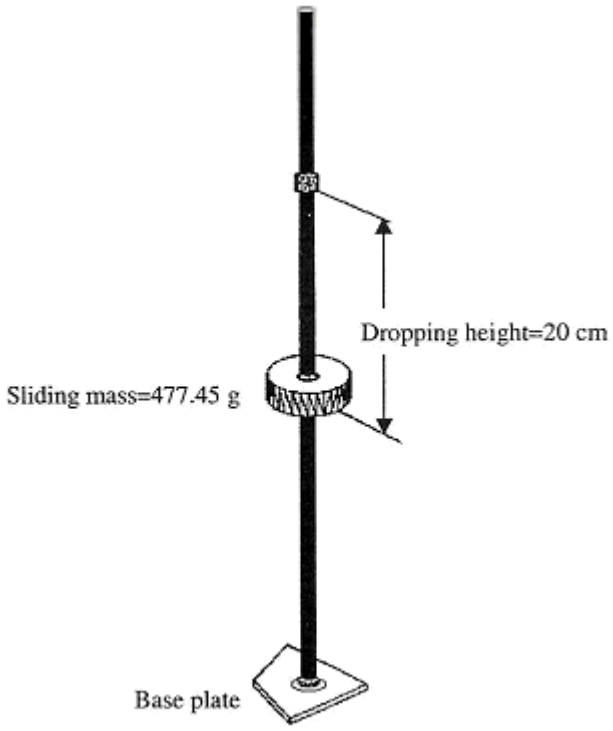

Figure 6. Illustration of tamping device

1.3.2 Direct Tension Experimental Procedure

Following preparation, immediately before the experiment was begun, the tape which secured the two halves of the container in place were cut with a sharp blade. A tensile load on the sample was then steadily applied by introducing small amounts of water in the front loading container until failure occurred. Careful measurements of the empty apparatus found that about 120 gram was necessary to overcome the friction in the apparatus itself, and this was subtracted from the applied tensile load after testing to correct for this. Variations in apparatus friction were small, and given the magnitude of the total measured failure load, potential variations in friction within the device itself could be expected to be quite small. This somewhat simple loading procedure provided good results, and proved to be highly repeatable.

2 Test Results

2.1 Grain Size Distribution

Sieve analysis was performed on Tons 1, 2, and 3 of JSC-1a. Three samples were tested from each ton. Results are tabulated in Table 1 through Table 3, and show that the mass loss during testing was well below the 1% acceptable value.

Graphical results of the sieve analysis for one sample from each of the three tons and the comparison of grain size distribution for JSC-1A simulant and lunar regolith is shown in Figure 7. As the figure shows, the results are very consistent among the three batches. The grain size distribution of lunar soil regolith was reported by Carrier et al. (1973), and is illustrated with upper and lower curves representing the range of grain size distributions found among the tested samples. As can be seen, JSC-1a falls inside the upper and lower bound curves at sizes greater than 0.075 mm. It is highly important that a lunar simulant have a grain size distribution similar to that of the lunar regolith itself. These test results indicate that this property has been achieved.

Figure 8 compares the grain size distribution of JSC-1a and JSC-1 tests conducted by Willman et al. (1995) and Klosky (1997). Though similar, the curves are not the same and will result in some variation in soil behavior from a geotechnical engineering perspective. The JSC-1A gradation is very similar to JSC-1 as measured by Willman et al for grain sizes 0.15 mm and greater, but then diverges, with the JSC-1a material showing a greater amount of fine particles.

It is noted that measurements of grain size distribution does not include particles below 0.063 mm in size. The reader is referred to USGS data using a Coluter LS seriesw laser diffraction particle size analyzer. These results were used in combination with sieve analysis data to derive the coefficient of curvature and coefficient of uniformity, shown in Table 4.

Table 1. Ton 1 sieve results.

Sieve Number	Opening, mm	Percent Passing		
		Sample 1	Sample 2	Sample 3
4	4.75	100	100	100
10	2.00	100	100	100
20	0.850	98.7	98.7	98.7
40	0.425	91.6	91.4	91.6
50	0.300	84.7	84.4	84.5
60	0.246	80.3	79.9	80.2
80	0.177	72.3	70.9	71.8
100	0.150	63.0	61.8	62.6
140	0.106	51.8	52.0	51.5
200	0.075	38.8	38.4	39.9
Percent mass lost:		0.3%	0.2%	0.2%

Table 2. Ton 2 sieve results.

Sieve Number	Opening, mm	Percent Passing		
		Sample 1	Sample 2	Sample 3
4	4.75	100	100	100
10	2.00	100	100	100
20	0.850	98.6	98.7	98.7
40	0.425	90.6	90.8	91.0
50	0.300	83.5	83.8	83.9
60	0.246	79.7	79.8	79.9
80	0.177	72.0	72.6	72.5
100	0.150	64.4	63.4	64.8
140	0.106	54.2	53.7	54.7
200	0.075	41.6	41.4	41.9
Percent mass lost:		0.2%	0.3%	0.3%

Table 3. Ton 3 sieve results.

Sieve Number	Opening, mm	Percent Passing		
		Sample 1	Sample 2	Sample 3
4	4.75	100	100	100
10	2.00	100	100	100
20	0.850	98.9	98.9	99.0
40	0.425	92.6	92.6	92.5
50	0.300	85.6	85.5	85.1
60	0.246	81.0	81.1	80.8
80	0.177	72.4	72.6	72.2
100	0.150	64.0	63.6	62.9
140	0.106	53.1	52.1	52.2
200	0.075	41.0	38.4	39.1
Percent mass lost:		0.2%	0.2%	0.2%

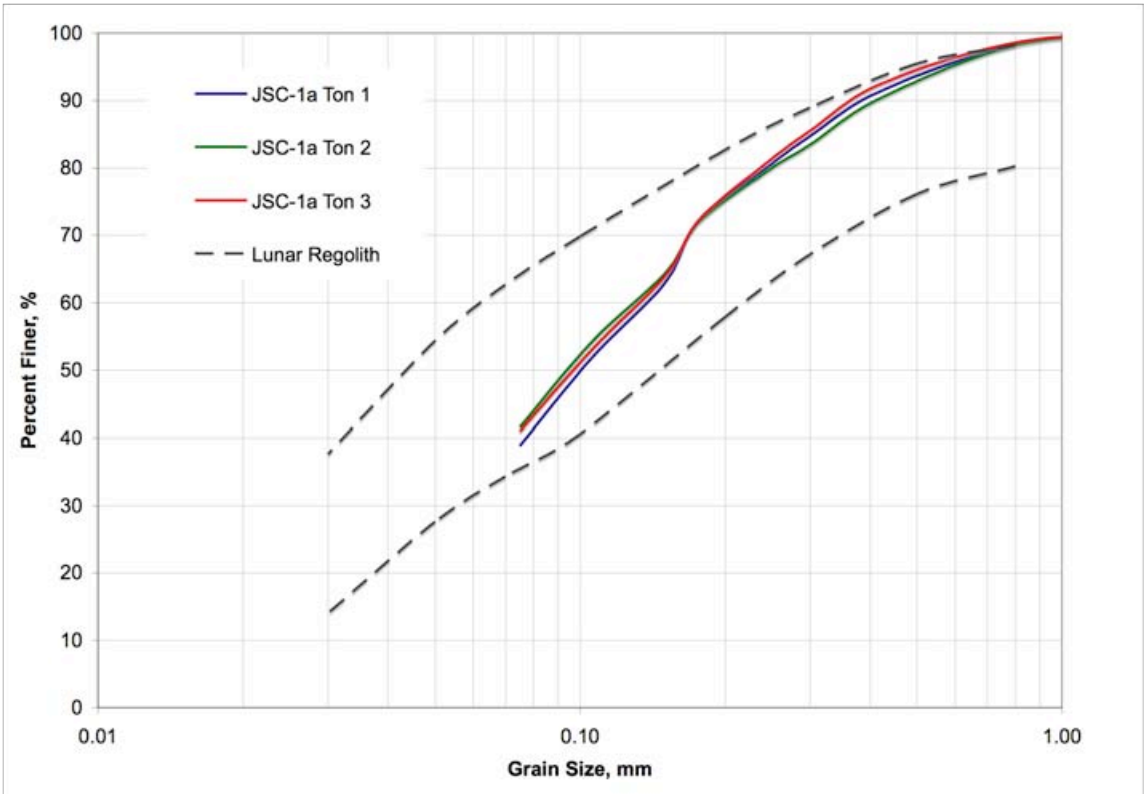

Figure 7. Grain size distribution of JSC-1A Tone 1, 2, and 3. Comparison with upper and lower bounds of lunar regolith (Carrier et al. 1973) is provided.

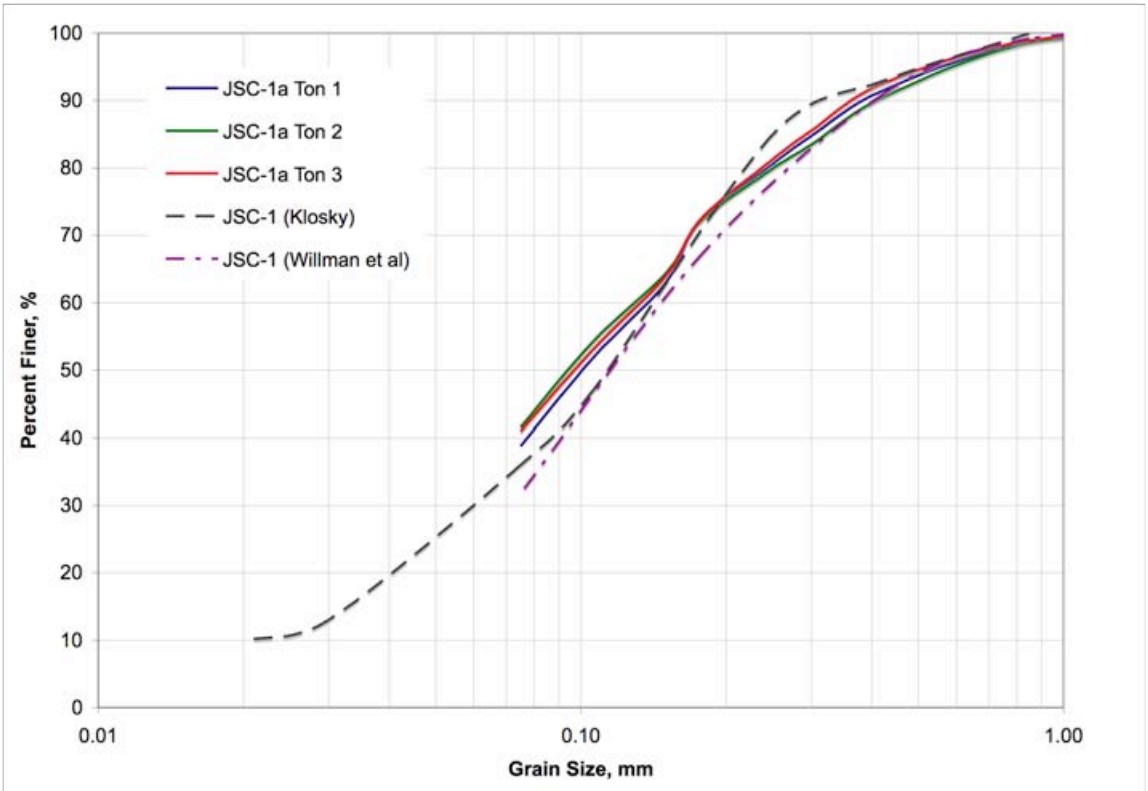

Figure 8. Comparison of grain size distribution of JSC-1A Tons 1, 2 and 3. sample grain size distributions with JSC-1 lunar soil simulant (Willman et al. 1995, Klosky 1997).

Table 4. Key parameters of the particle size distribution curve. Data provided by USGS laser diffraction measurements were used to provide d_{30} and d_{10} values.

Coefficient of uniformity	$Cu=D_{60}/D_{10}$	6.85
Coefficient of curvature	$Cz=D_{30}^2/D_{60}D_{10}$	1.06
Particle size such that 60% of the particles are smaller	D_{60}, mm	0.137
Particle size such that 50% of the particles are smaller	D_{50}, mm	0.100
Particle size such that 30% of the particles are smaller	D_{30}, mm	0.054
Effective size, mm	D_{10}, mm	0.020

2.2 Triaxial Experiments

Experimental data and results of triaxial testing for characterization of stress-strain and volumetric behavior of JSC-1A samples of 1.7, 1.8, and 1.9 g/cm^3 at 15, 30 and 60 kPa confinements are summarized in Table 5 to Table 8. Mohr's circle to determine combined friction and effective cohesion of JSC-1A samples are shown in Figure 9 to Figure 11. Individual experiment results are included as Appendix A, B and C.

The stress ratio data are used to find shear strength parameters cohesion and friction. The maximum stress during an experiment is found and entered into the Mohr-Coulomb model with the confining stress, represented as a Mohr's circle. Performing experiments at multiple confining stresses provides data to allow fitting a line tangent to the Mohr's circles. The angle of the line is equal to the friction angle of the material, and the point where the fit line crosses the y-axis is the cohesion parameter. Figures 8 to 10 show the fit of the triaxial experiments to the Mohr-Coulomb model. From these data, it is determined that the average internal friction angle of the JSC-1A and the average cohesion is 1.4 kPa and the friction angle is 42.9º for the density of 1.7g/cm^3; and the average cohesion is 1.8 kPa and the friction angle is 44.5º for the density of 1.8 g/cm^3; and the average cohesion is 2.4 kPa and the friction angle is 48.8º for the density of 1.9 g/cm^3. When testing, it was found that the strength of the material, measured by stress ratios on single tests declined some during testing, and the values reported are for the material following a small number of triaxial tests (≈2-4) at 60 kPa confining stress. This decline in strength is related to the working of the soil, where some of the small, sharp edges will break off, reducing the strength of the soil.

The cohesions and friction angles are a reasonable value for a lunar soil simulant (Perkins, 1991; McKay, 1994; Klosky, 1996) and indicate the particulates are probably sufficiently angular, thus the basic method used to create the material is probably acceptable. Perkins (1991), McKay (1994), Klosky (1996) found friction angles between 45-55°.

Table 5. Summary of triaxial experiments performed on samples at 1.7 g/cc density. Friction angles reported in this table are derived from individual experiments, assuming zero cohesion.

Test Name*	Date Performed	Ton batch of sample	Density (ρ), g/cm^3	Maximum Friction Angle				E_{tan}, MPa	Dilatancy Angle (ψ), deg	Residual Friction Angle	
				Friction Angle (ϕ_{max}), c=0	Axial Strain, ε_{ax}	σ_1	σ_3			Friction Angle, (ϕ_{res}), c=0	Axial Strain, ε_{ax}
J1A_15_17A	11/16/2006	1	1.69	43.6	0.028	83.2	15.3	12.4	*22.3*	35.6	0.15
J1A_15_17B	11/21/2006	1	1.68	40.2	0.031	71.0	15.3	15.4	18.0	35.2	0.15
J1A_15_17C	11/22/2006	1	1.69	41.4	0.034	74.2	15.1	9.4	11.0	n/a	n/a
J1A_15_17D	11/22/2006	1	1.69	39.2	0.027	67.7	15.3	10.3	18.7	32.6	0.15
J1A_15_17E	11/26/2006	1	1.69	43.4	0.029	80.7	14.9	12.9	18.2	34.2	0.15
J1A_15_17F	11/29/2006	1	1.69	44.0	0.033	84.4	15.2	9.9	18.5	34.9	0.15
J1A_15_17G	03/05/2007	2	1.71	43.4	0.034	81.3	15.1	10.0	12.2	34.6	0.15
J1A_15_17H	04/09/2007	3	1.72	42.5	0.032	77.4	15.0	9.3	12.8	34.6	0.15
J1A_15_17I	04/19/2007	3	1.71	38.1	0.030	63.1	14.9	8.9	*10.1*	32.6	0.15
AVERAGE			**1.70**	**41.8**			**15.1**	**10.9**	**15.6**	**34.3**	
J1A_30_17A	02/16/2007	1	1.71	41.1	0.044	147.0	30.3	18.7	6.8	35.0	0.15
J1A_30_17B	02/22/2007	1	1.70	41.0	0.040	144.6	30.0	15.1	11.4	34.9	0.15
J1A_30_17C	03/06/2007	2	1.71	*45.0*	0.032	175.3	30.1	*6.7*	12.0	36.5	0.15
J1A_30_17D	04/09/2007	3	1.72	41.7	0.033	149.2	30.0	15.0	10.4	35.8	0.15
J1A_30_17E	04/20/2007	3	1.72	42.1	0.032	151.5	29.9	15.8	7.1	37.7	0.15
AVERAGE			**1.71**	**41.5**			**30.1**	**16.2**	**9.5**	**36.0**	
J1A_60_17A	02/13/2007	1	1.70	43.0	0.047	317.3	60.0	15.4	9.7	36.5	0.15
J1A_60_17B	02/15/2007	1	1.70	43.5	0.044	325.7	60.0	*21.4*	12.0	37.8	0.15
J1A_60_17C	03/08/2007	2	1.71	44.6	0.034	341.7	59.8	15.6	*5.7*	38.7	0.15
J1A_60_17D	04/10/2007	3	1.72	42.1	0.044	304.3	60.0	13.9	9.9	36.7	0.15
AVERAGE			**1.71**	**43.3**			**60.0**	**15.0**	**8.4**	**37.4**	

*Experiment Name Coding: J1A_xx_yyZ ("J1A": Indicates test material, JSC-1A)

xx: Indicates nominal test pressure in kPa

yy: Indicates nominal initial density in g/cm^3*10. "17"= 1.7 g/cc, "18" = 1.8 g/cc, "19" = 1.9 g/cc

Z: Used to distinguish between experiments of same material, pressure and density

Table 6. Summary of triaxial experiments performed on samples at 1.8 g/cc density. Friction angles reported in this table are derived from individual experiments, assuming zero cohesion.

Test Name*	Date Performed	Ton batch of sample	Density (ρ), g/cm^3	Maximum Friction Angle				E_{tan}, MPa	Dilatancy Angle (ψ), deg	Residual Friction Angle	
				Friction Angle (ϕ_{max}), c=0	E_{tan}, MPa	σ_1	σ_3			Friction Angle, (ϕ_{res})	Axial Strain, ε_{ax}
J1A_15_18A	12/05/2006	1	1.78	47.3	0.027	99.8	15.3	15.5	20.9	38.5	0.09
J1A_15_18B	12/05/2006	1	1.78	44.9	0.023	87.4	15.1	14.8	20.8	35.5	0.15
J1A_15_18D	03/21/2007	3	1.78	*53.0*	0.036	133.9	*15.0*	*17.3*	*17.0*	*40.2*	0.15
J1A_15_18E	04/11/2007	3	1.78	45.3	0.036	89.7	15.1	12.4	*13.5*	37.1	0.15
AVERAGE			**1.78**	**45.8**			**15.2**	**14.2**	**20.9**	**37.0**	
J1A_30_18A	02/23/2007	1	1.80	45.0	0.029	175.1	30.0	24.2	16.8	37.6	0.15
J1A_30_18B	02/26/2007	1	1.79	44.7	0.035	172.1	30.0	20.1	14.6	37.0	0.15
J1A_30_18C	03/22/2007	3	1.78	47.3	0.036	196.4	30.0	20.8	9.5	38.1	0.15
J1A_30_18D	04/12/2007	3	1.78	45.1	0.034	175.7	30.0	16.5	16.1	38.2	0.15
AVERAGE			**1.79**	**45.5**			**30.0**	**20.4**	**14.3**	**37.7**	
J1A_60_18A	01/25/2007	1	1.80	46.1	0.033	370.6	60.1	35.8	13.1	38.5	0.15
J1A_60_18B	02/01/2007	1	1.79	46.1	0.034	367.4	59.8	34.5	15.0	39.0	0.15
J1A_60_18C	02/08/2007	1	1.80	47.0	0.029	386.4	59.9	34.9	16.6	39.2	0.15
J1A_60_18D	03/28/2007	3	1.78	46.7	0.044	345.1	60.2	*24.5*	12.8	37.9	0.15
J1A_60_18E	04/17/2007	3	1.78	43.0	0.034	316.9	59.9	38.7	11.8	36.8	0.15
AVERAGE			**1.79**	**46.5**			**60.0**	**36.0**	**13.9**	**38.3**	

*Experiment Name Coding: J1A_xx_yyZ

"J1A": Indicates test material, JSC-1A

xx: Indicates nominal test pressure in kPa

yy: Indicates nominal initial density in g/cm^3*10. "17"= 1.7 g/cc, "18" = 1.8 g/cc, "19" = 1.9 g/cc

Z: Used to distinguish between experiments of same material, pressure and density

Table 7. Summary of triaxial experiments performed on samples at 1.9 g/cc density. Friction angles reported in this table are derived from individual experiments, assuming zero cohesion.

Test Name*	Date Performed	Ton batch of sample	Density (ρ), g/cm^3	Maximum Friction Angle				E_{tan}, MPa	Dilatancy Angle (ψ), deg	Residual Friction Angle	
				Friction Angle (ϕ_{max}), c=0	Axial Strain, ε_{ax}	σ_1	σ_3			Friction Angle, (ϕ_{res})	Axial Strain, ε_{ax}
J1A_15_19B	01/10/2007	1	1.88	47.7	0.033	99.6	14.9	13.9	23.0	35.9	0.15
J1A_15_19C	01/11/2007	1	1.88	48.1	0.031	102.2	15.0	10.6	22.2	39.2	0.15
J1A_15_19D	03/09/2007	2	1.88	48.3	0.035	104.4	15.1	8.7	20.2	37.3	0.15
J1A_15_19E	04/03/2007	3	1.88	47.9	0.029	102.7	15.2	11.4	24.9	37.3	0.15
AVERAGE			**1.88**	**48**			**15.1**	**11.2**	**22.6**	**37.4**	
J1A_30_19A	02/28/2007	1	1.87	47.0	0.033	193.9	30.0	19.3	18.5	37.8	0.15
J1A_30_19B	03/01/2007	1	1.87	46.8	0.033	192.6	30.1	15.2	18.5	38.1	0.15
J1A_30_19C	03/20/2007	2	1.87	*50.8*	0.036	237.1	*30.1*	*21.4*	*16.1*	*39.8*	0.15
J1A_30_19D	04/04/2007	3	1.87	48.6	0.033	211.1	30.1	15.0	18.6	39.2	0.15
AVERAGE			**1.87**	**47.5**			**30.1**	**16.5**	**18.5**	**38.4**	
J1A_60_19A	01/17/2007	1	1.88	*49.3*	0.034	407.5	*55.9*	*20.5*	*8.6*	*44.9*	0.06
J1A_60_19B	01/18/2007	1	1.88	50.0	0.028	446.7	59.3	--	14.8	39.8	0.15
J1A_60_19C	01/19/2007	1	1.88	49.3	0.033	435.0	59.8	28.3	14.7	40.7	0.15
J1A_60_19D	01/22/2007	1	1.88	51.3	0.037	486.5	59.9	21.5	16.9	40.9	0.15
J1A_60_19E	01/24/2007	1	1.88	49.4	0.036	437.4	59.9	24.4	15.6	39.9	0.15
J1A_60_19F	03/12/2007	2	1.88	50.1	0.037	456.3	60.0	27.4	16.0	40.1	0.15
J1A_60_19G	04/05/2007	3	1.87	48.1	0.041	409.2	60.1	20.4	15.5	40.2	0.15
AVERAGE			**1.88**	**49.7**			**59.8**	**24.4**	**15.6**	**40.3**	

*Experiment Name Coding: J1A_xx_yyZ

"J1A": Indicates test material, JSC-1A

xx: Indicates nominal test pressure in kPa

yy: Indicates nominal initial density in g/cm^3*10. "17"= 1.7 g/cc, "18" = 1.8 g/cc, "19" = 1.9 g/cc

Z: Used to distinguish between experiments of same material, pressure and density

Table 8. Material properties of JSC-1a as determined by triaxial testing.

Density, g/cc	Pressure, kPa	Friction Angle (max)	Cohesion (c), kPa	Etan, MPa	Dilatancy Angle ( ), deg	Residual Friction Angle, (res), deg, c=0
1.70	15			11	16	34
1.71	30	42.9	1.4	16	10	36
1.71	60			15	8	37
1.78	15			14	21	37
1.79	30	44.5	1.8	20	14	38
1.79	60			36	14	38
1.88	15			11	23	37
1.87	30	48.8	2.4	17	19	38
1.88	60			24	16	40

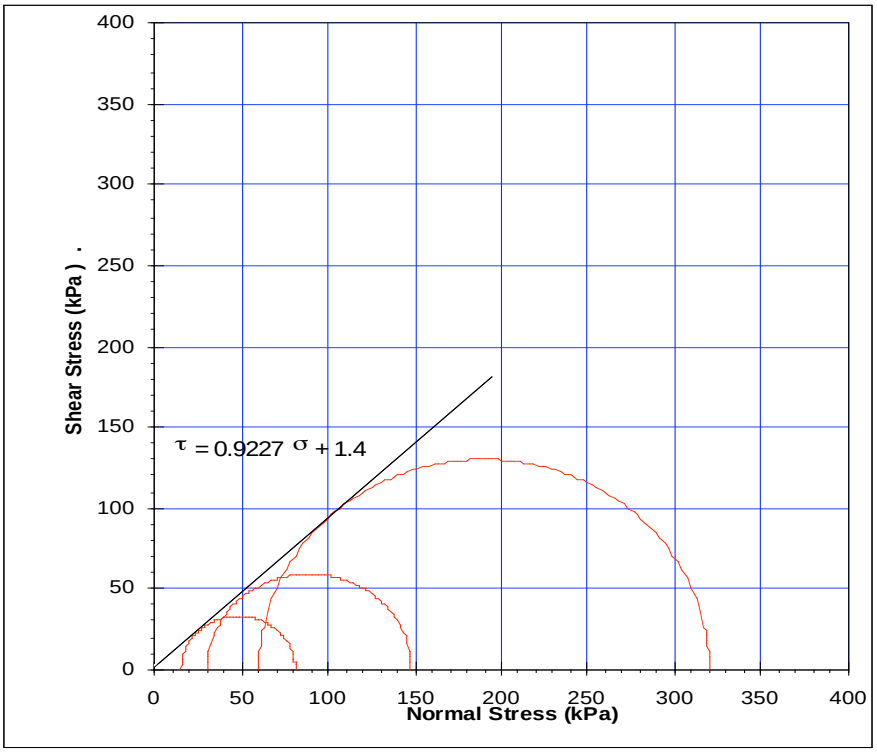

Figure 9. Mohr-Coulomb model of JSC-1a soil strength parameters at 1.7 g/cm^3 density.

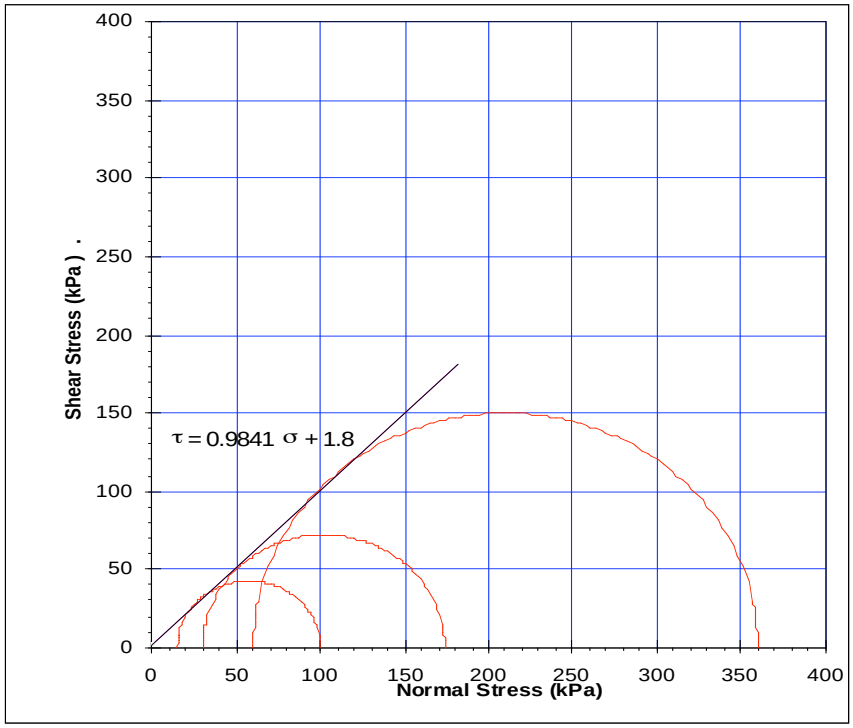

Figure 10. Mohr-Coulomb model of JSC-1a soil strength parameters at 1.8 g/cm^3 density.

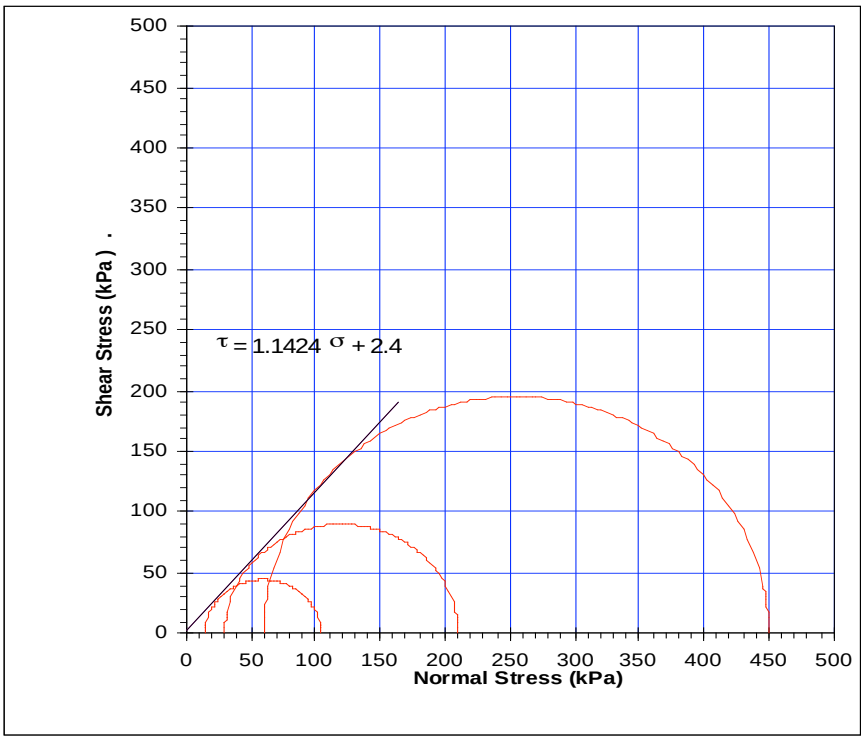

Figure 11. Mohr-Coulomb model of JSC-1a soil strength parameters at 1.9 g/cm^3 density.

2.3 Direct Tension

Nine experiments were performed in the direct tension device. In order to have a sufficient quantity of material for the apparatus, Ton 1, 2, and 3 samples were mixed to provide a single sample. Three different bulk densities (1.7, 1.8, 1.9 g/cm^3) have been tested for the JSC-1A. The results of the direct tension tests on three different densities are given in Table 9.

Table 9. Tensile strength properties of JSC-1A Tons 1, 2, 3 mixed sample, 1.7 g/cm^3

Area	Water Weight(g)	Load for Friction (g)	Total Load	**Tensile Strength (kPa)**
278.89	385	125	260	**0.93**
278.89	388	125	263	**0.94**
278.89	389	125	264	**0.95**

Table 10. Tensile strength properties of JSC-1A Tons 1, 2, 3 mixed sample, 1.8 g/cm^3

Area	Water Weight(g)	Load for Friction (g)	Total Load	**Tensile Strength (kPa)**
278.89	499	125	374	**1.34**
278.89	497	125	372	**1.33**
278.89	498	125	373	**1.34**

Table 11. Tensile strength properties of JSC-1A Tons 1, 2, 3 mixed sample, 1.9 g/cm^3

Area	Water Weight(g)	Load for Friction (g)	Total Load	**Tensile Strength (kPa)**
278.89	689	125	564	**2.02**
278.89	682	125	557	**2.00**
278.89	683	125	558	**2.00**

The direct tension experiment results show that cohesion and tensile strength of the JSC-1A are in the same magnitude. Even though the parameters are two different properties of granular materials, the values are quite close.

3 Summary and Conclusions

Several experiments have been performed on JSC-1A, and behavioral parameters were determined for three density levels. These data indicate that JSC-1A is a high friction, high stiffness soil with extraordinary dilatancy. Unconventional direct tension experiments showed that the tensile strength of the lunar regolith simulant JSC-1A s significant. It must be noted that the response of JSC-1A to loading is dependent on density of the specimen and confinement

pressure. Table 10 summarizes several geotechnical parameters of JSC-1 and JSC-1a lunar regolith simulants. The particle size distribution and shear strength of the two materials is similar. The values of Young's Modulus and dilatancy do differ, most likely due to some variations in measurement techniques.

Table 10. Comparison of JSC-1 and JSC-1a lunar regolith simulants.

	JSC-1				JSC-1a		
Passing #200	Perkins and Madson, 1996	36%			39%		
Cu	Perkins and Madson, 1996	7.5			6.85		
Cc	Perkins and Madson, 1996	1.12			1.06		
D_{50}	Perkins and Madson, 1996	≈0.11 mm			0.10 mm		
Specific Gravity	Willman et al., 1995	2.91					
Void Ratio max	Perkins and Madson, 1996	e_{max} = 1.18 e_{min} = 0.61	ρ_{min} = 1.33 g/cc ρ_{max} = 1.80 g/cc				
	Klosky, 2000		ρ_{min} = 1.43 g/cc ρ_{max} = 1.83 g/cc				
Shear Strength	Perkins and Madson, 1996	ϕ = 64° for c=0 at p=10kPa					
		ρ, g/cc	ϕ, deg	c, kPa	ρ, g/cc	ϕ, deg	c, kPa
	McKay, 1994	1.50, 1.60, 1.65	45.0	≤ 1.0	1.7	43.9	1.4
	Perkins, 1991	1.9	49	0.2	1.8	44.5	1.8
	Carrier, 1991		52-55	2.4-3.8	1.9	48.8	2.4
	Klosky, 1996	1.62	44.4	3.9			
	Klosky 1996	1.72	52.7	13.4			
Dilatancy		ρ, g/cc	Conf. Stress, kPa	Dil. Angle, deg	ρ, g/cc	Conf. Stress, kPa	Dil. Angle, deg
	Klosky 1996	1.62	1 10	44.0° 40.5°	1.7	15 30 60	16 10 8
	Klosky 1996	1.72	10	65.0°	1.8	15 30 60	21 14 14
					1.9	15 30 60	23 19 16
Residual Friction Angle	Perkins and Madson, 1996	42°			37°		
E, MPa Young's modulus	Klosky, 2000	ρ, g/cc	E, MPa		ρ, g/cc	Conf. Stress, kPa	E, MPa
		1.57 1.64	18-60 65-110		1.7	15 30 60	11 16 15
					1.8	15 30 60	14 20 36
					1.9	15 30 60	11 17 24

4 References

Al-Shibli, K. (1995), "Localized Deformations in Granular Materials", Ph.D. Thesis, University of Colorado, Boulder.

ASTM (1995a-1995b), Annual Book of ASTM Standards, Soil and Rock, American Society for Testing and Materials, ASTM, Philedelphia, PA.

Bishop, A.W. and Henkel, D.J. (1962), The Measurement of Soil Properties in the Triaxial Test, Edward Arnold, London.

Carrier, W.D., Mitchell, J.K., and Mahmood, A. (1973), "The Nature of Lunar Soil", *J. Soil Mech. and Found.*, ASCE, Vol. 99, 813-832.

Carrier, W. D., Olhoeft, G. R., and Mendell, W. (1991), ''Physical Properties of the Lunar Surface.'' *Lunar Sourcebook*, Heiken, Vaniman, and French, eds., Cambridge University Press, New York, 475–567.

Eden, W.J., (1963), Soil Testing, CBD-43. Canadian Building Digests, NRC's Institute for Research in Construction Press, Canada**.**

Hayashi, H., Honda, H., and Yamada, T. (1992), "Modeling of nonlinear stress strain relations of sands for dynamic response analysis". *Proc. of World Conf. on Earthquake Engnrg.*, Vol. 11, 6819-6825, Madrid, Spain, Balkema, Rotterdam.

Klosky, J.L., Sture, S., Ko, H.-Y., Barnes, F. (1996), "Mechanical Properties of JSC-1 Lunar Regolith Simulant", *Proceedings of Space V: Engineering, Construction and Operations in Space '96*, Vol. 1, 680-688 ASCE.

Klosky, J.L.(1997), "Behavior of Composite Granular Materials and Vibratory Helical Anchors", Ph.D. Thesis, University of Colorado-Boulder.

Klosky, J.L., Sture, S., Ko, H.-Y., Barnes, F. (2000), "Geotechnical Behavior of JSC-1 Lunar Regolith Simulant", *J. of Areospace Engineering*, ASCE 13:4, 680-688.

McKay, D.S., J.L. Carter, W.W. Boles, C.C. Allen, J.H. Allton (1994), "JSC-1: A New Lunar Soil Simulant", *Proceedings of Space IV: Engineering, Construction and Operations in Space*, Vol. 2, pp 857-866.

Perkins, S.W. (1991), "Modeling of Regolith Structure Interaction in Extraterrestrial Constructed Facilities", Ph.D. Thesis, University of Colorado, Boulder.

Perkins, S.W., Madson, C.R. (1996), "Mechanical and Load-Settlement Characteristics of Two Lunar Soil Simulant", *J. of Aerospace Engineering*, ASCE 9:1, 1-9.

Scott R. F. (1968), "The Density of Lunar Surface Soil," *J. Geophys. Res*., Vol. 73, 5469–5471.

Scott R.F. (1969), "Mechanical Properties of Lunar Surface Materials", *Powder Tech.*, Vol. 3, 41-50.

Subhash, G., Nemat-Nasser, S., Mehrabadi, M.M., Shodja, H.M. (1991), "Experimental Investigation of Fabric-Stress Relations in Granular Materials". *Mech. Mat.*, Vol. 11, 87- 106.

Tatsuoka, F.(2000), “Impacts on Geotechnical Engineering of Several Recent Findings from Laboratory Stress-Strain Tests on Geomaterials”, Burmister Lecture, 31st, October 2000, the Columbia University, N.Y., U.S.A

Willman, B.M., Boles, W.B., McKay, D.S., and Allen, C.C. (1995), ‘‘Properties of Lunar Soil Simulant JSC-1.’’ *J. Aerosp. Eng*., ASCE, 8:2, 77–87.

Appendix A

Triaxial tests results of JSC-1A

15 kPa confinement

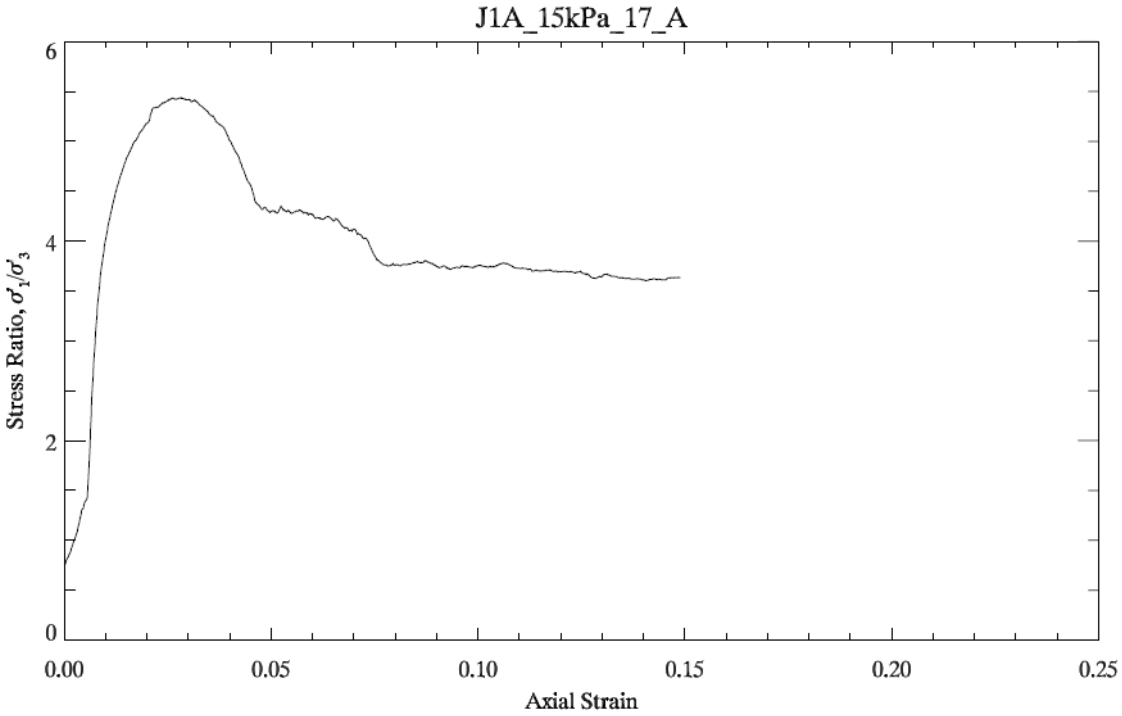

Figure A-1. Behavior of stress ratio as a function of axial strain for density of 1.7 g/cm^3 at 15 kPa confining stress.

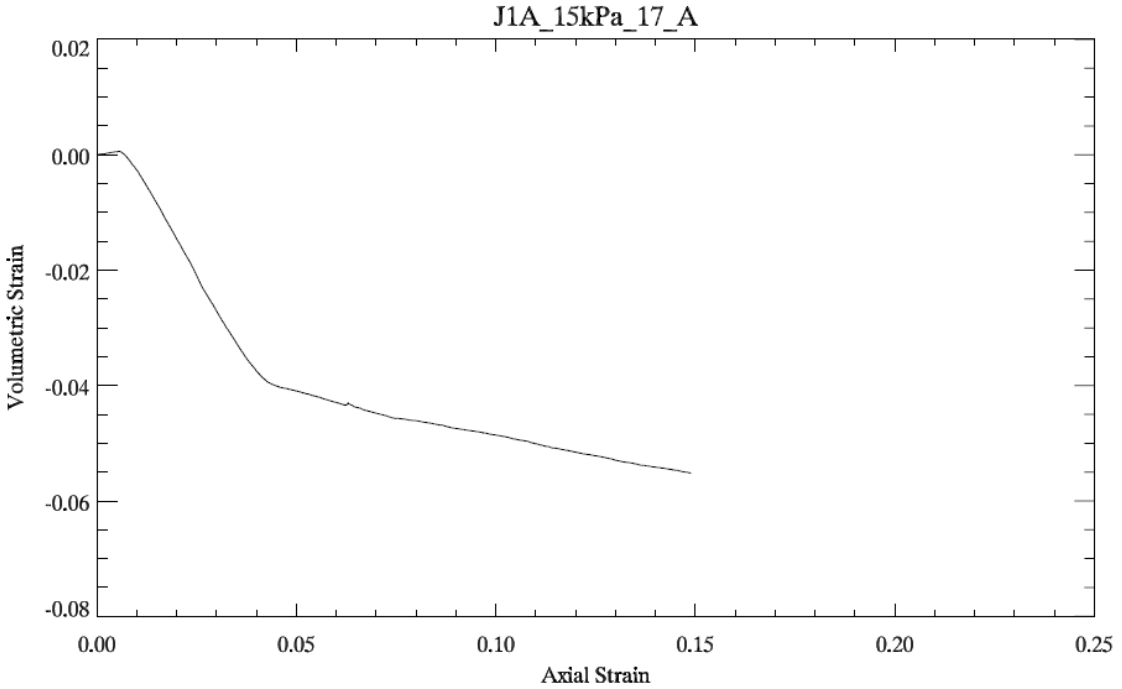

Figure A-2. Volumetric behavior for density of 1.7g/cm^3 at 15 kPa confining stress

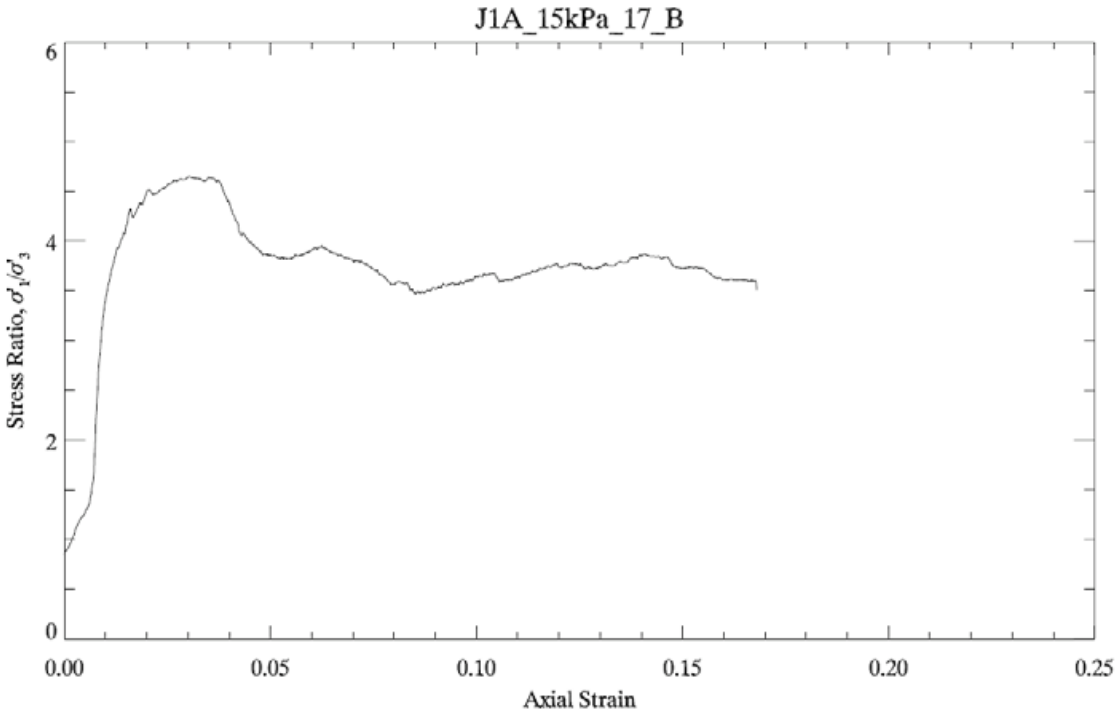

Figure A-3. Behavior of stress ratio as a function of axial strain for density of 1.7 g/cm^3 at 15 kPa confining stress.

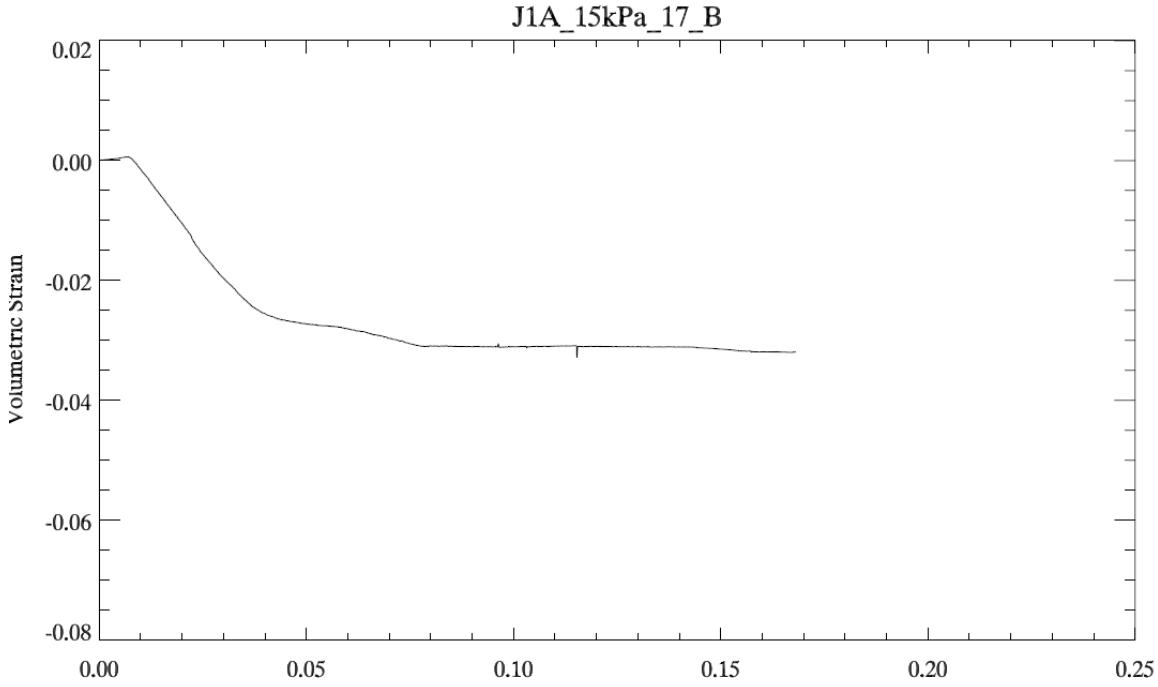

Figure A-4. Volumetric behavior for density of 1.7g/cm^3 at 15 kPa confining stress

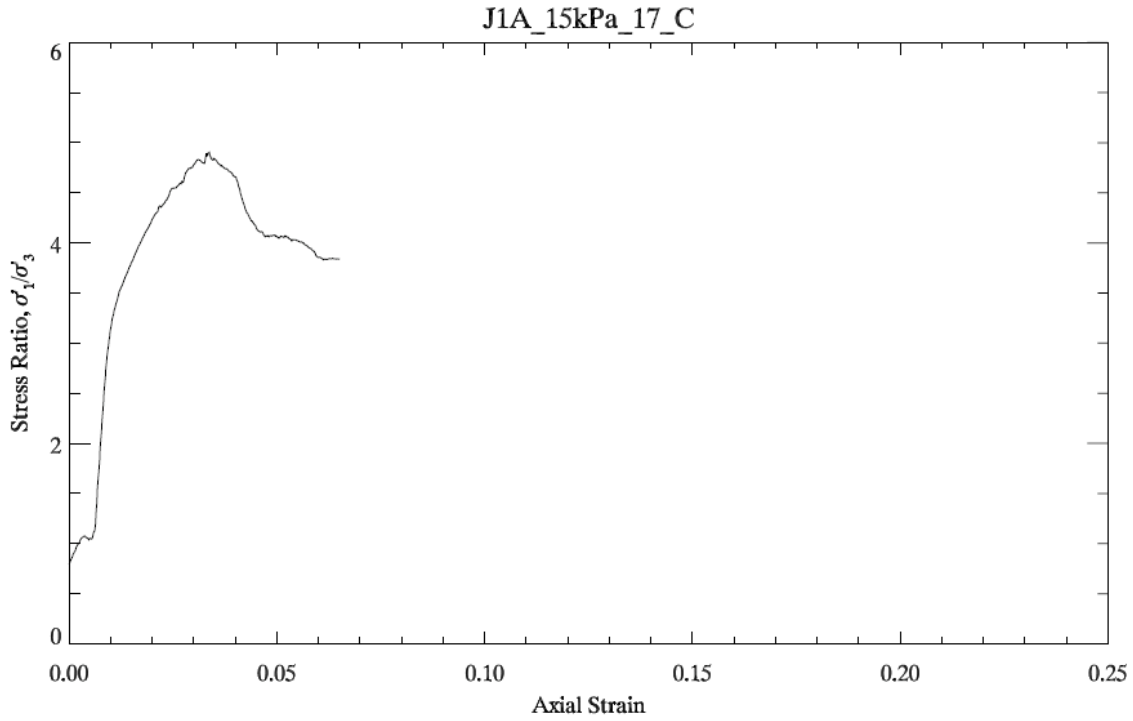

Figure A-5. Behavior of stress ratio as a function of axial strain for density of 1.7 g/cm^3 at 15 kPa confining stress.

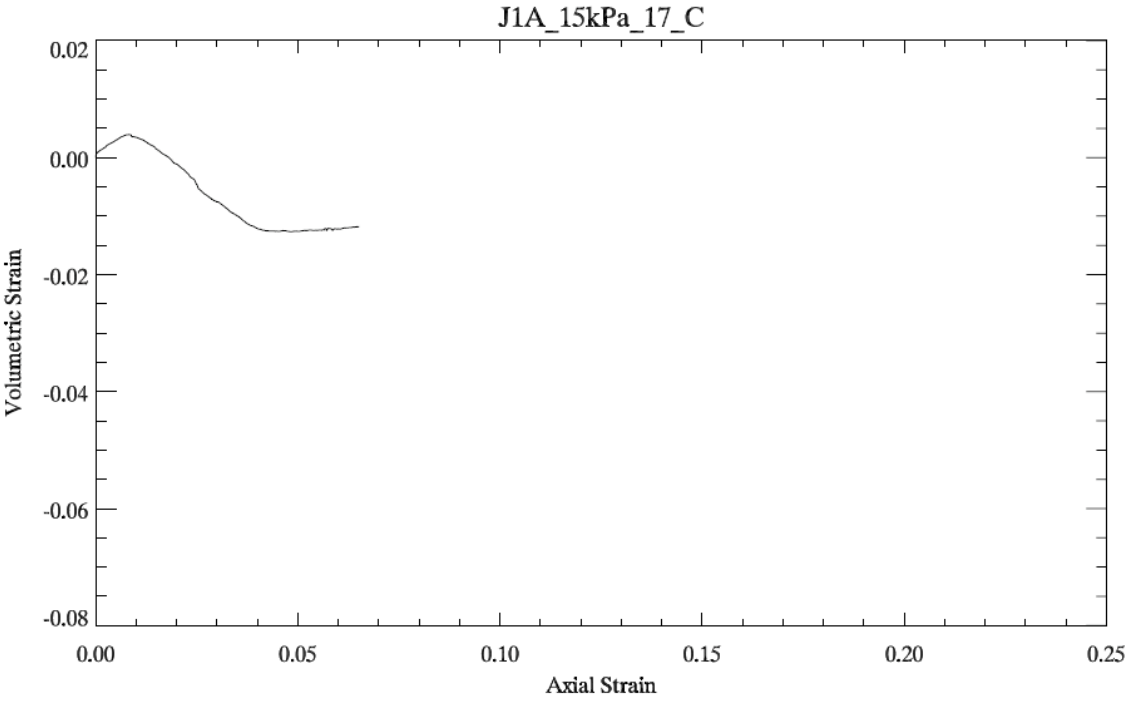

Figure A-6. Volumetric behavior for density of 1.7g/cm^3 at 15 kPa confining stress

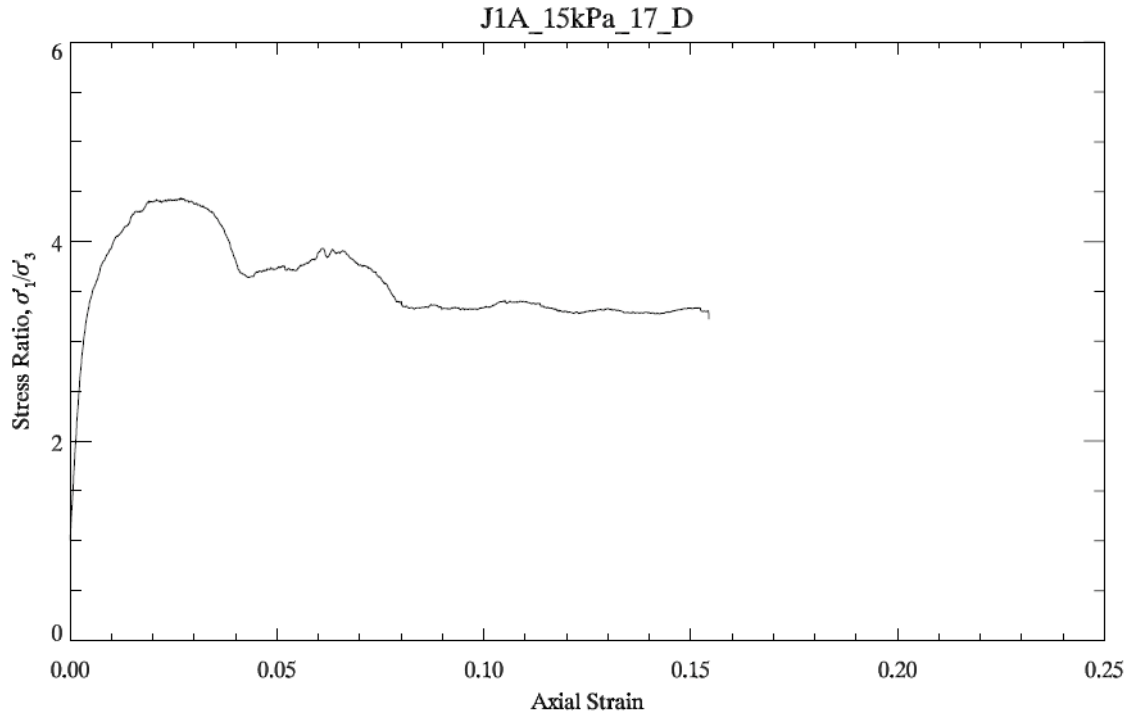

Figure A-7. Behavior of stress ratio as a function of axial strain for density of 1.7 g/cm^3 at 15 kPa confining stress.

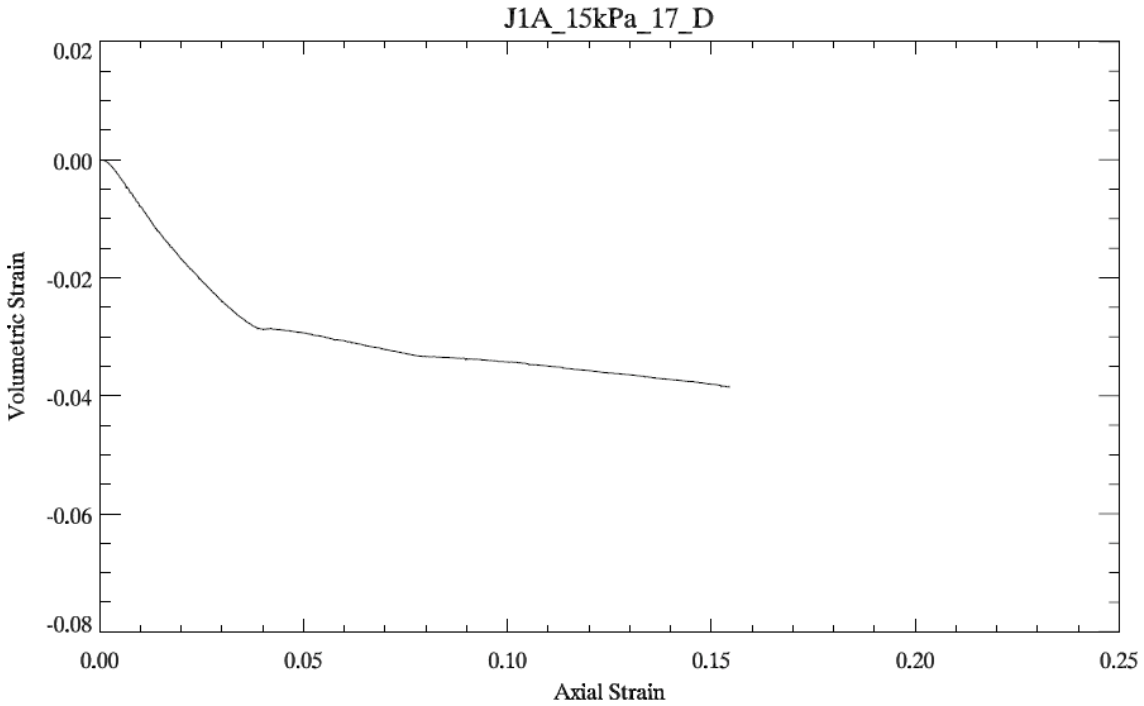

Figure A-8. Volumetric behavior for density of 1.7g/cm^3 at 15 kPa confining stress

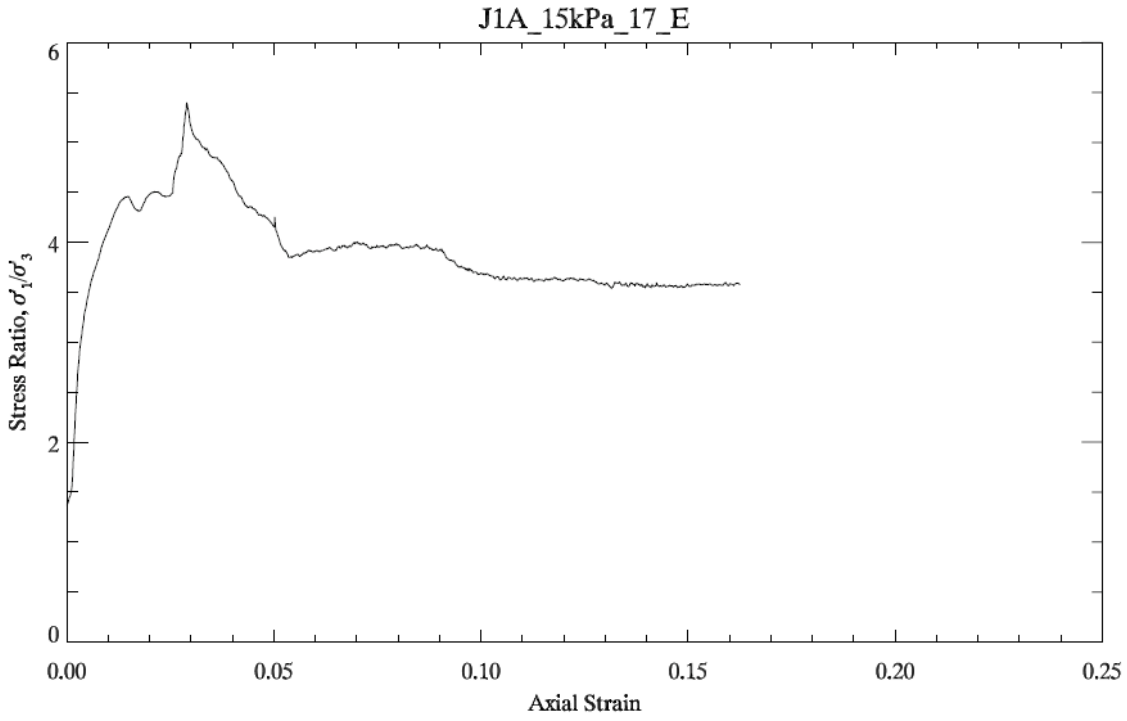

Figure A-9. Behavior of stress ratio as a function of axial strain for density of 1.7 g/cm^3 at 15 kPa confining stress.

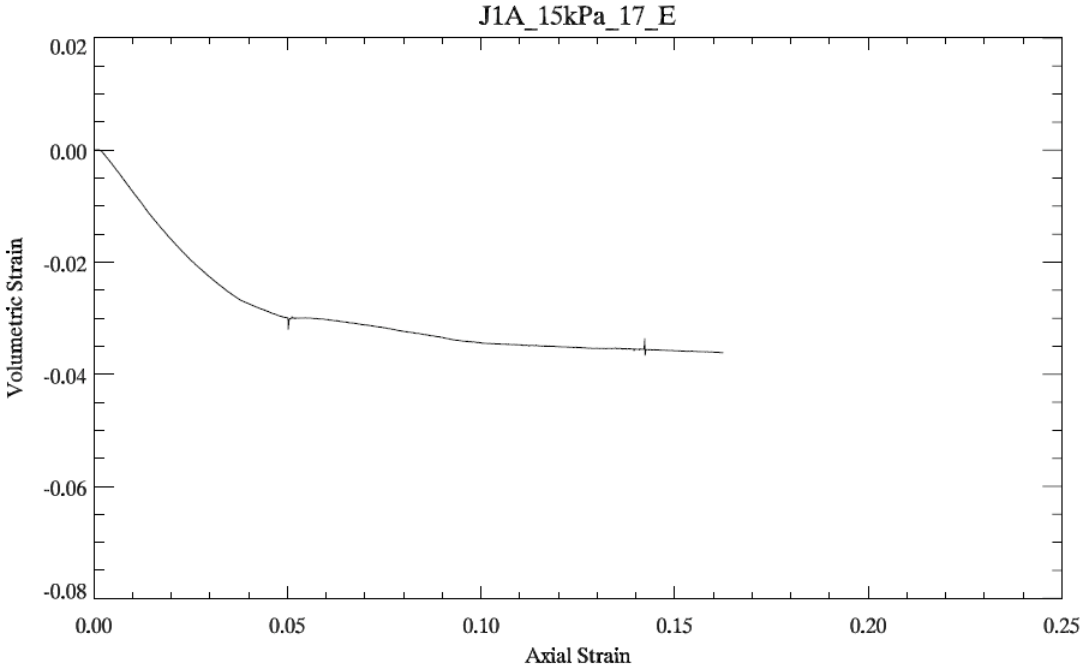

Figure A-10. Volumetric behavior for density of 1.7g/cm^3 at 15 kPa confining stress

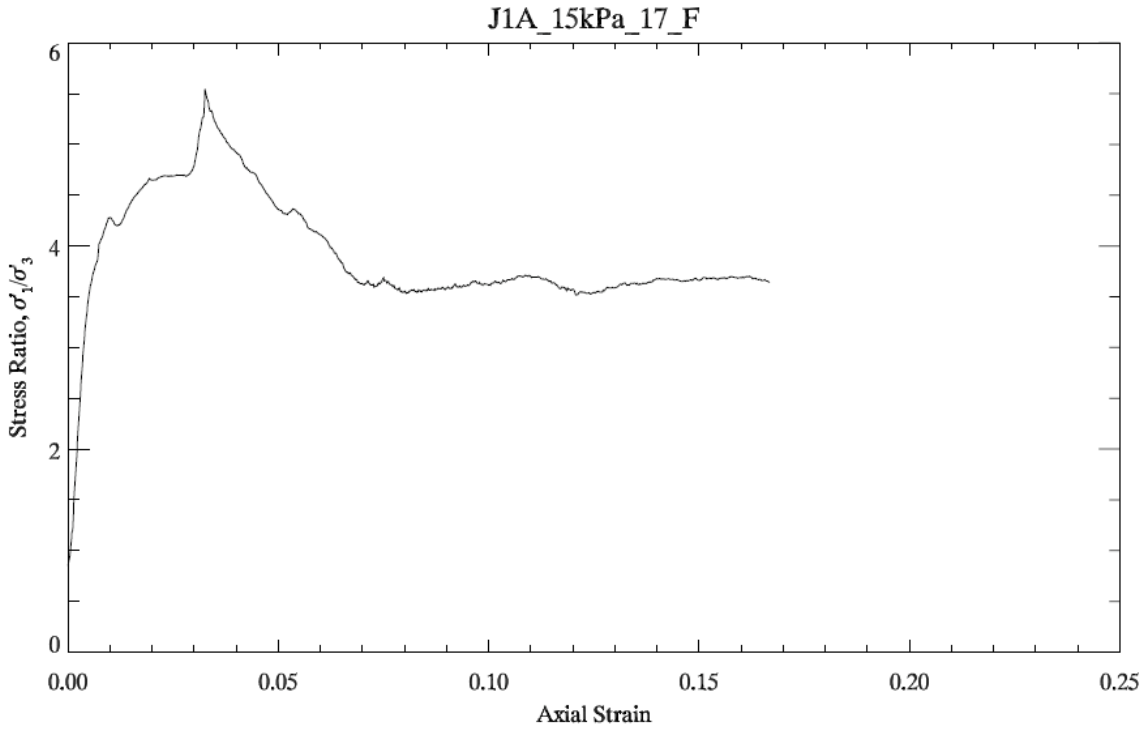

Figure A-11. Behavior of stress ratio as a function of axial strain for density of 1.7 g/cm^3 at 15 kPa confining stress.

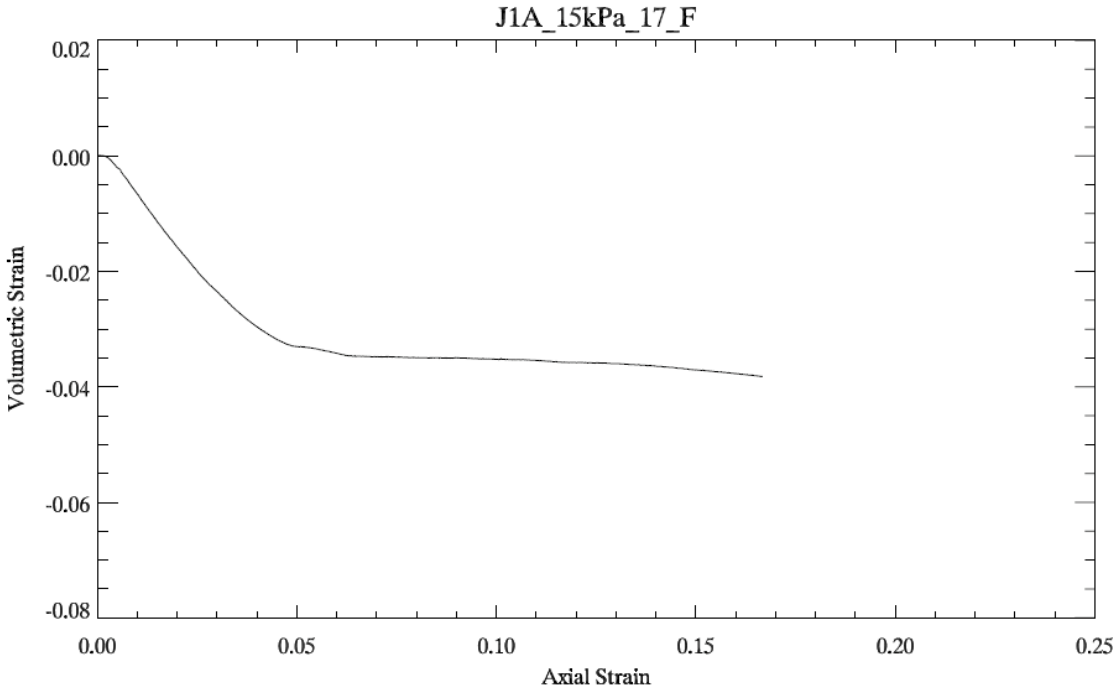

Figure A-12. Volumetric behavior for density of 1.7g/cm^3 at 15 kPa confining stress

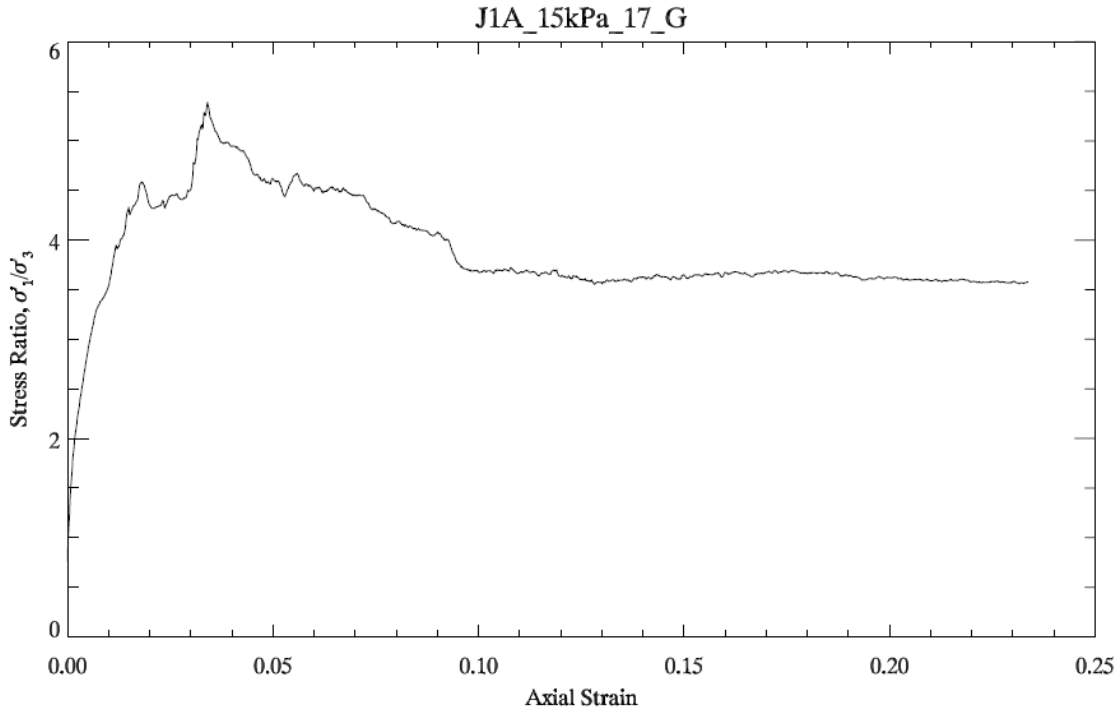

Figure A-13. Behavior of stress ratio as a function of axial strain for density of 1.7 g/cm^3 at 15 kPa confining stress.

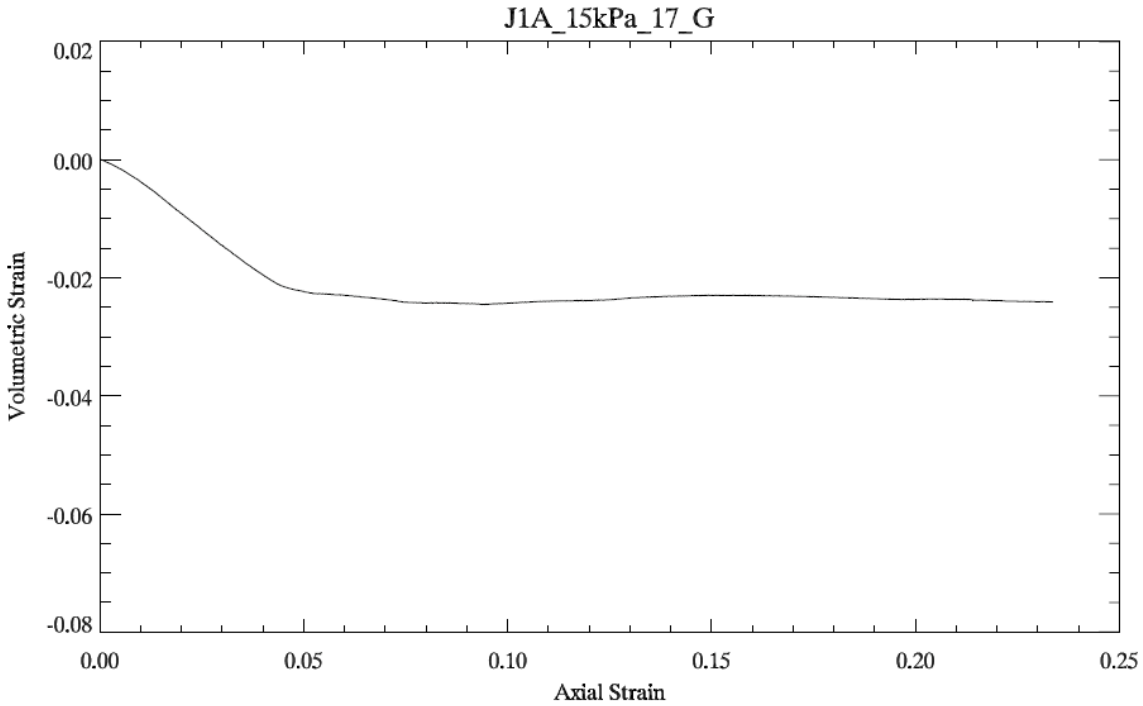

Figure A-14. Volumetric behavior for density of 1.7g/cm^3 at 15 kPa confining stress

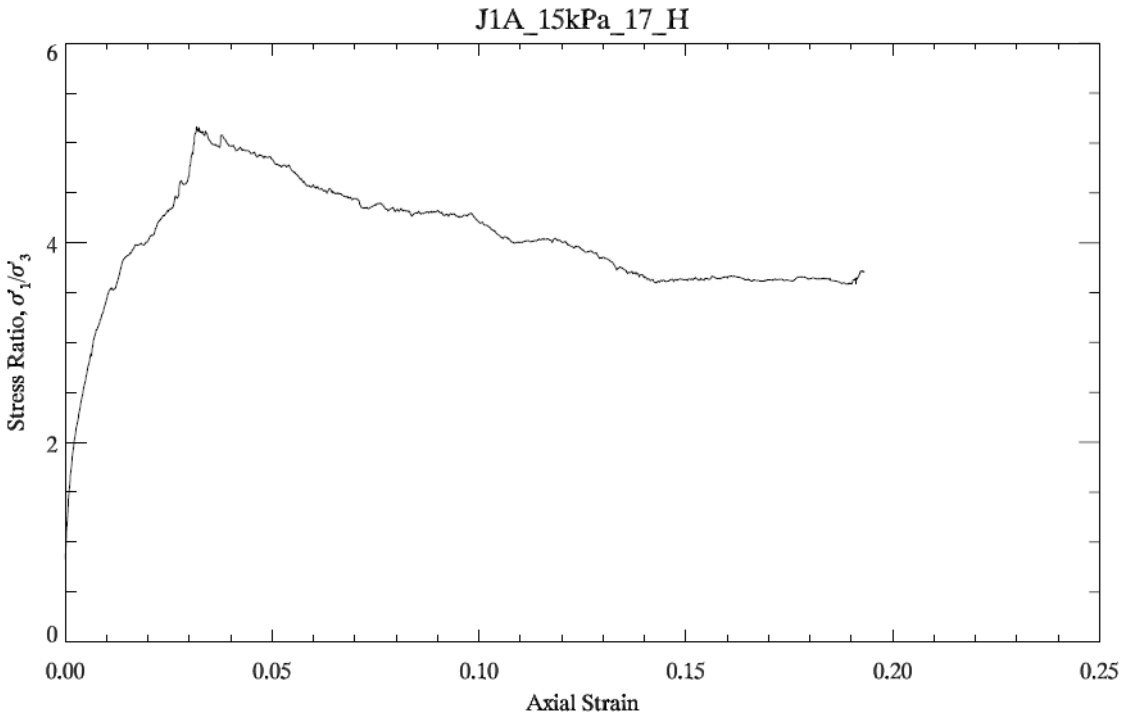

Figure A-15. Behavior of stress ratio as a function of axial strain for density of 1.7 g/cm^3 at 15 kPa confining stress.

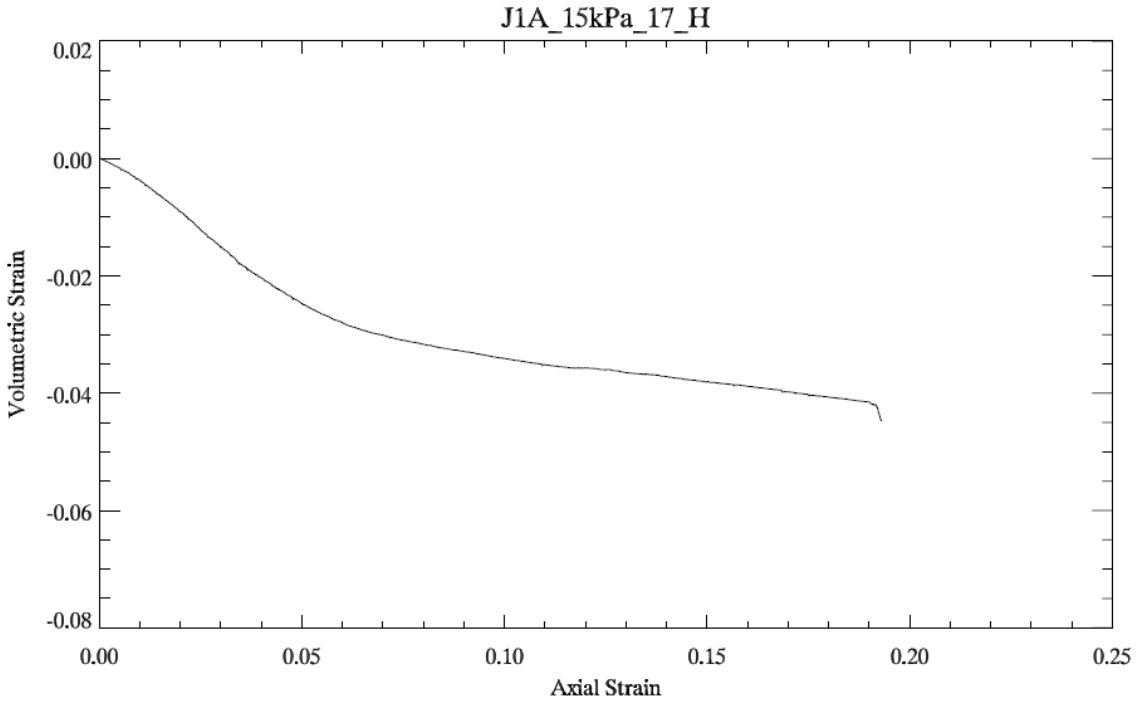

Figure A-16. Volumetric behavior for density of 1.7g/cm^3 at 15 kPa confining stress

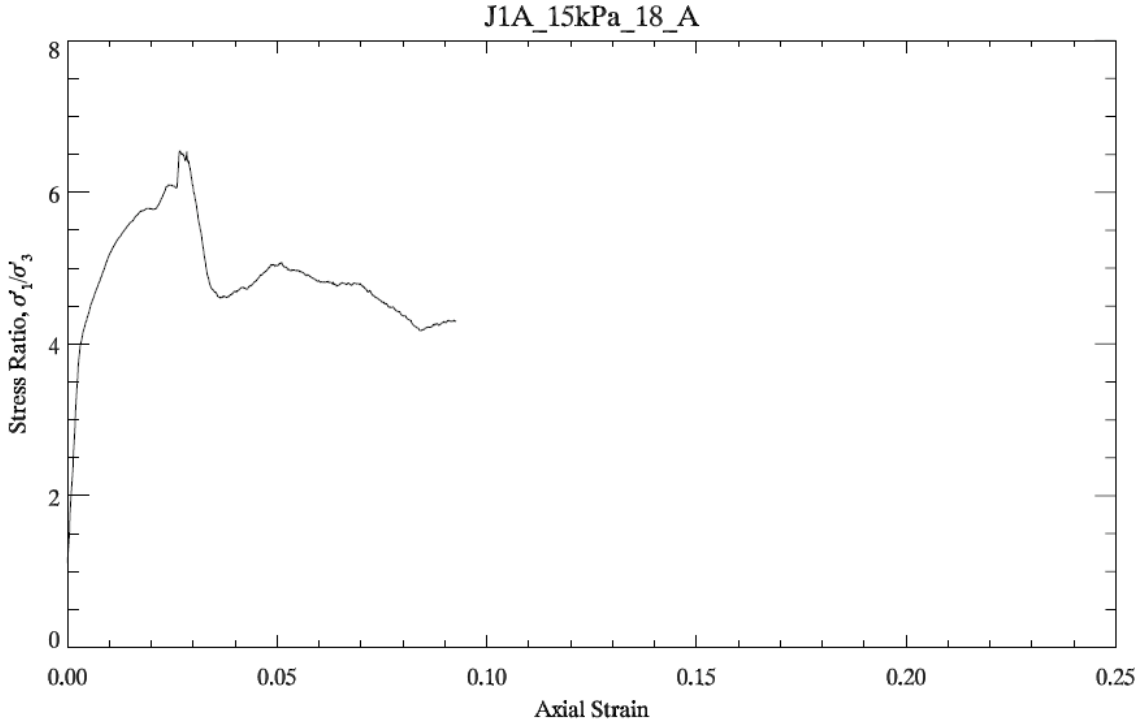

Figure A-17. Behavior of stress ratio as a function of axial strain for density of 1.8 g/cm^3 at 15 kPa confining stress.

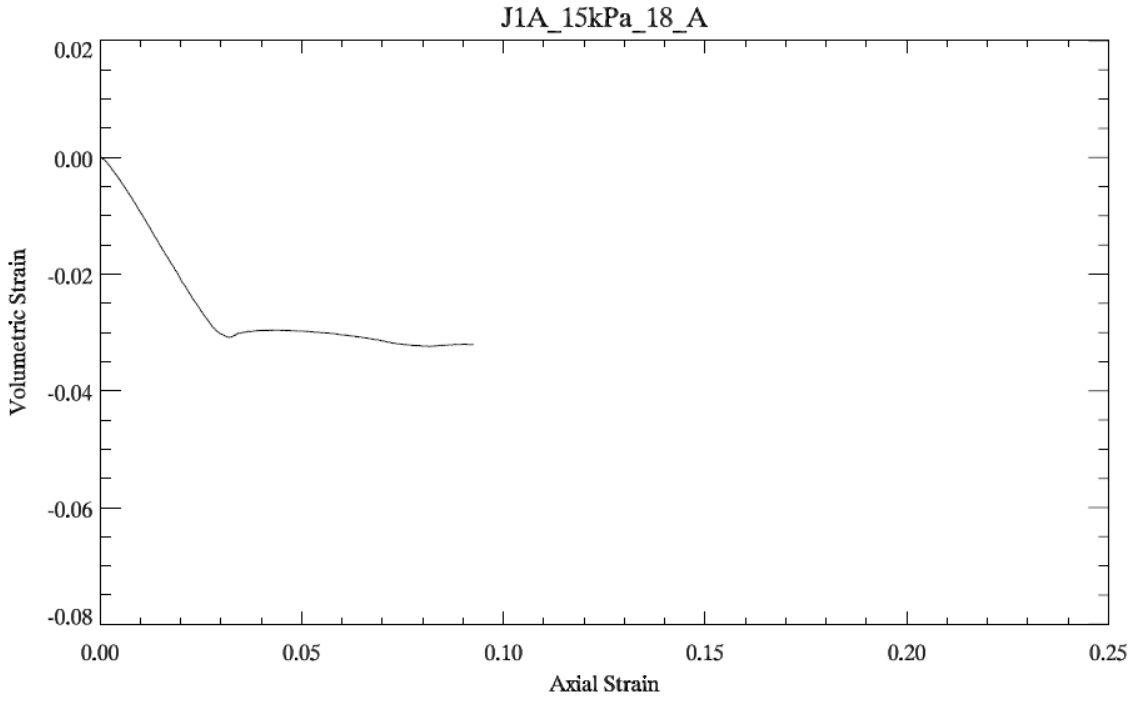

Figure A-18. Volumetric behavior for density of 1.8 g/cm^3 at 15 kPa confining stress

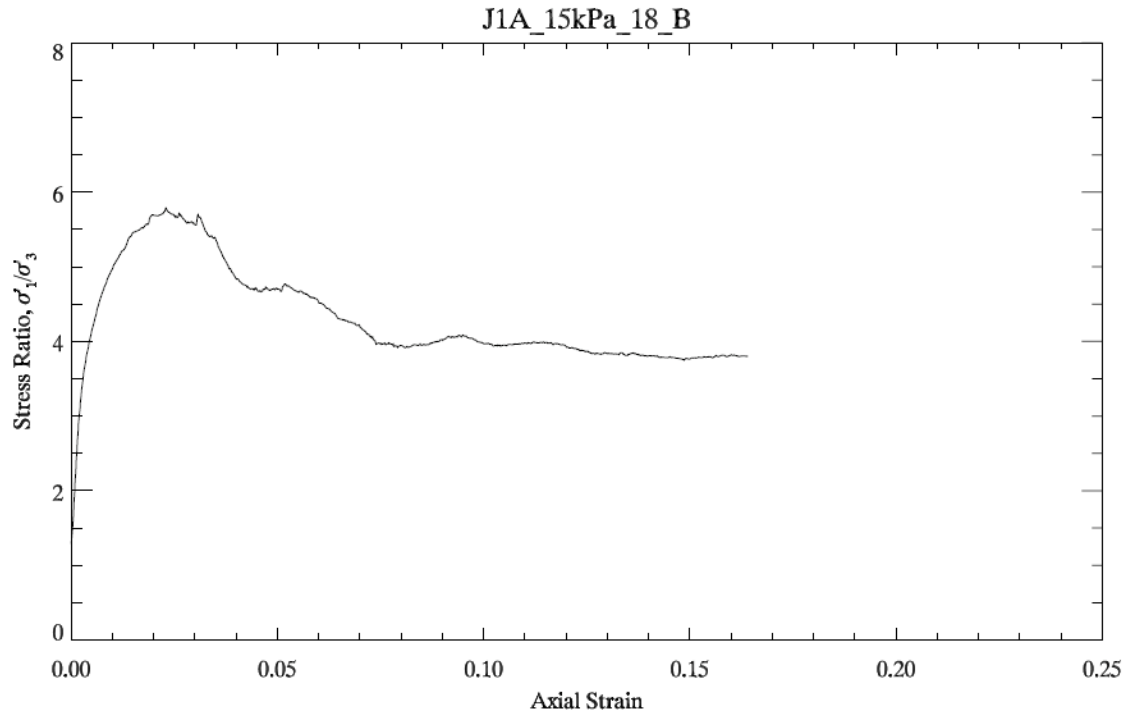

Figure A-19. Behavior of stress ratio as a function of axial strain for density of 1.8 g/cm^3 at 15 kPa confining stress.

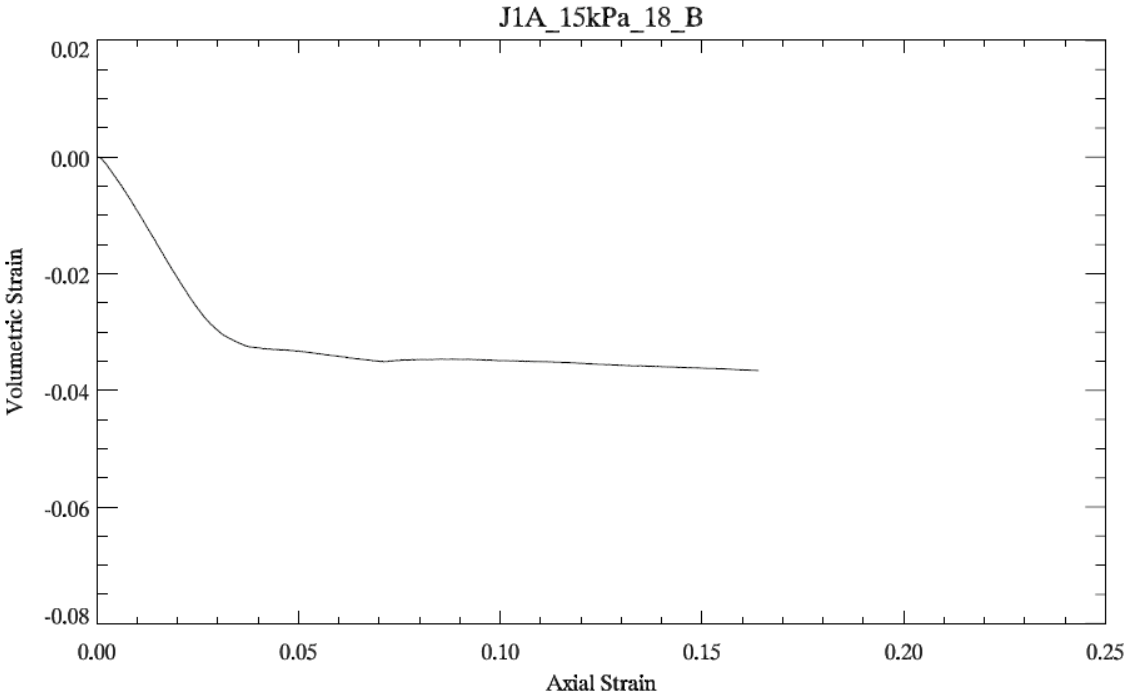

Figure A-20. Volumetric behavior for density of 1.8 g/cm^3 at 15 kPa confining stress

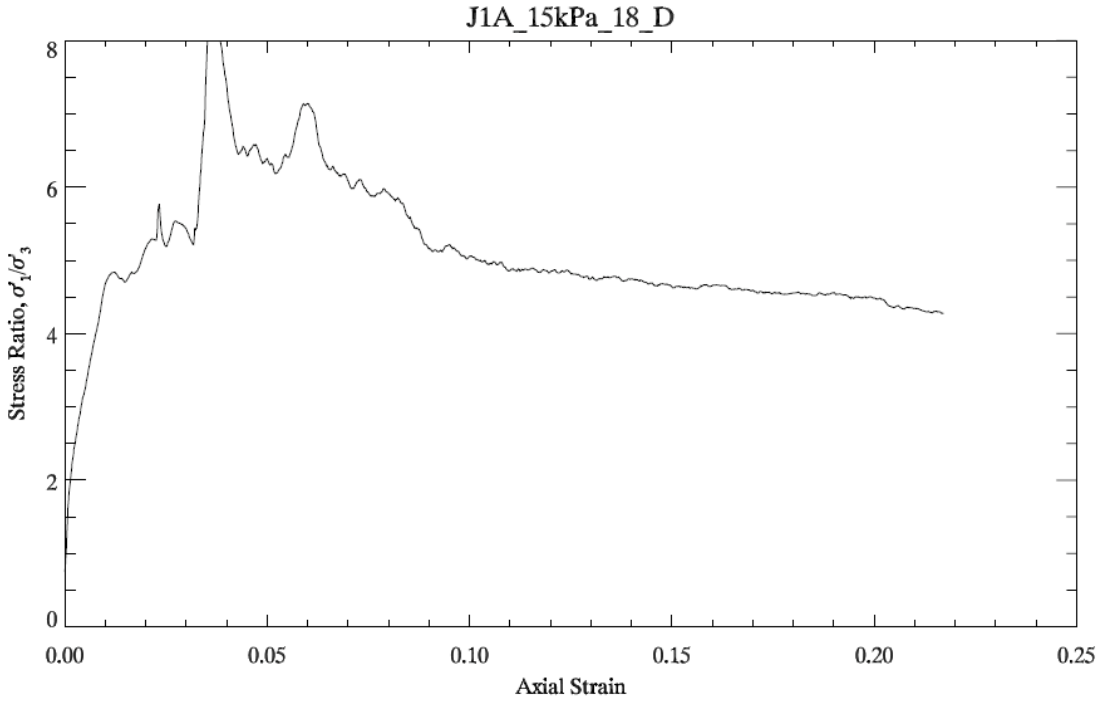

Figure A-21. Behavior of stress ratio as a function of axial strain for density of 1.8 g/cm^3 at 15 kPa confining stress.

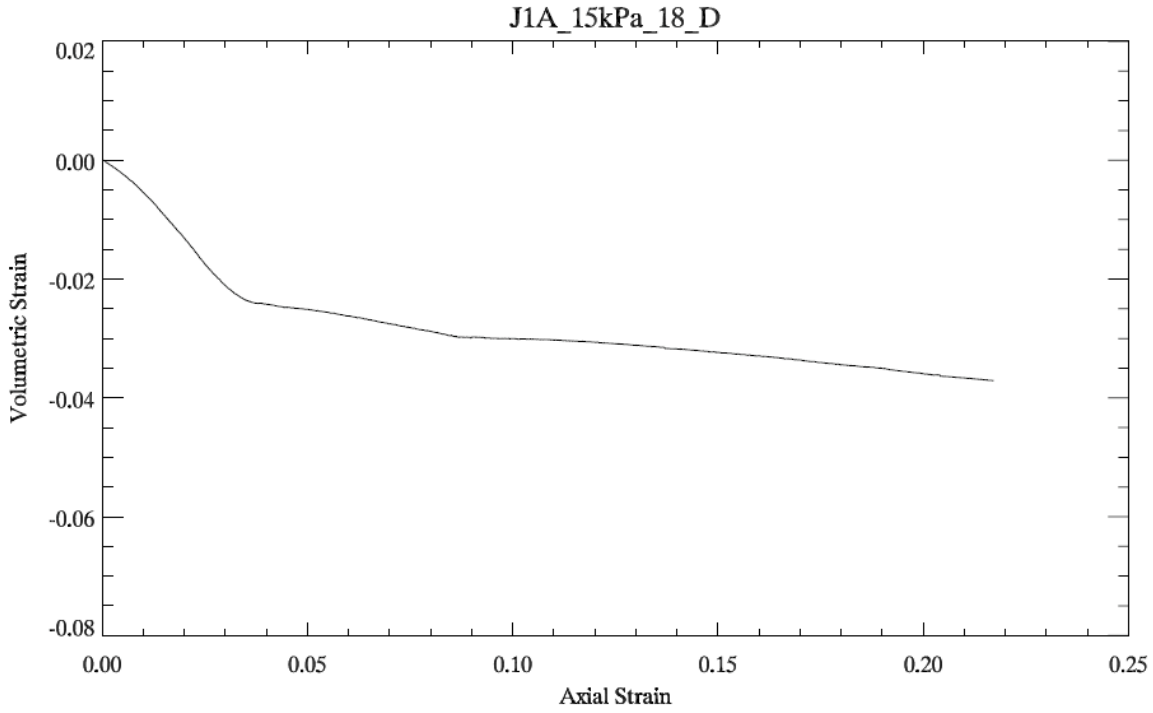

Figure A-22. Volumetric behavior for density of 1.8 g/cm^3 at 15 kPa confining stress

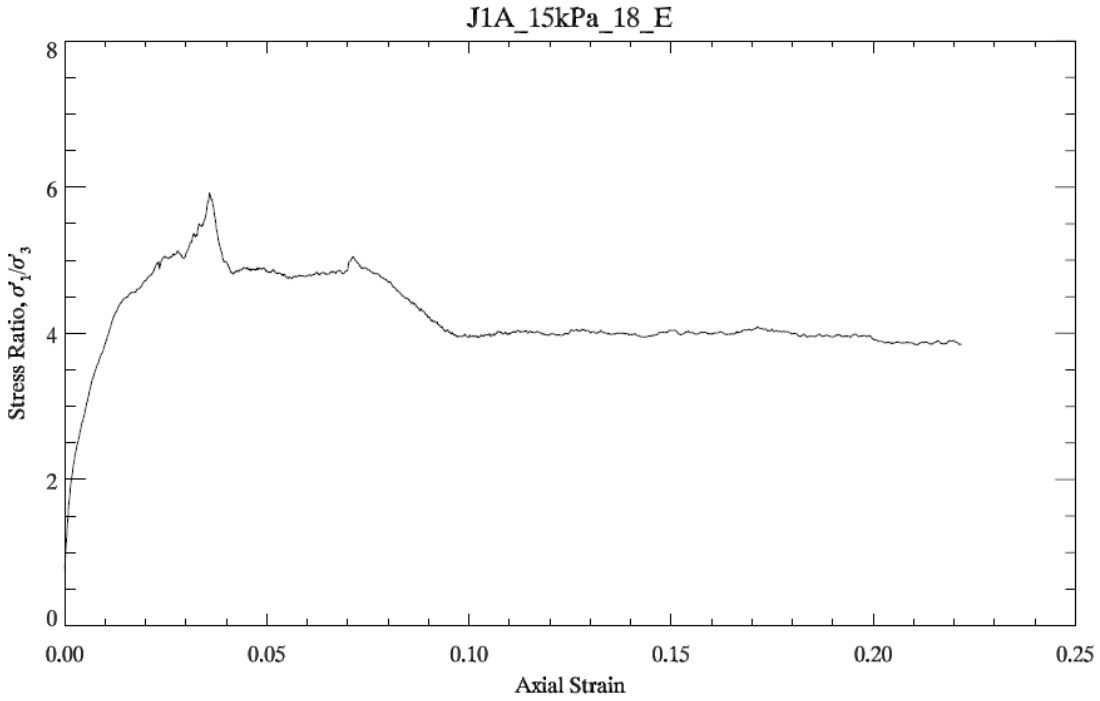

Figure A-23. Behavior of stress ratio as a function of axial strain for density of 1.8 g/cm^3 at 15 kPa confining stress.

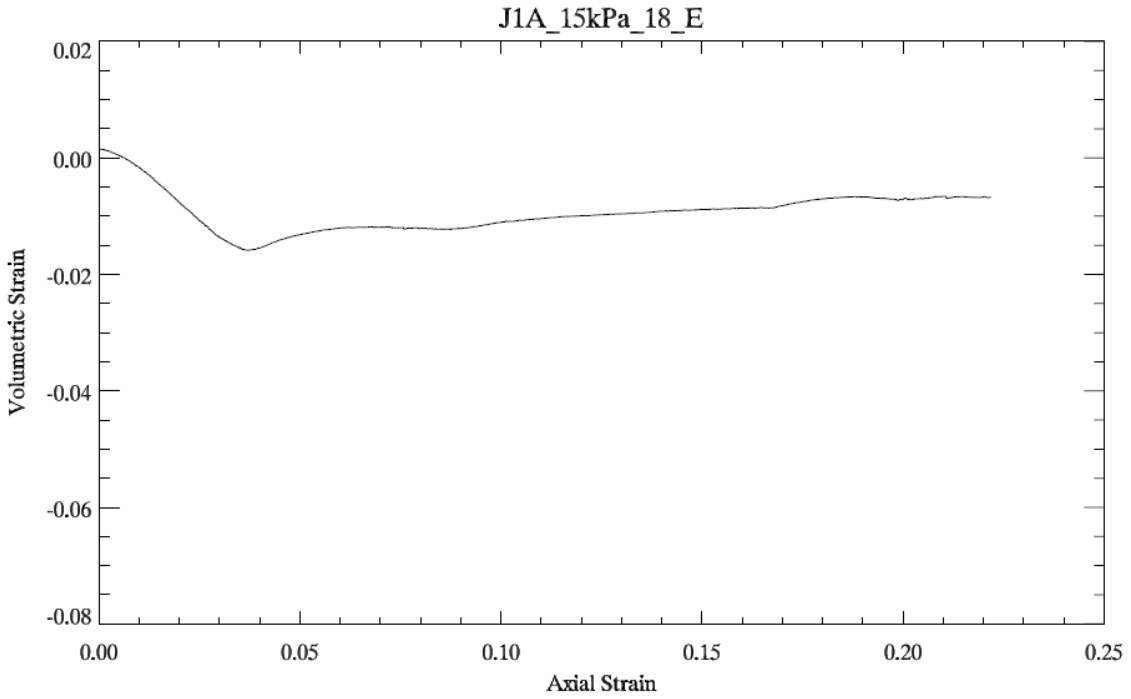

Figure A-24. Volumetric behavior for density of 1.8 g/cm^3 at 15 kPa confining stress

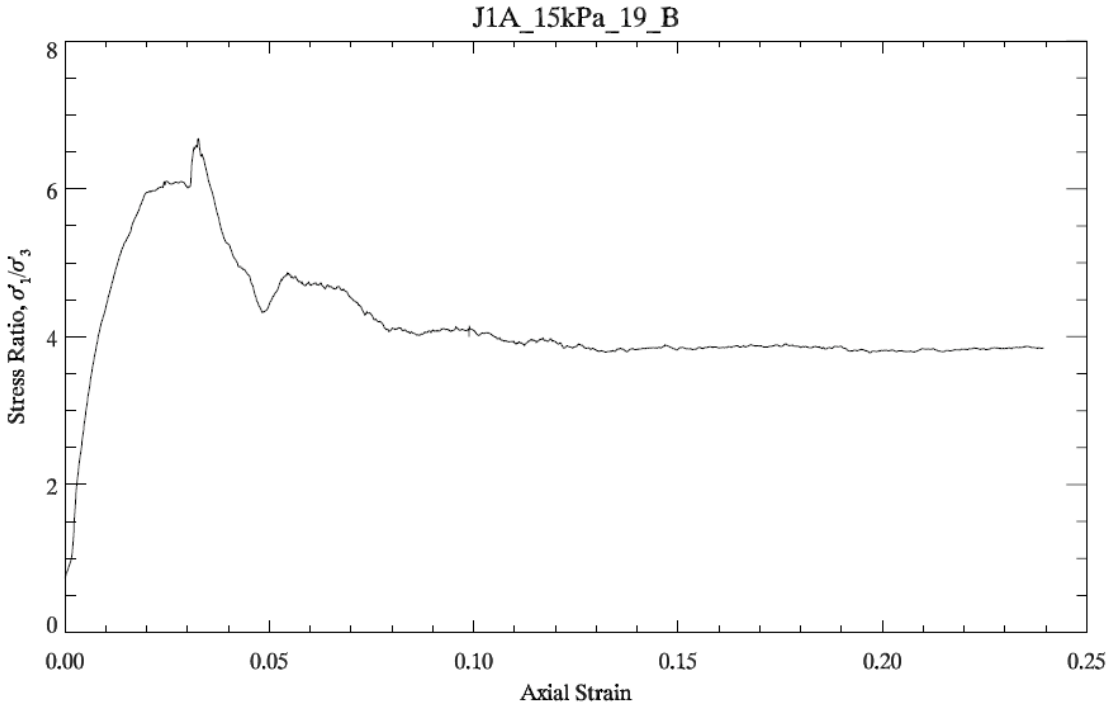

Figure A-25. Behavior of stress ratio as a function of axial strain for density of 1.9 g/cm^3 at 15 kPa confining stress.

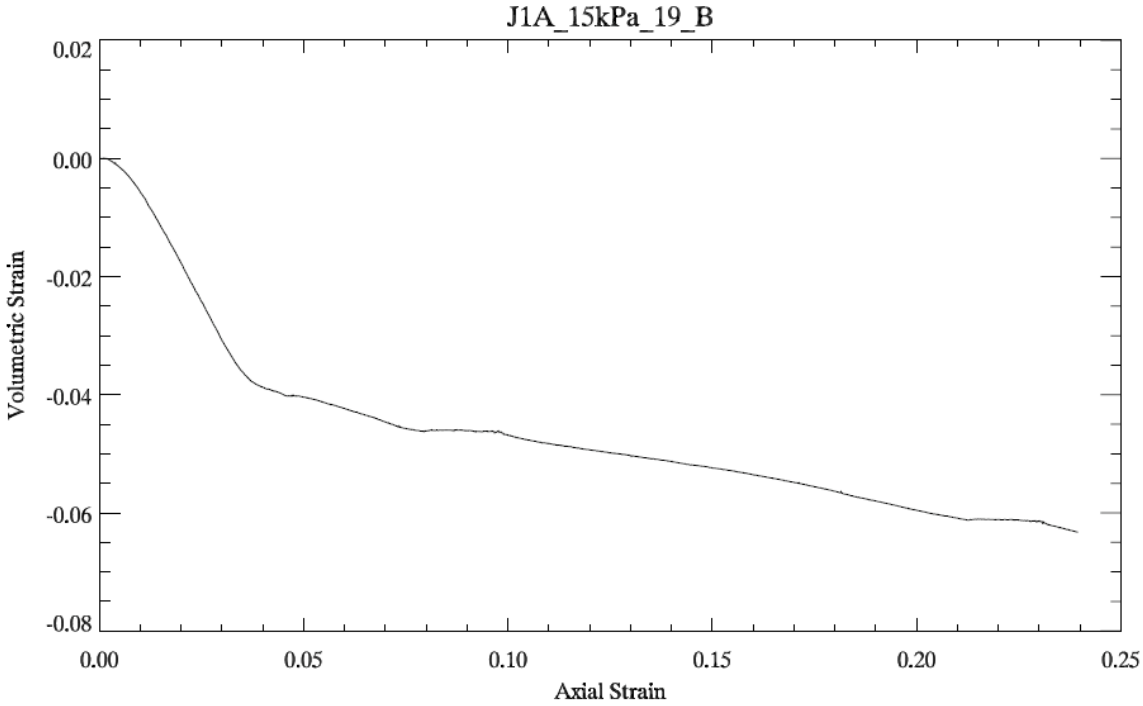

Figure A-26. Volumetric behavior for density of 1.9 g/cm^3 at 15 kPa confining stress

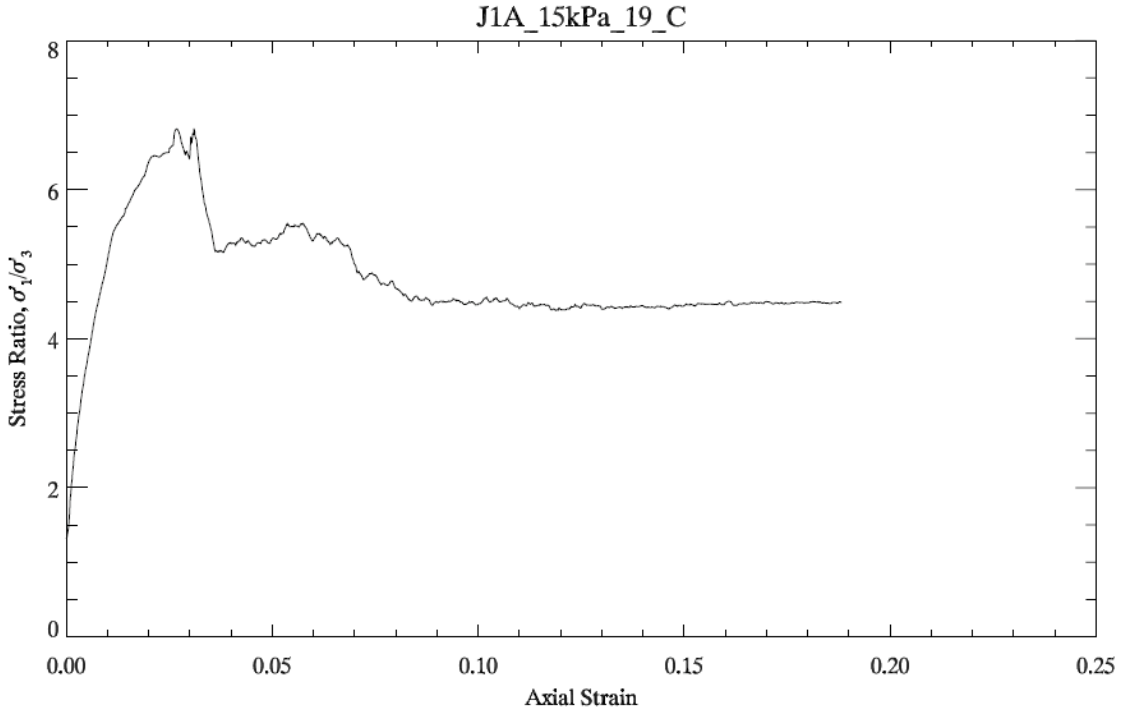

Figure A-27. Behavior of stress ratio as a function of axial strain for density of 1.9 g/cm^3 at 15 kPa confining stress.

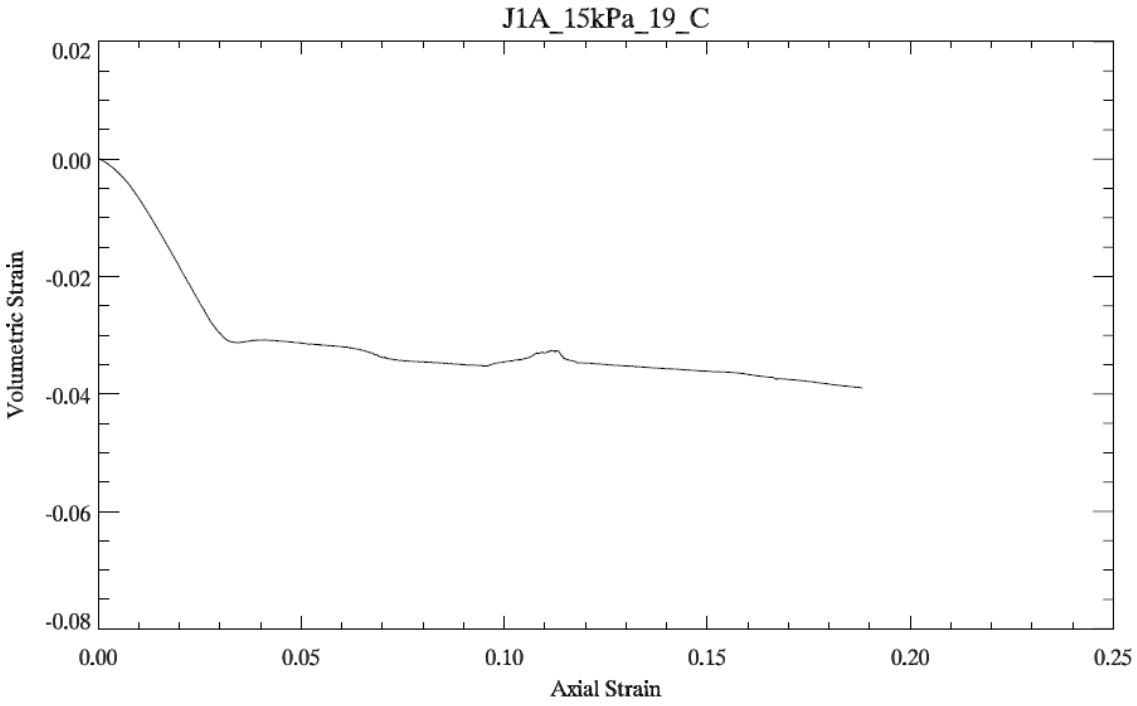

Figure A-28. Volumetric behavior for density of 1.9 g/cm^3 at 15 kPa confining stress

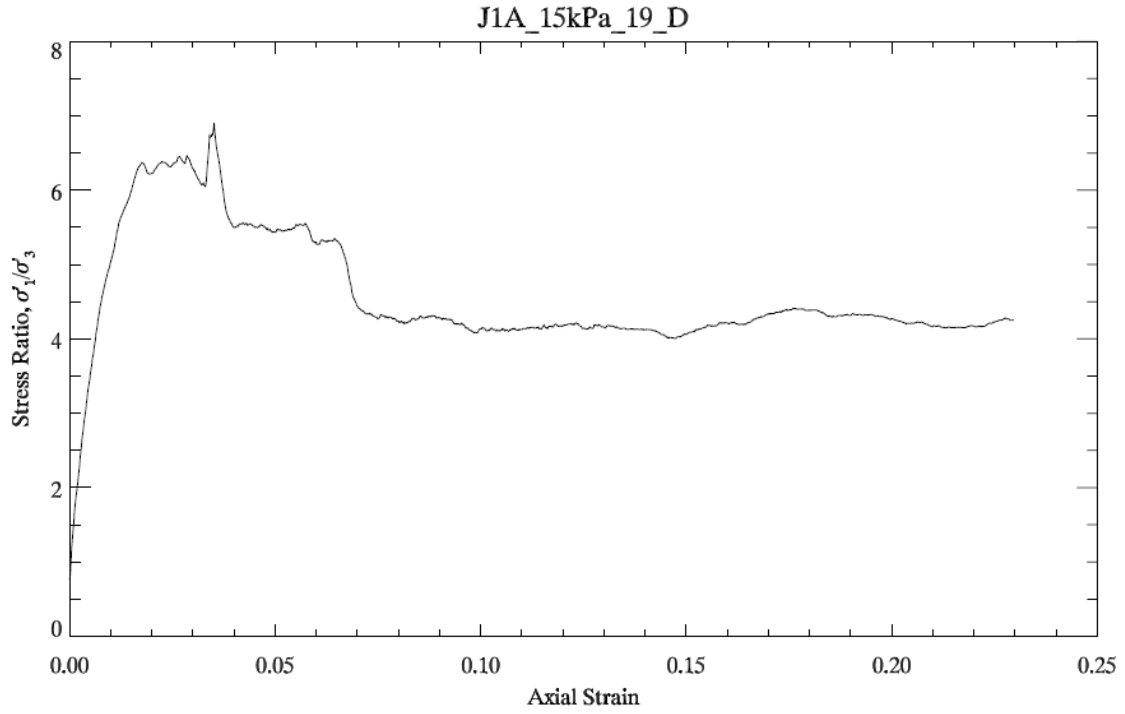

Figure A-29. Behavior of stress ratio as a function of axial strain for density of 1.9 g/cm^3 at 15 kPa confining stress.

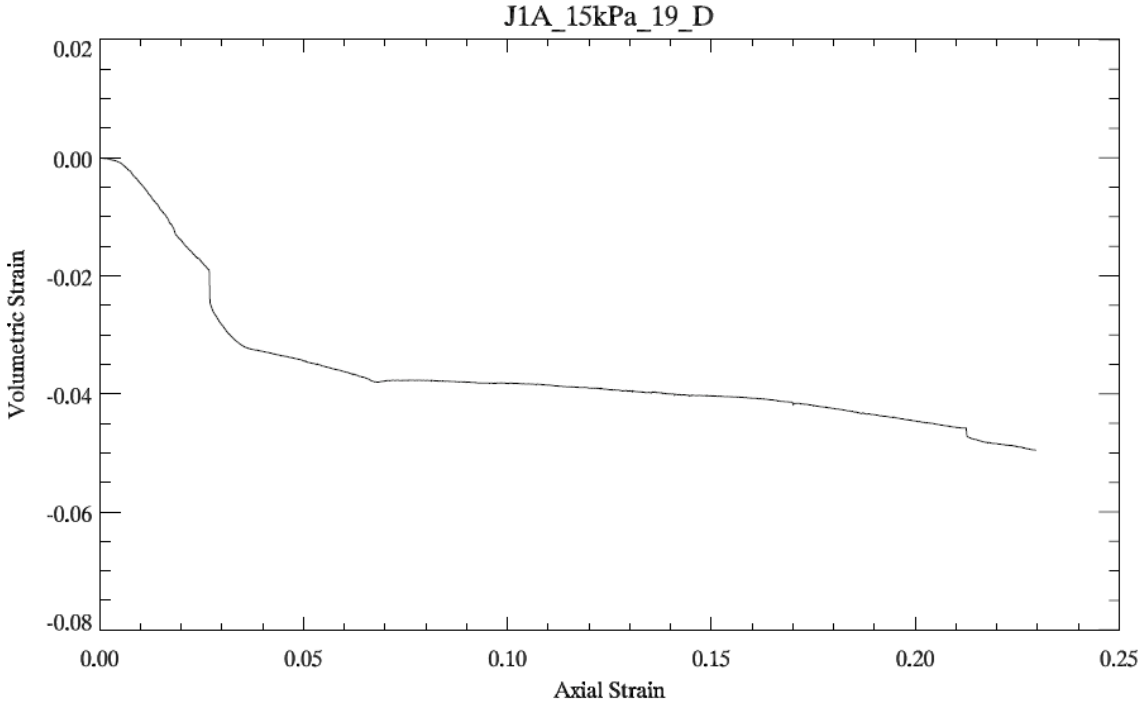

Figure A-30. Volumetric behavior for density of 1.9 g/cm^3 at 15 kPa confining stress

Appendix B

Triaxial tests results of JSC-1A

30 kPa confinement

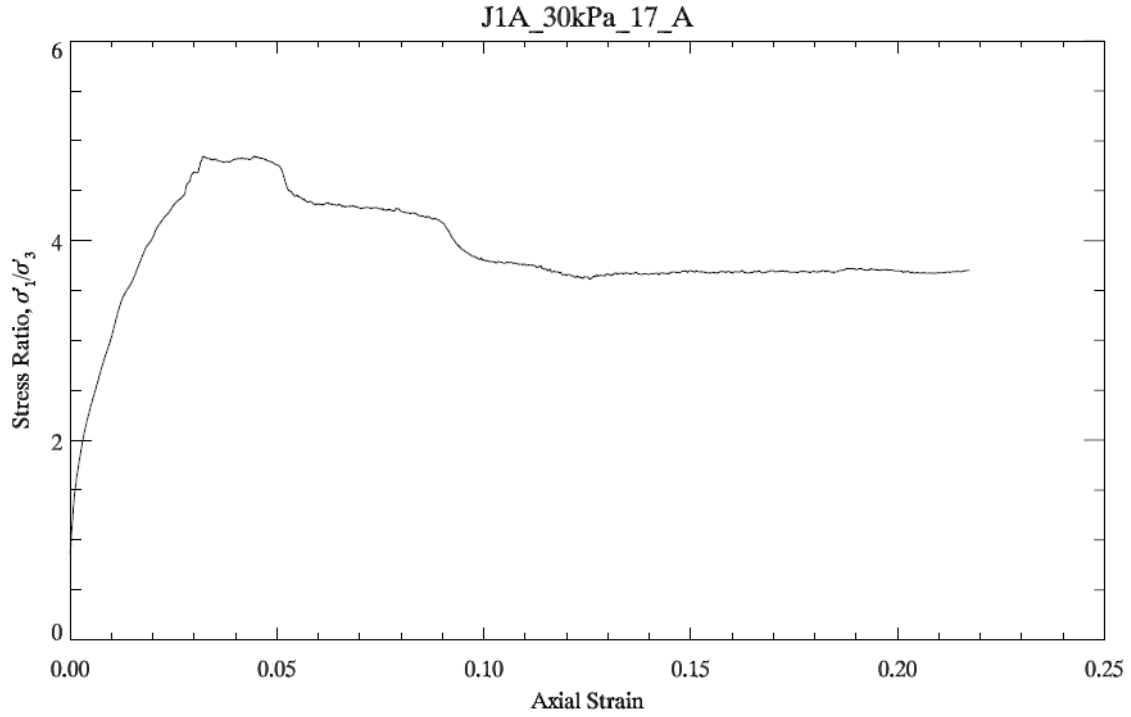

Figure B-1. Behavior of stress ratio as a function of axial strain for density of 1.7 g/cm^3 at 30 kPa confining stress.

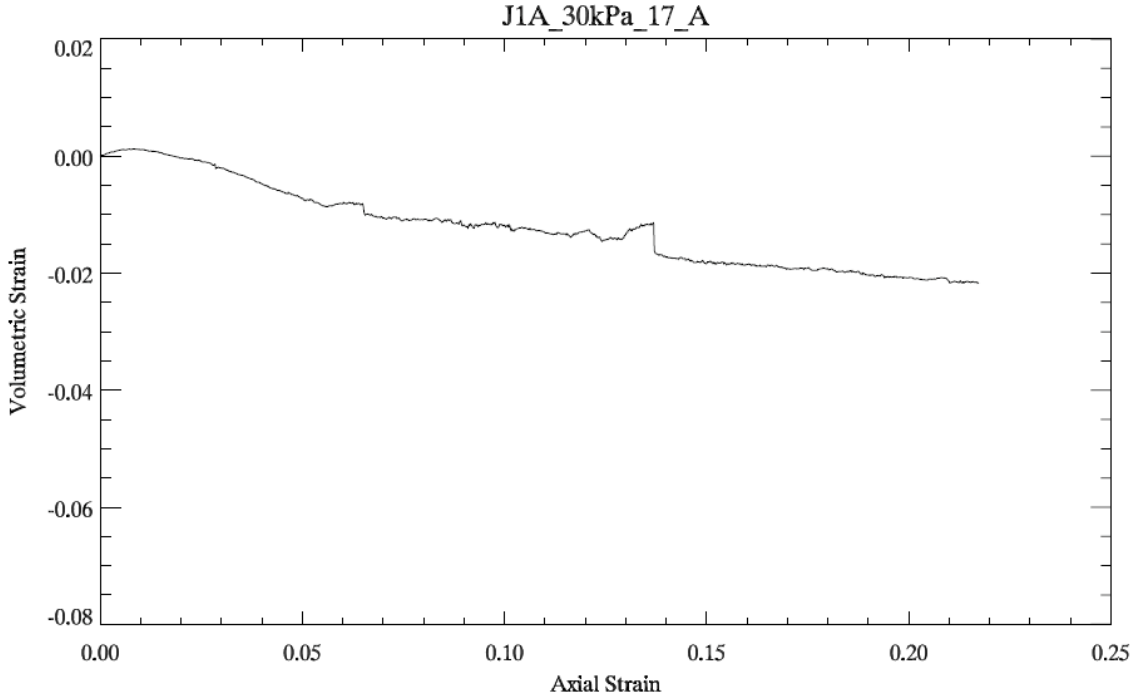

Figure B-2. Volumetric behavior for density of 1.7 g/cm^3 at 30 kPa confining stress

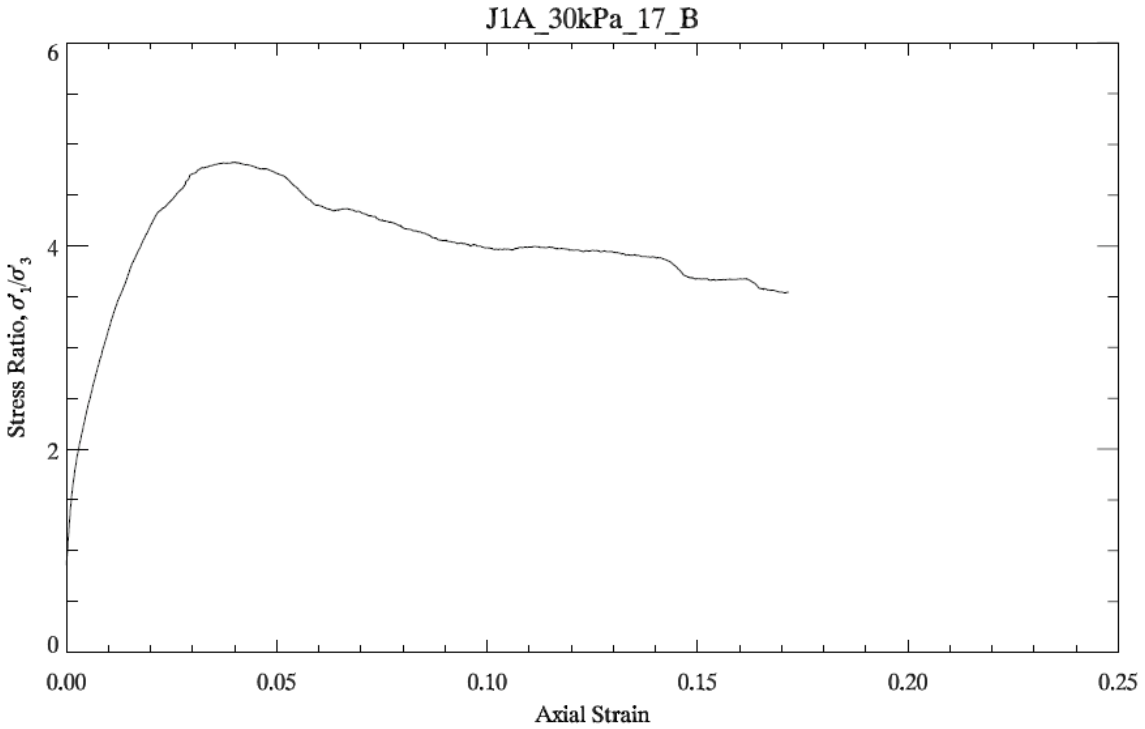

Figure B-3. Behavior of stress ratio as a function of axial strain for density of 1.7 g/cm^3 at 30 kPa confining stress.

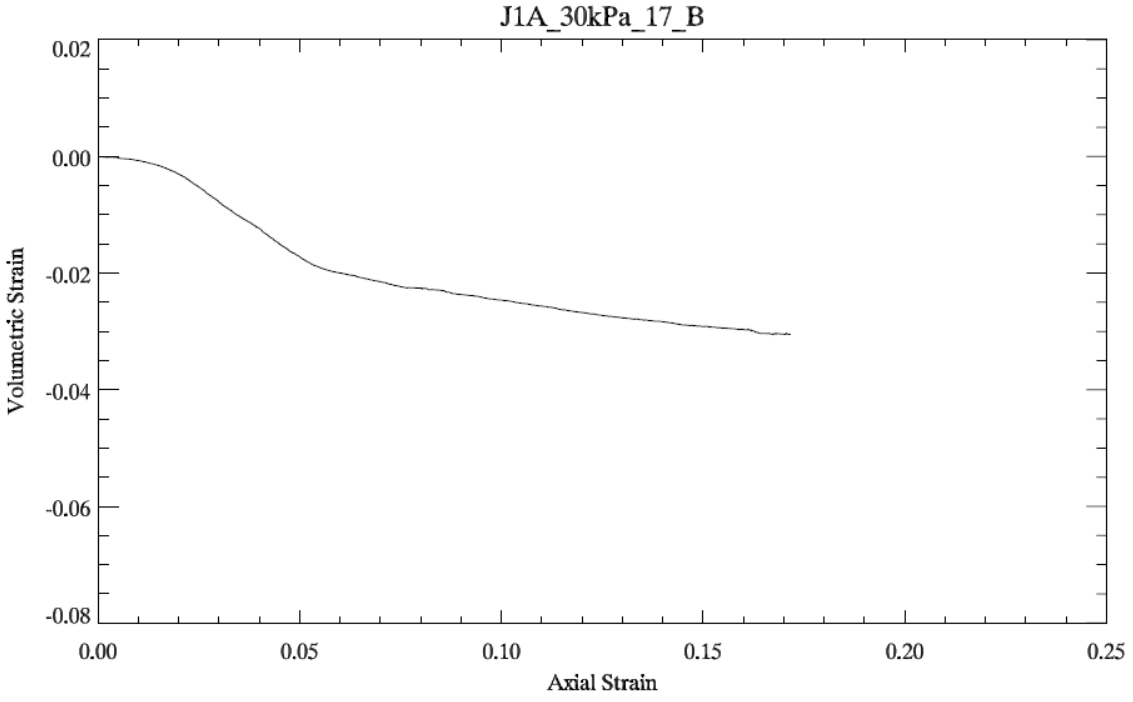

Figure B-4. Volumetric behavior for density of 1.7 g/cm^3 at 30 kPa confining stress

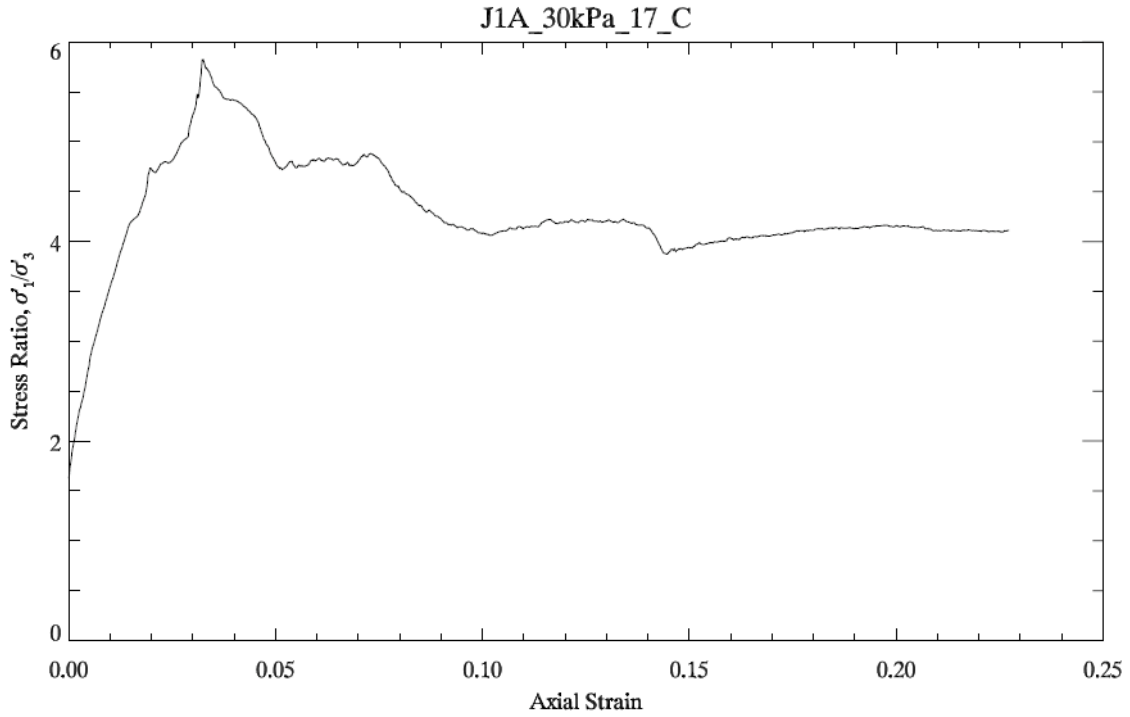

Figure B-5. Behavior of stress ratio as a function of axial strain for density of 1.7 g/cm^3 at 30 kPa confining stress.

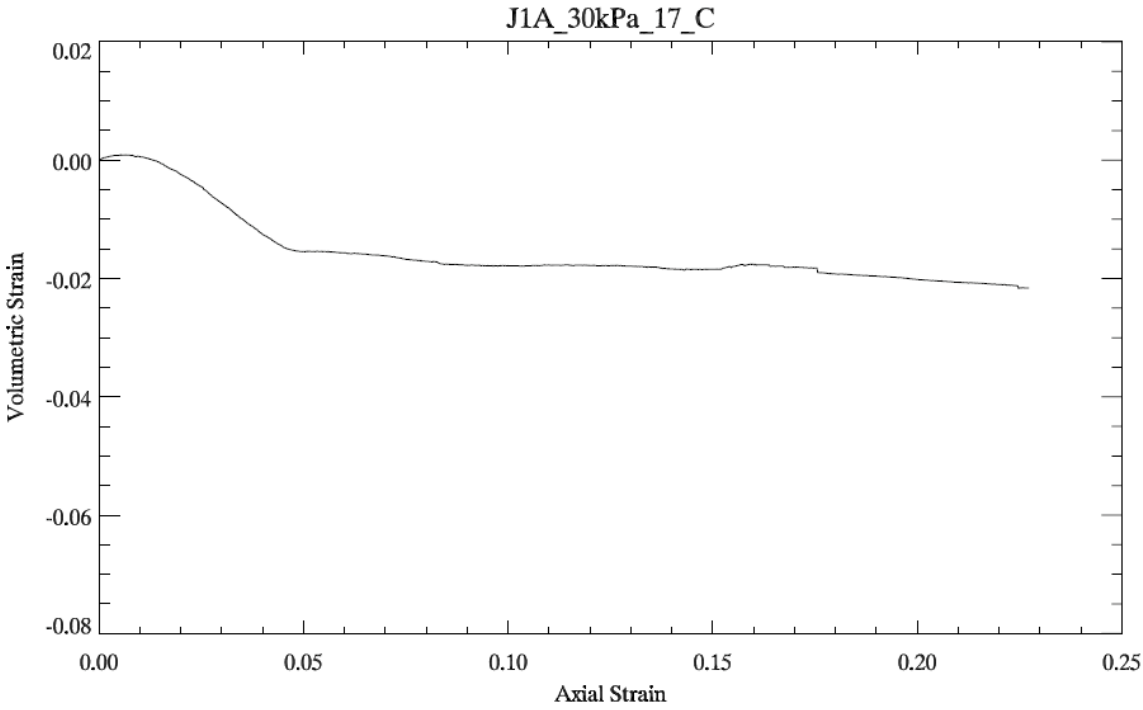

Figure B-6. Volumetric behavior for density of 1.7 g/cm^3 at 30 kPa confining stress

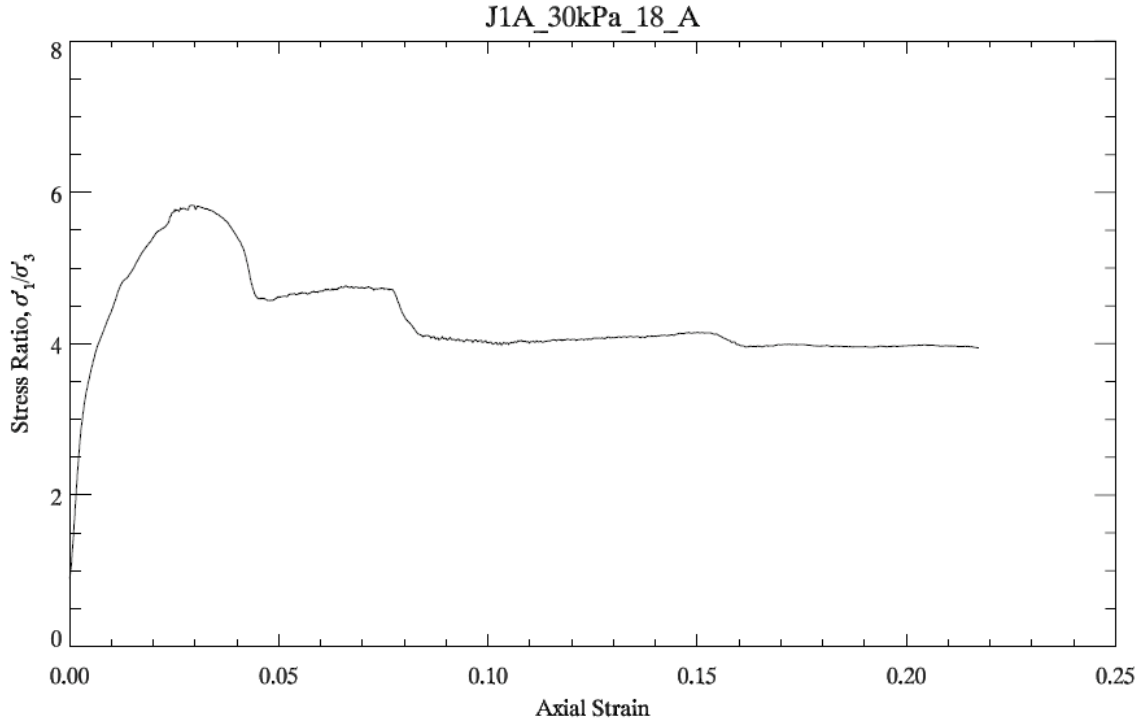

Figure B-7. Behavior of stress ratio as a function of axial strain for density of 1.8 g/cm^3 at 30 kPa confining stress.

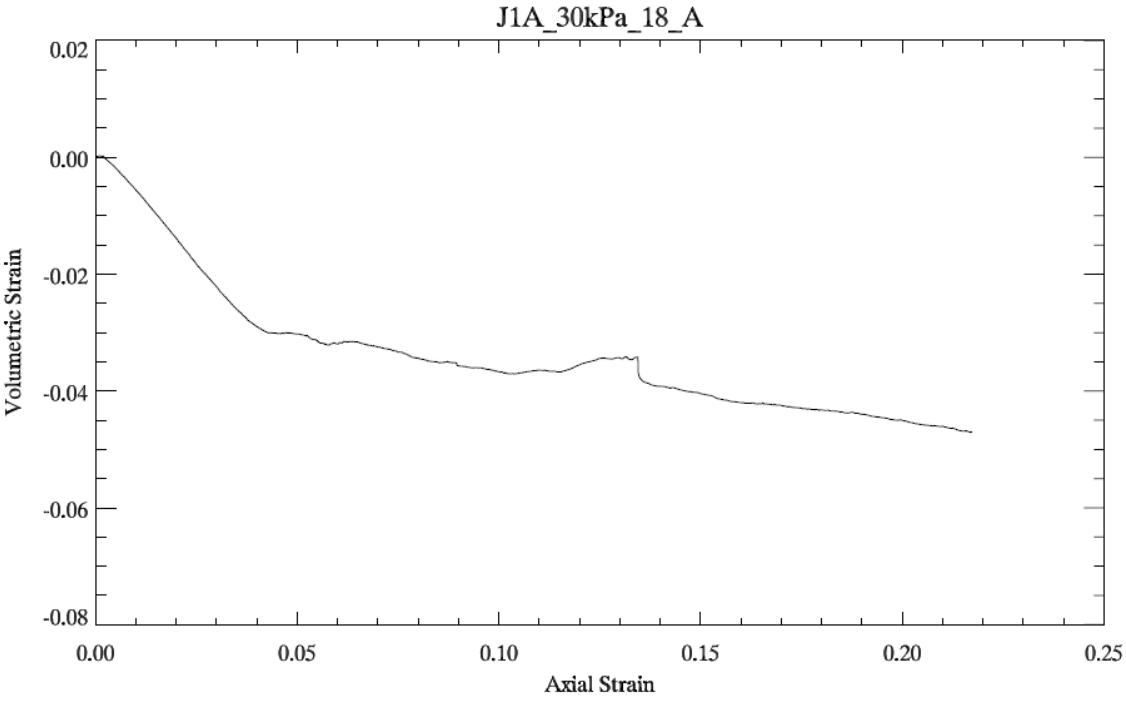

Figure B-8. Volumetric behavior for density of 1.8 g/cm^3 at 30 kPa confining stress

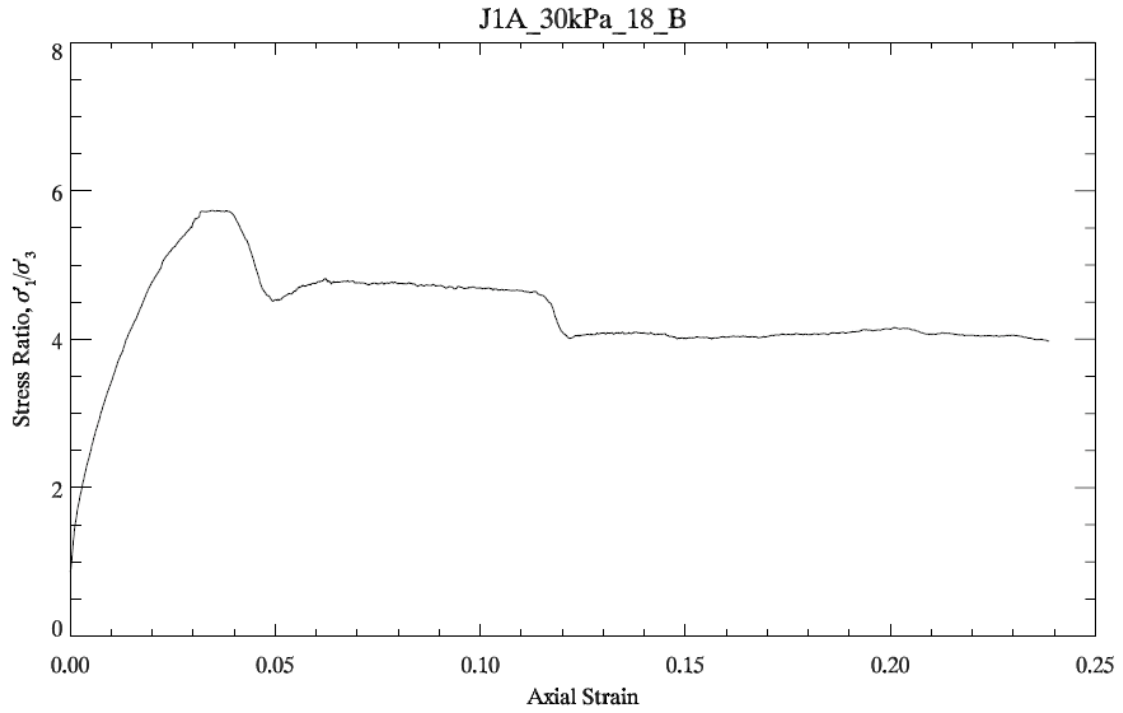

Figure B-9. Behavior of stress ratio as a function of axial strain for density of 1.8 g/cm^3 at 30 kPa confining stress.

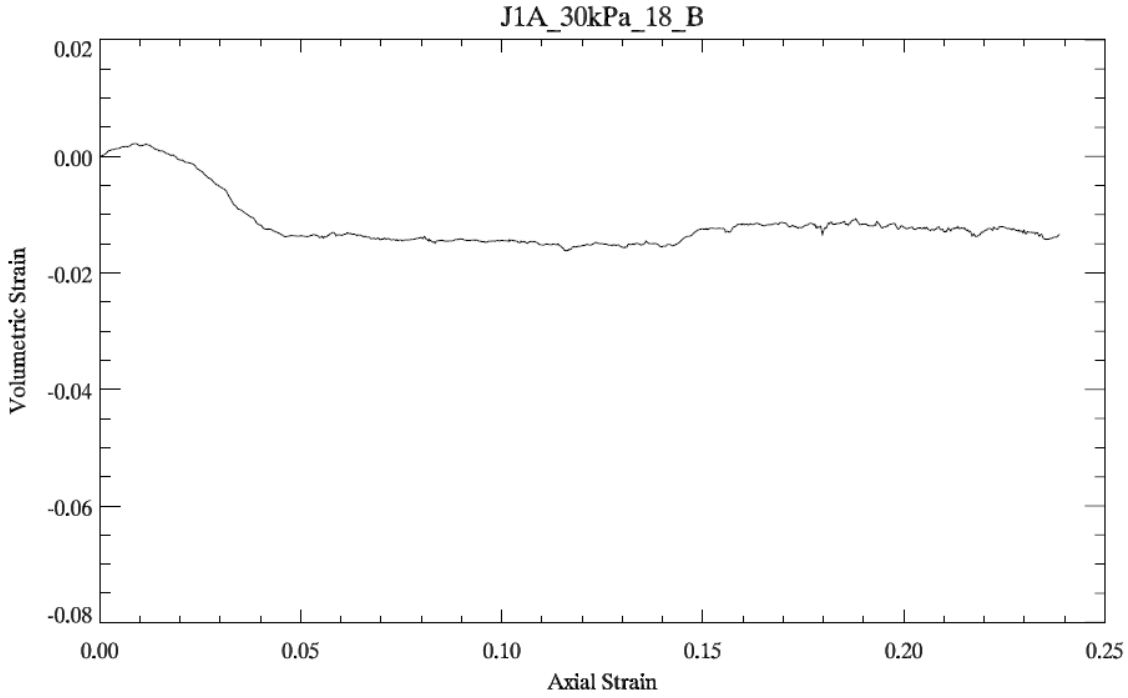

Figure B-10. Volumetric behavior for density of 1.8 g/cm^3 at 30 kPa confining stress

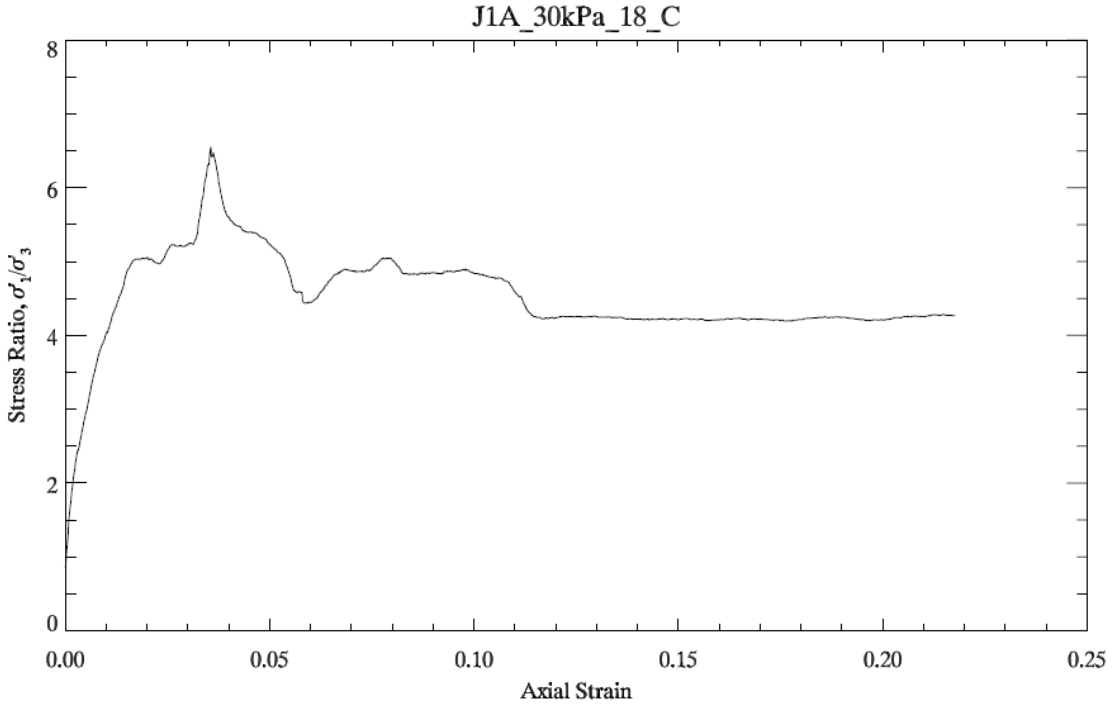

Figure B-11. Behavior of stress ratio as a function of axial strain for density of 1.8 g/cm^3 at 30 kPa confining stress.

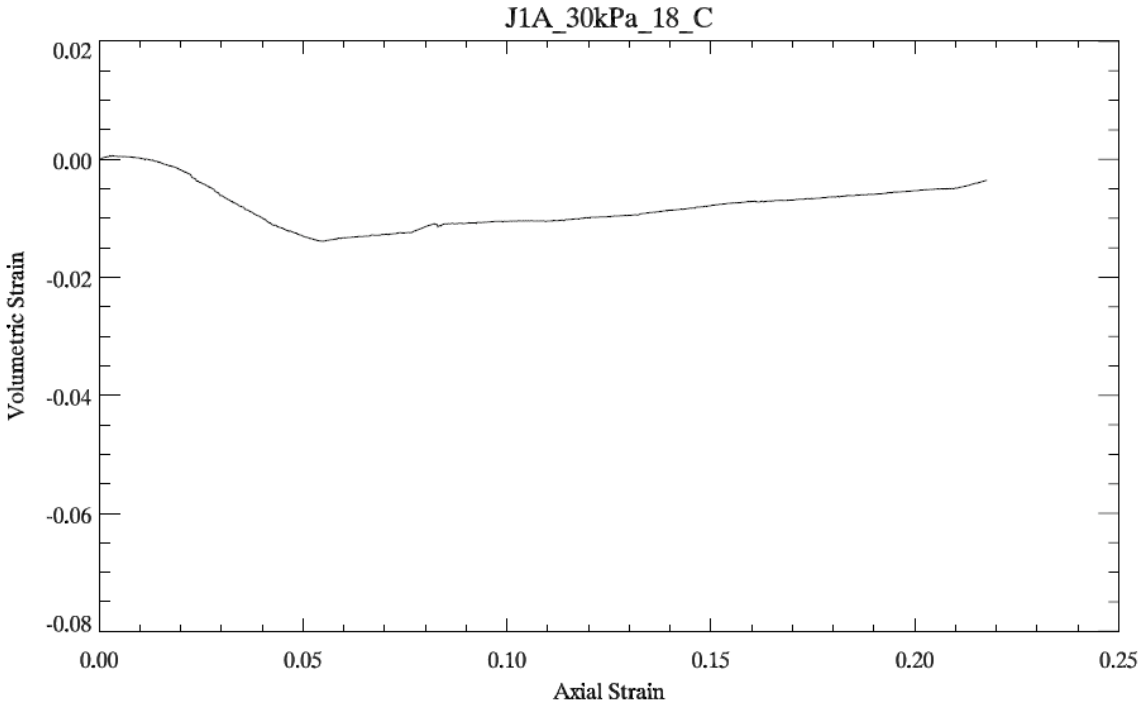

Figure B-12. Volumetric behavior for density of 1.8 g/cm^3 at 30 kPa confining stress

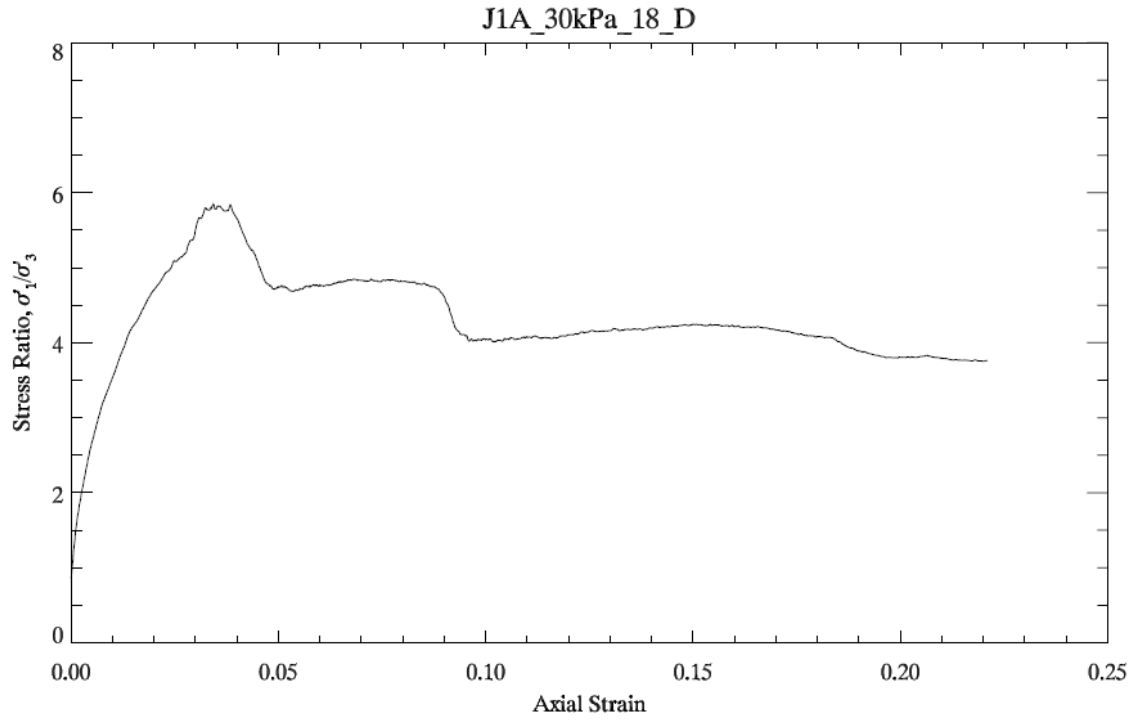

Figure B-13. Behavior of stress ratio as a function of axial strain for density of 1.8 g/cm^3 at 30 kPa confining stress.

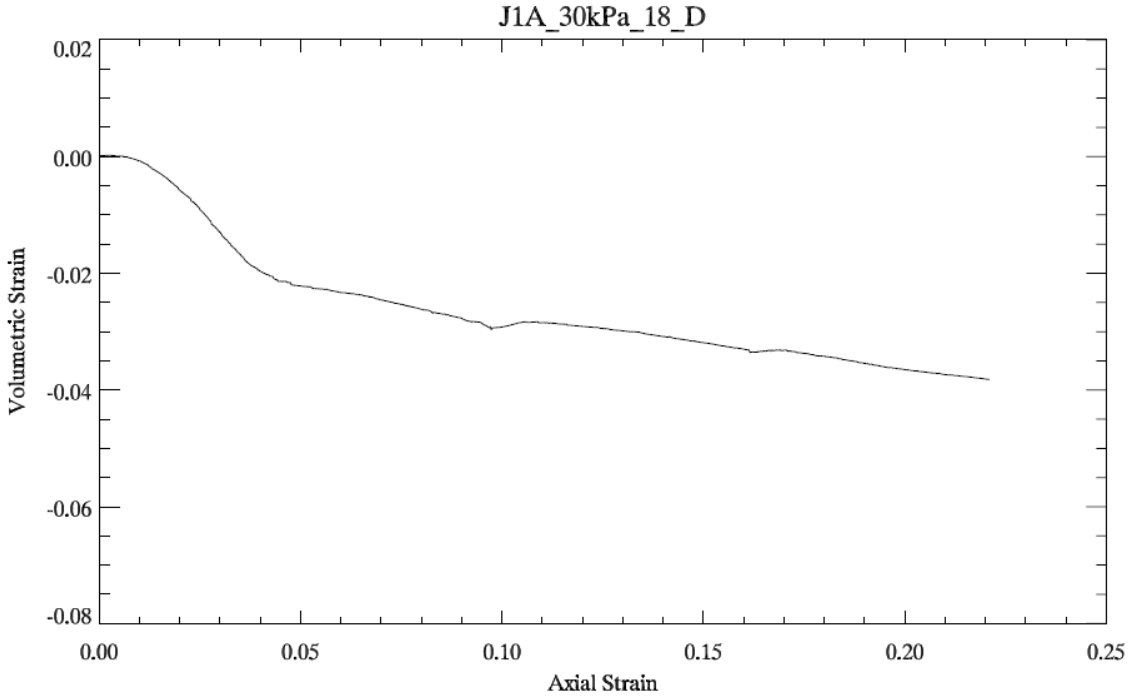

Figure B-14. Volumetric behavior for density of 1.8 g/cm^3 at 30 kPa confining stress

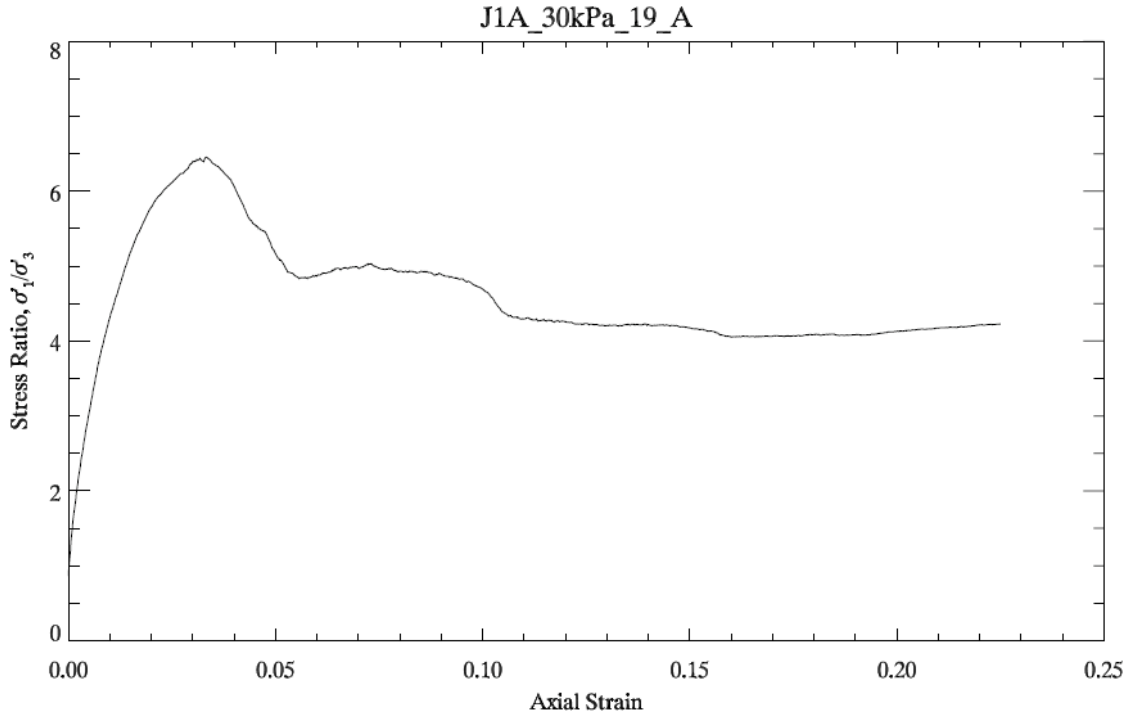

Figure B-15. Behavior of stress ratio as a function of axial strain for density of 1.9 g/cm^3 at 30 kPa confining stress.

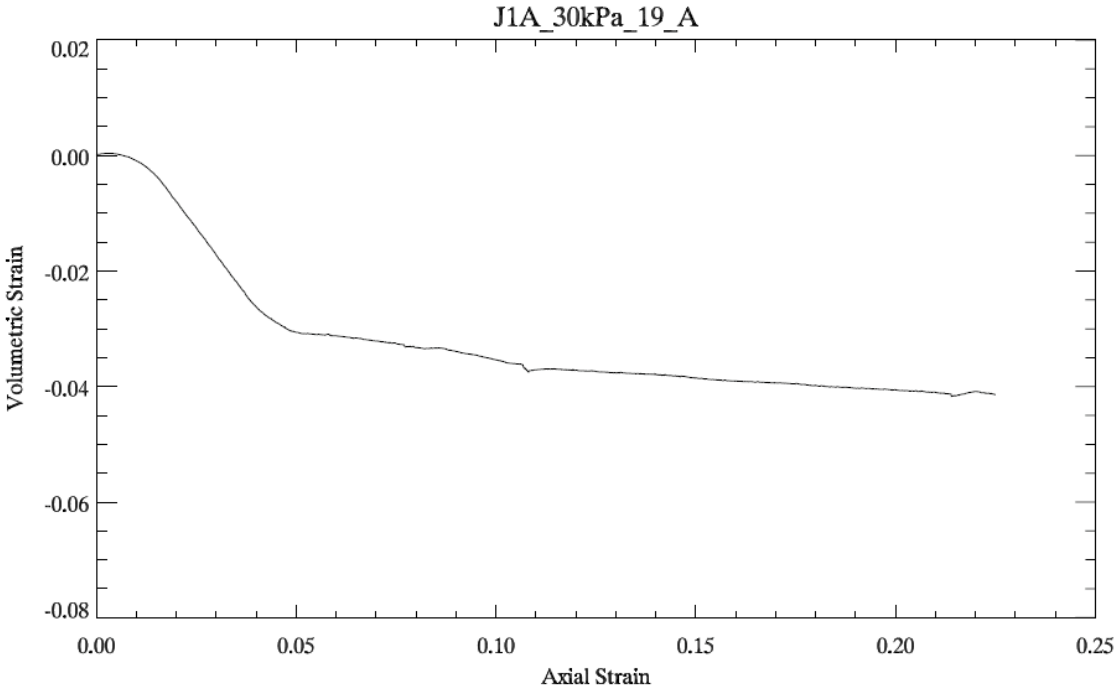

Figure B-16. Volumetric behavior for density of 1.9 g/cm^3 at 30 kPa confining stress

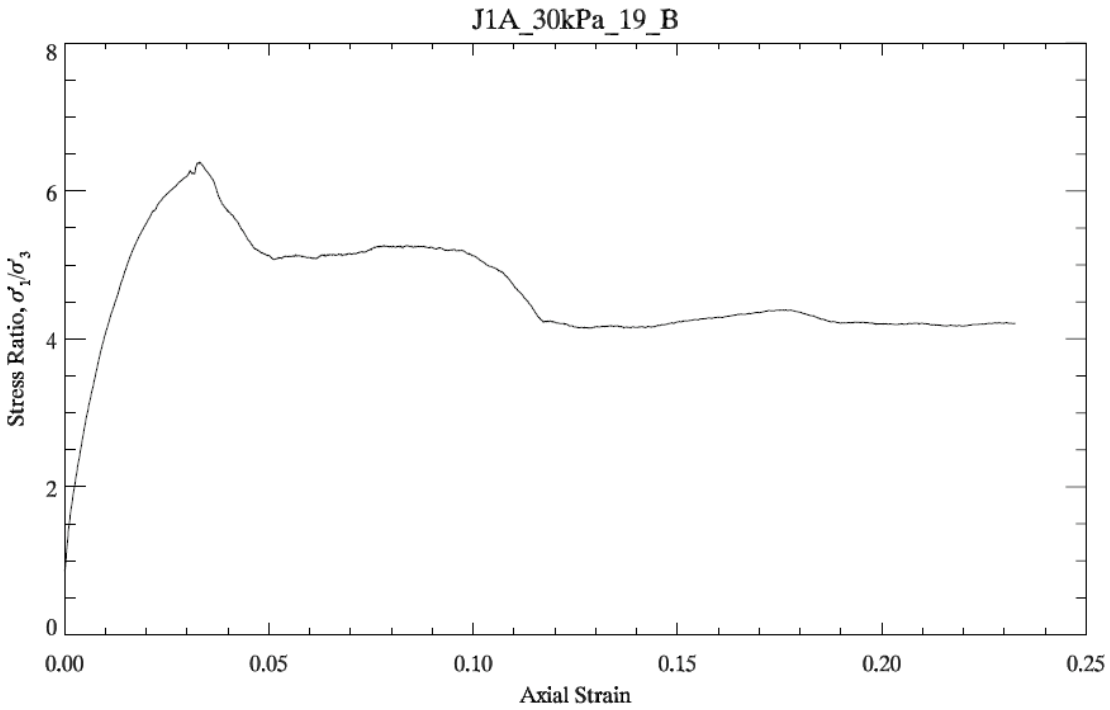

Figure B-17. Behavior of stress ratio as a function of axial strain for density of 1.9 g/cm^3 at 30 kPa confining stress.

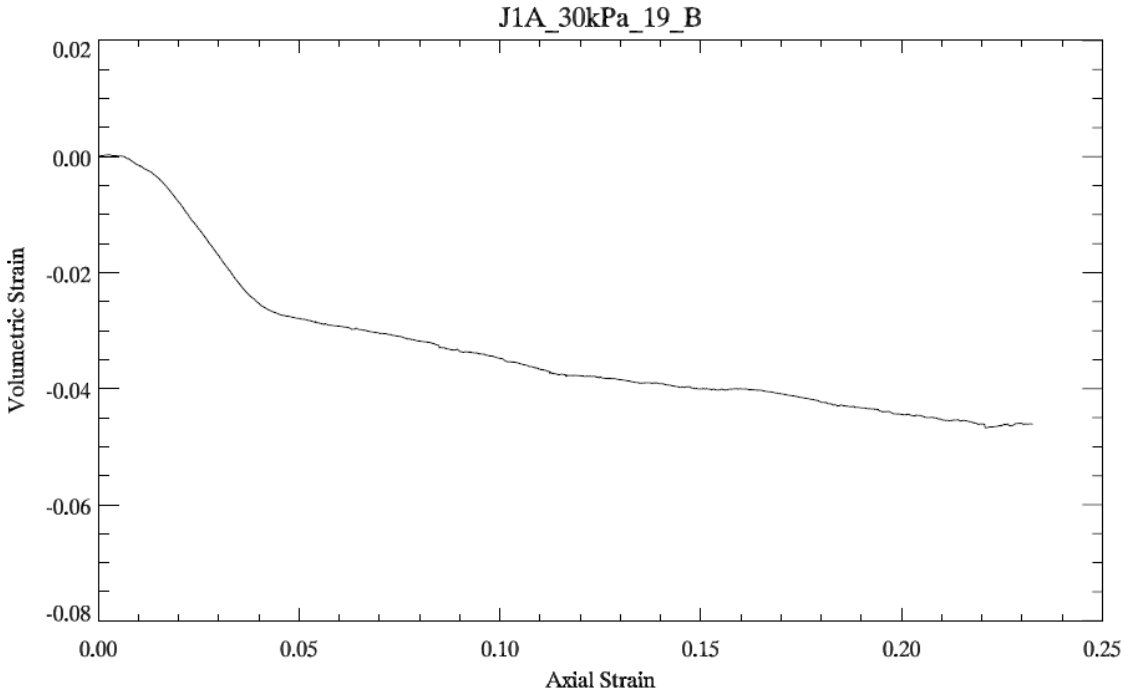

Figure B-18. Volumetric behavior for density of 1.9 g/cm^3 at 30 kPa confining stress

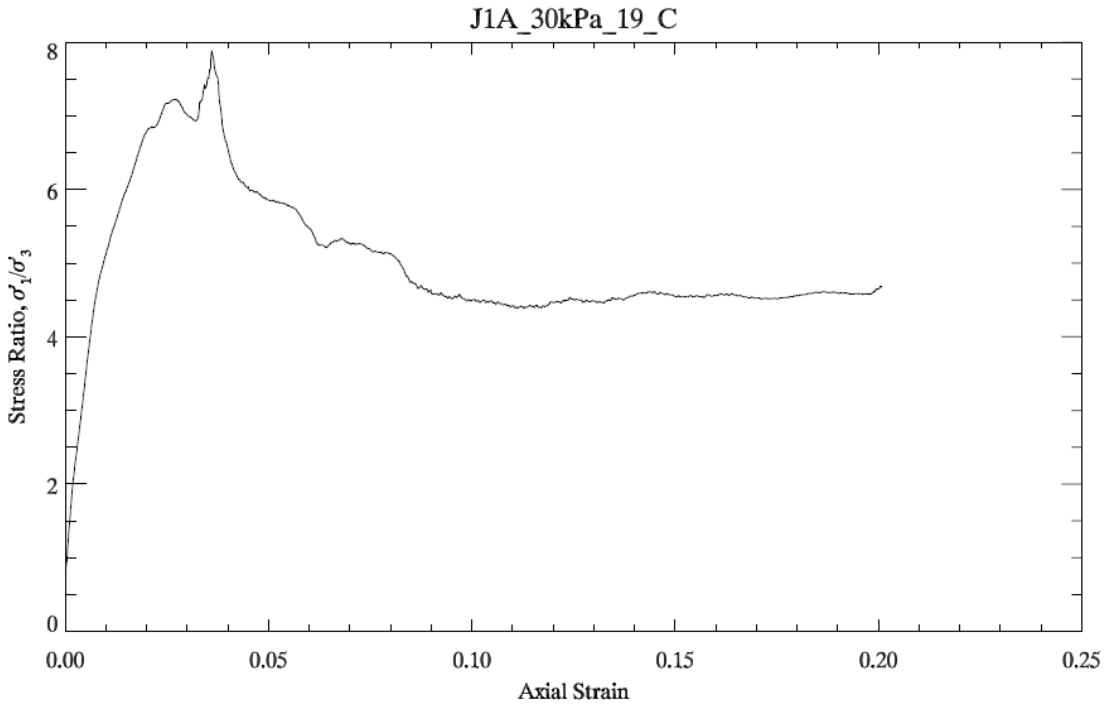

Figure B-19. Behavior of stress ratio as a function of axial strain for density of 1.9 g/cm^3 at 30 kPa confining stress.

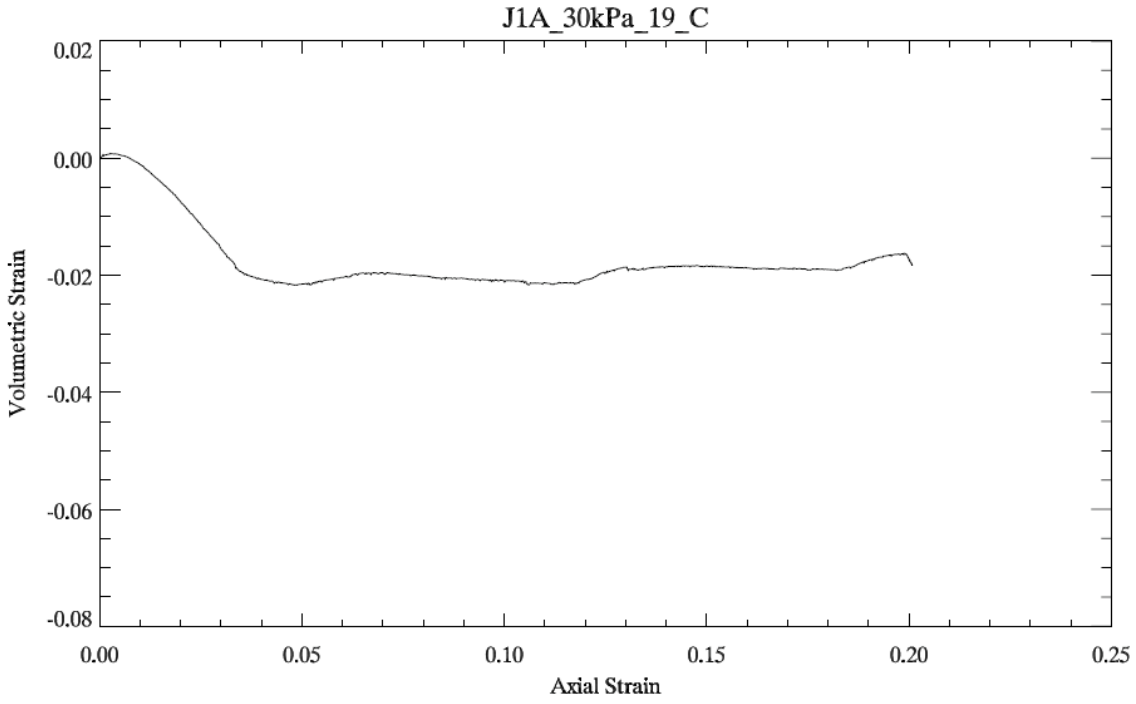

Figure B-20. Volumetric behavior for density of 1.9 g/cm^3 at 30 kPa confining stress

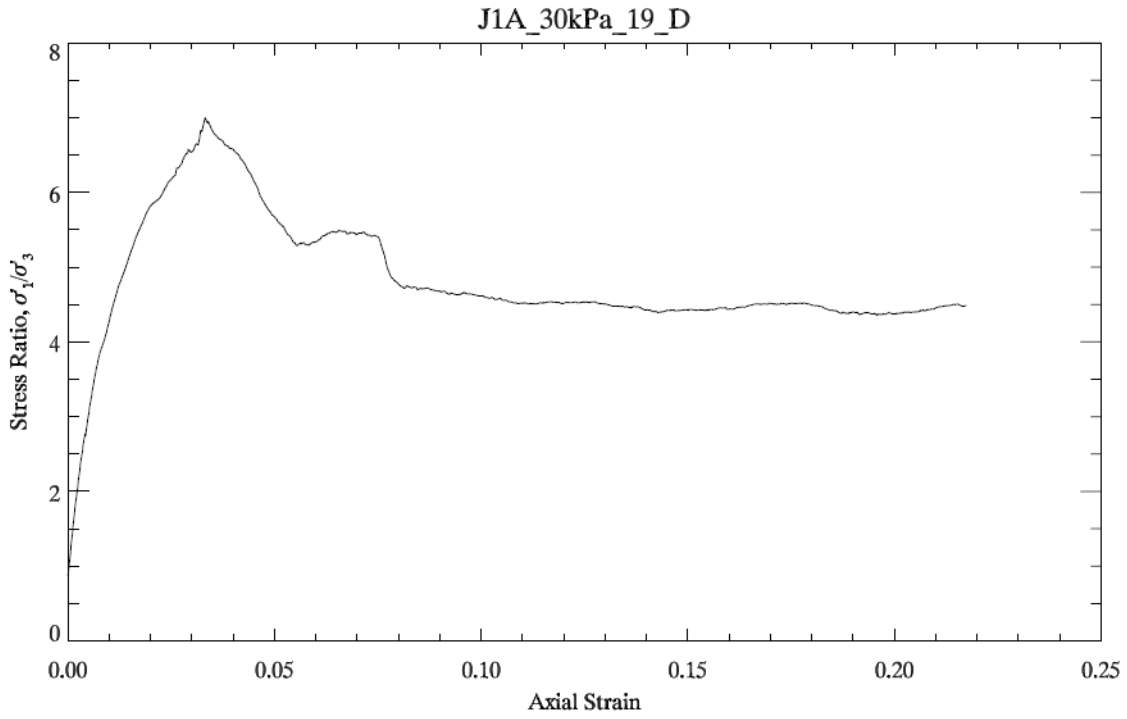

Figure B-21. Behavior of stress ratio as a function of axial strain for density of 1.9 g/cm^3 at 30 kPa confining stress.

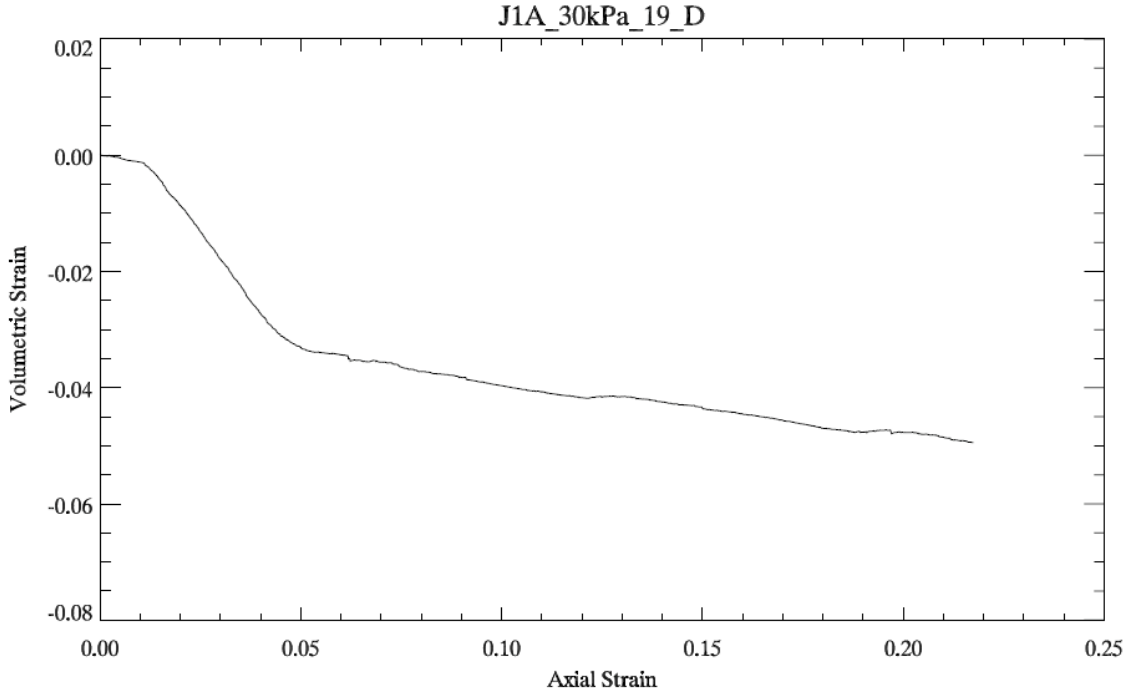

Figure B-22. Volumetric behavior for density of 1.9 g/cm^3 at 30 kPa confining stress

Appendix C

Triaxial tests results of JSC-1A

60 kPa confinement

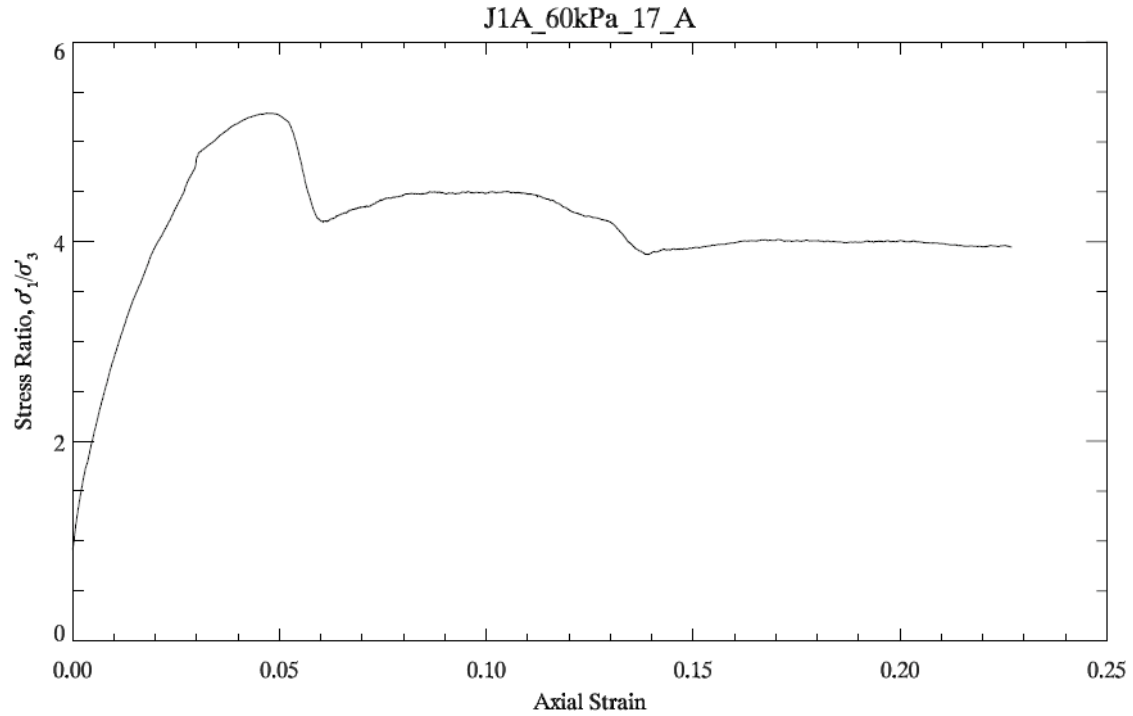

Figure C-1. Behavior of stress ratio as a function of axial strain for density of 1.7 g/cm^3 at 60 kPa confining stress.

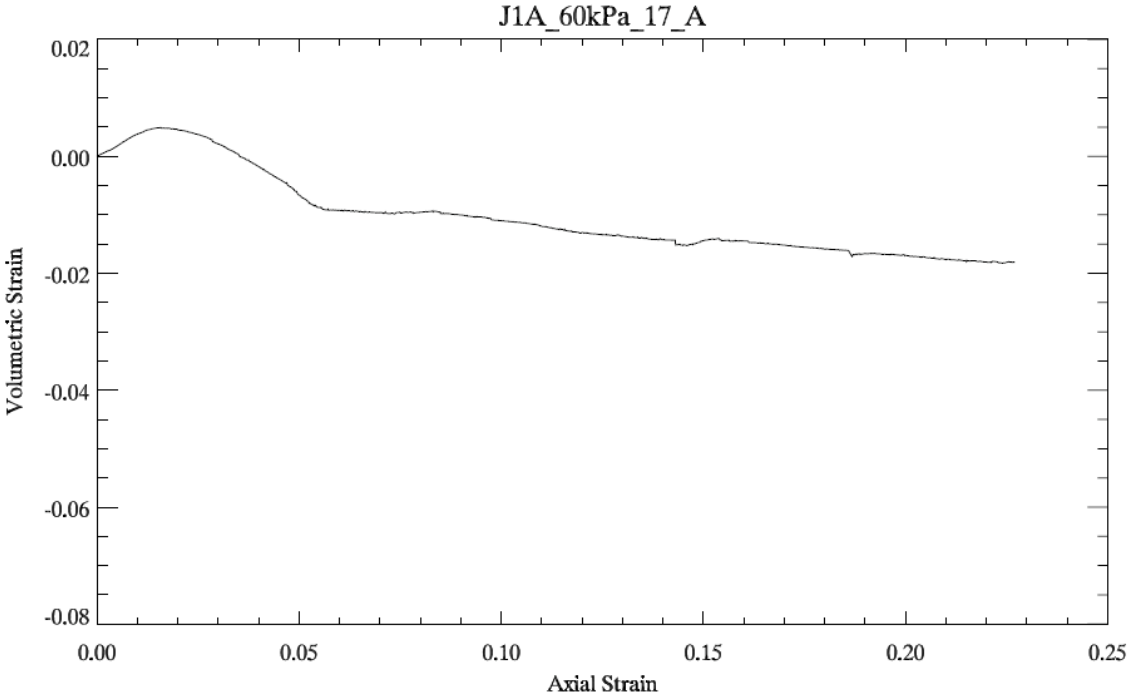

Figure C-2. Volumetric behavior for density of 1.7 g/cm^3 at 60 kPa confining stress

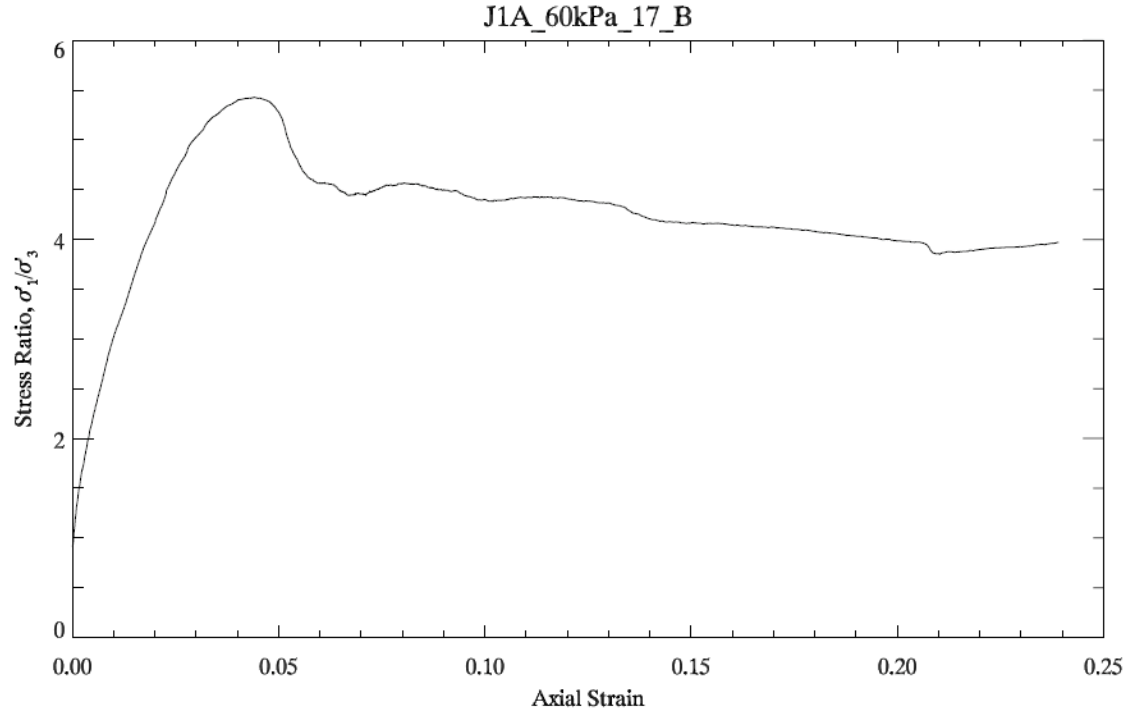

Figure C-3. Behavior of stress ratio as a function of axial strain for density of 1.7 g/cm^3 at 60 kPa confining stress.

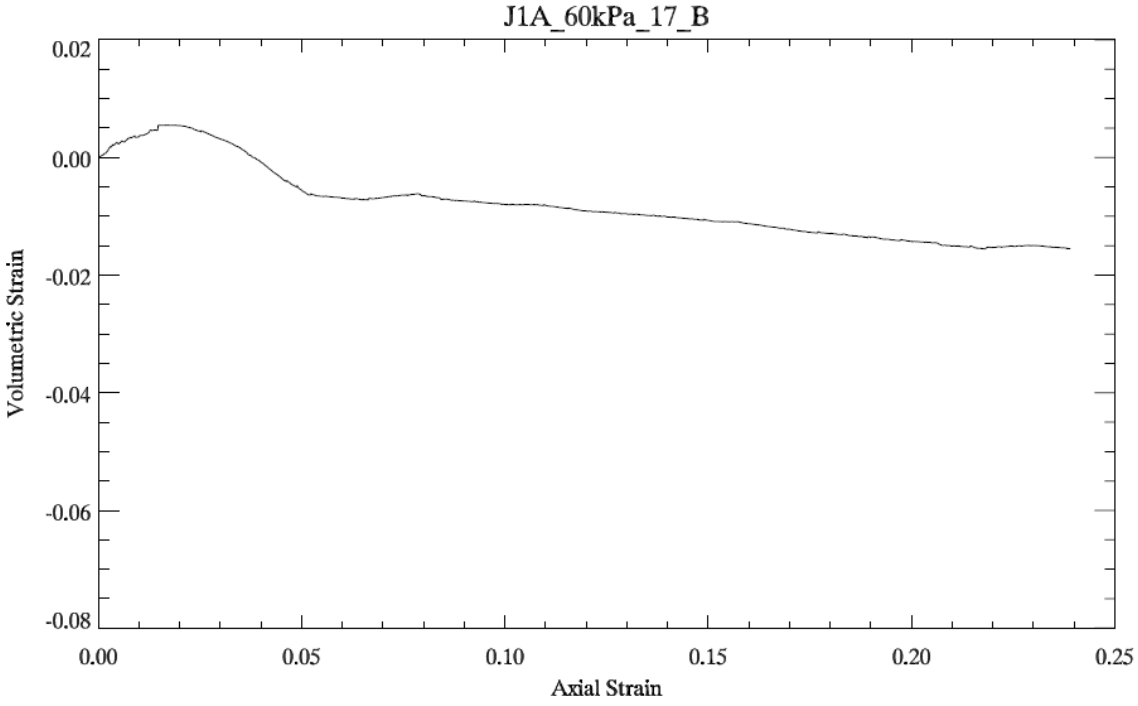

Figure C-4. Volumetric behavior for density of 1.7 g/cm^3 at 60 kPa confining stress

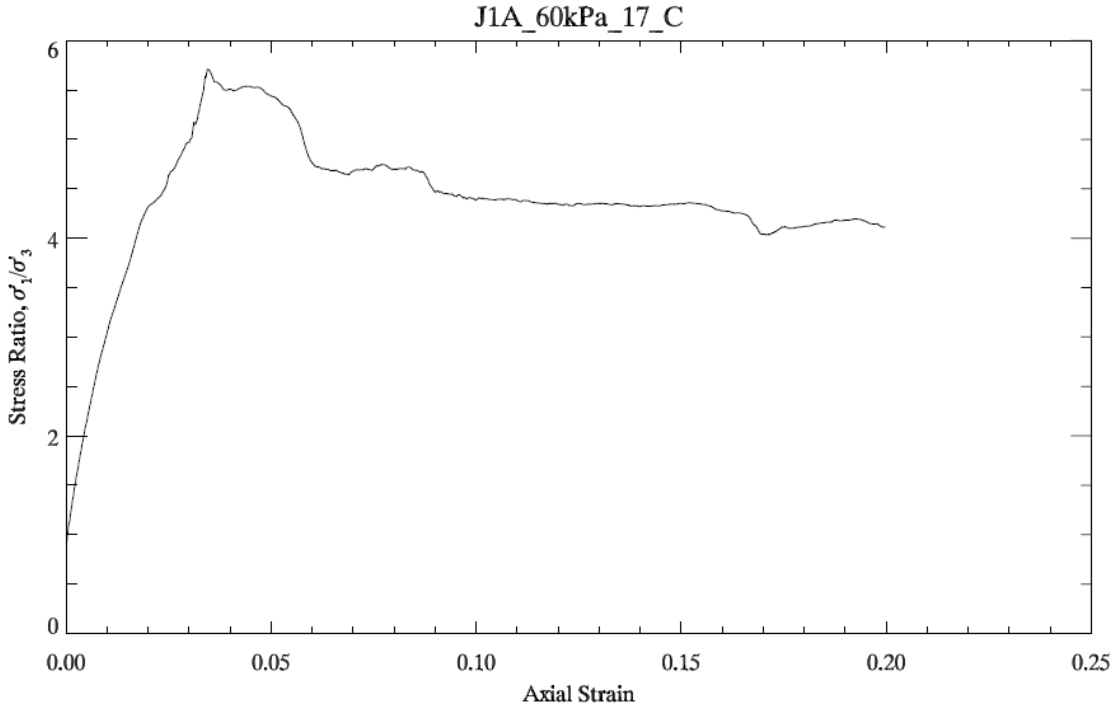

Figure C-5. Behavior of stress ratio as a function of axial strain for density of 1.7 g/cm^3 at 60 kPa confining stress.

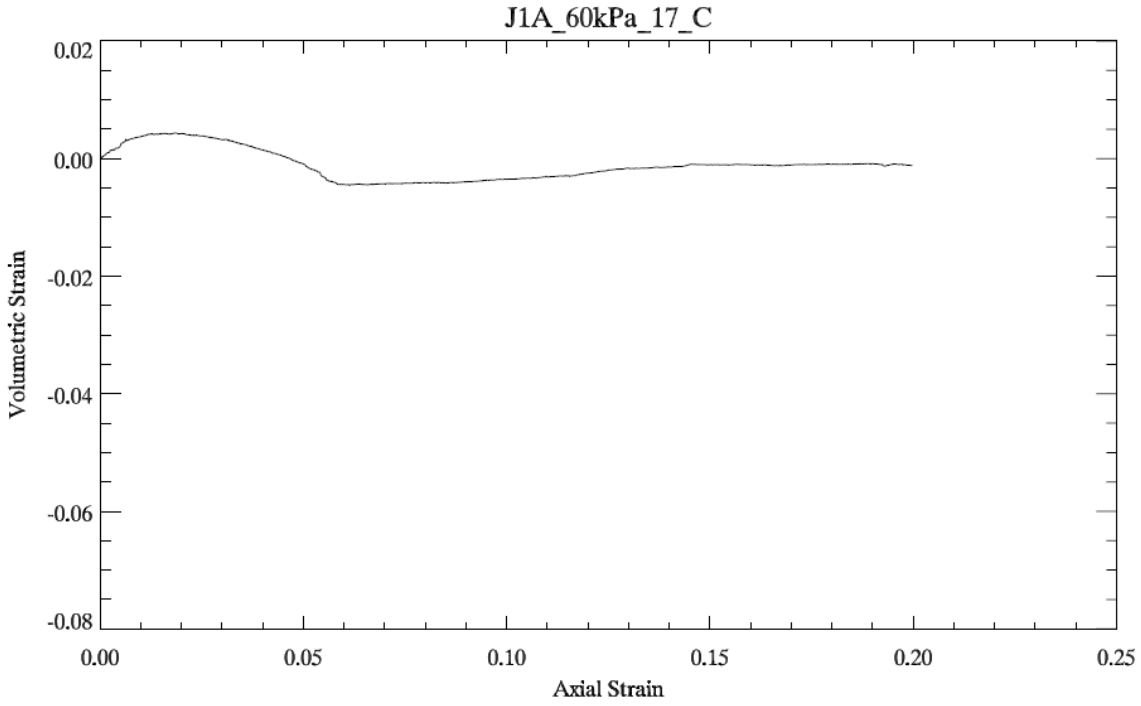

Figure C-6. Volumetric behavior for density of 1.7 g/cm^3 at 60 kPa confining stress

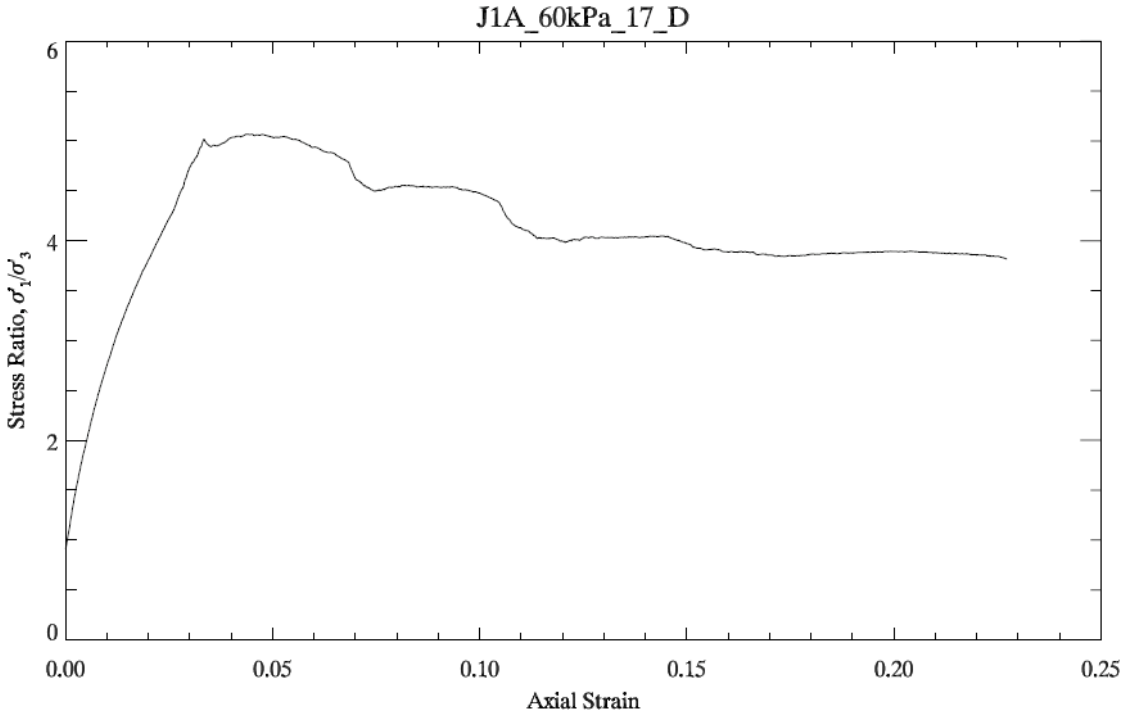

Figure C-7. Behavior of stress ratio as a function of axial strain for density of 1.7 g/cm^3 at 60 kPa confining stress.

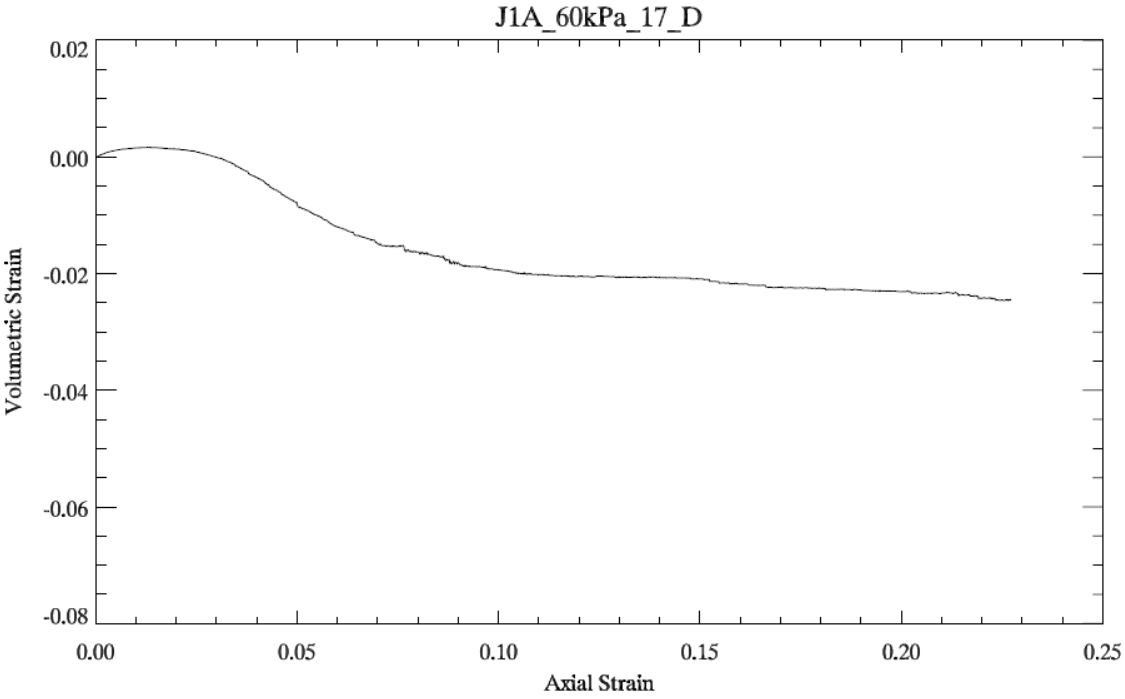

Figure C-8. Volumetric behavior for density of 1.7 g/cm^3 at 60 kPa confining stress

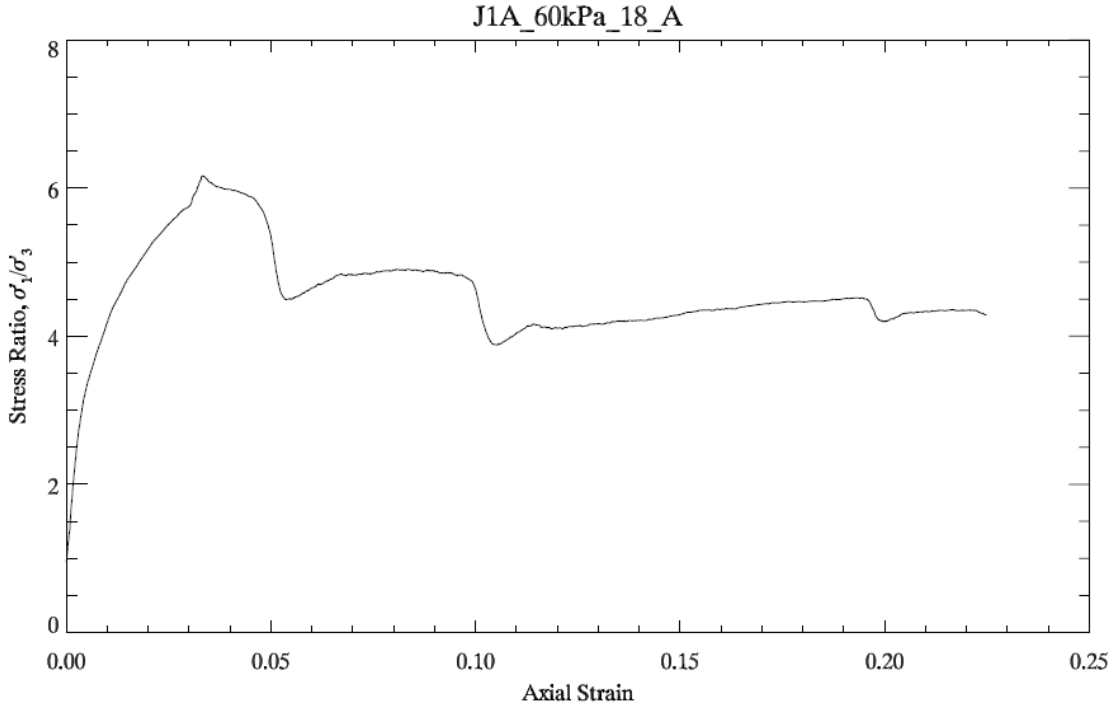

Figure C-9. Behavior of stress ratio as a function of axial strain for density of 1.8 g/cm^3 at 60 kPa confining stress.

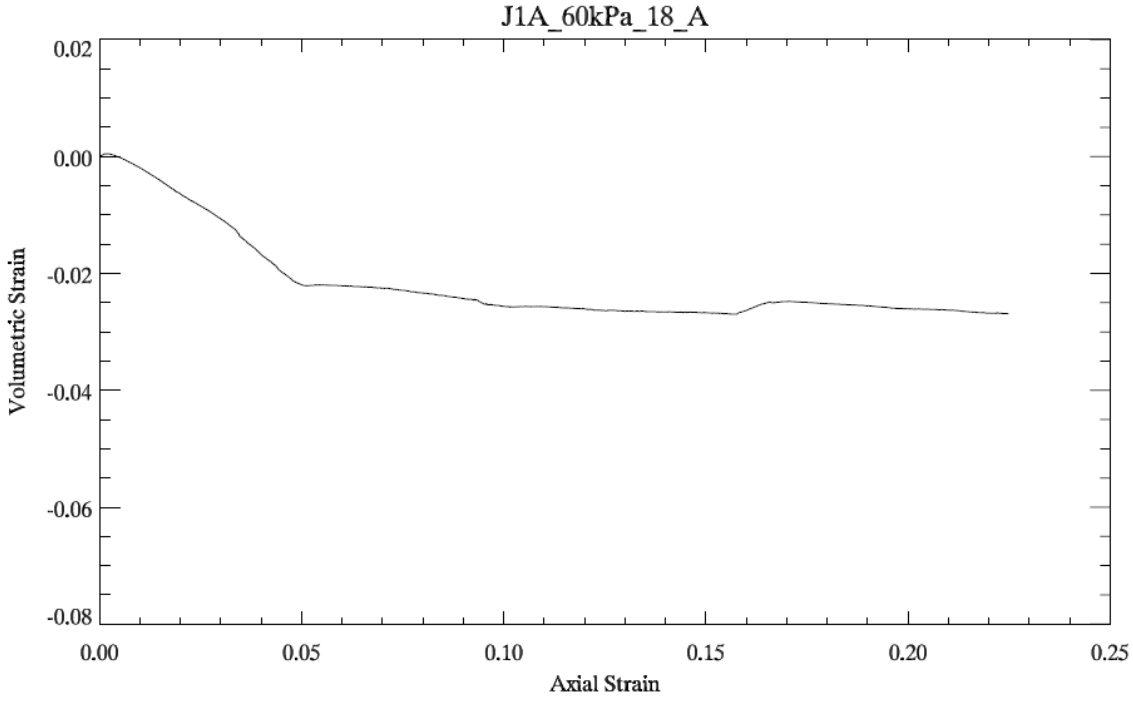

Figure C-10. Volumetric behavior for density of 1.8 g/cm^3 at 60 kPa confining stress

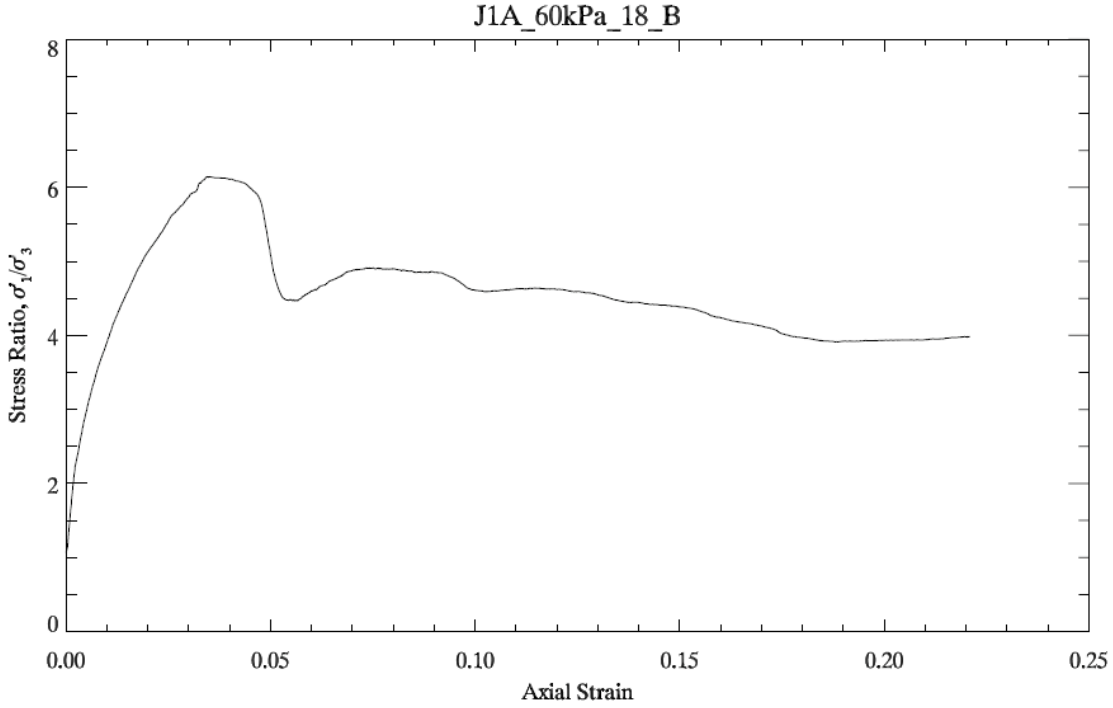

Figure C-11. Behavior of stress ratio as a function of axial strain for density of 1.8 g/cm^3 at 60 kPa confining stress.

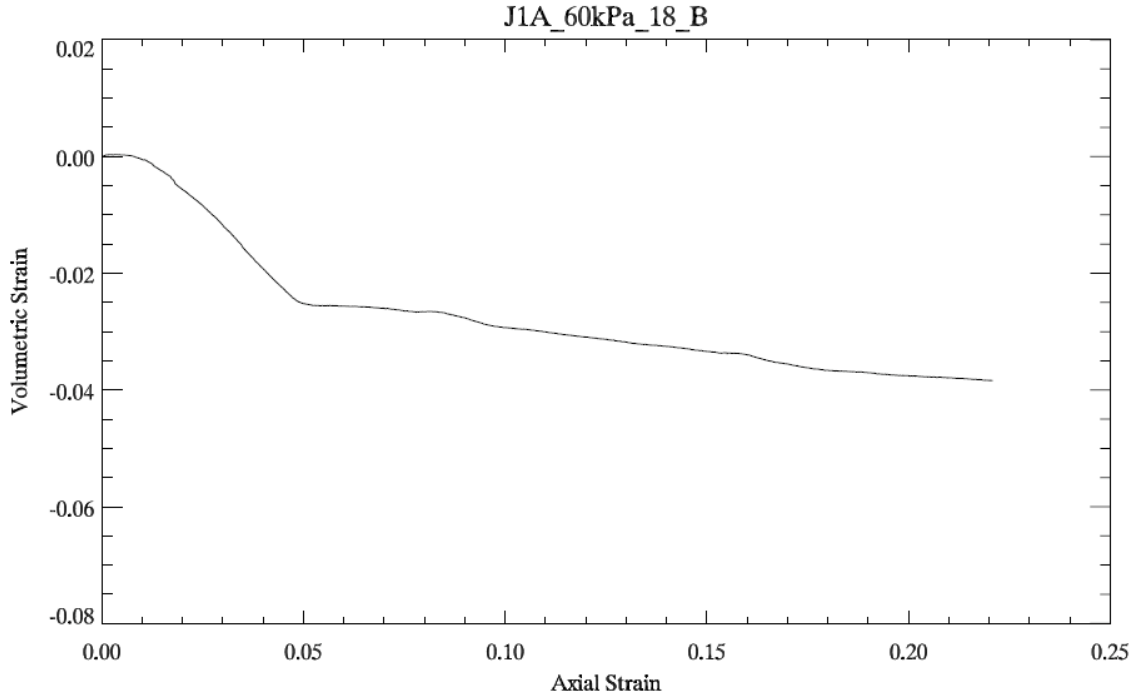

Figure C-12. Volumetric behavior for density of 1.8 g/cm^3 at 60 kPa confining stress

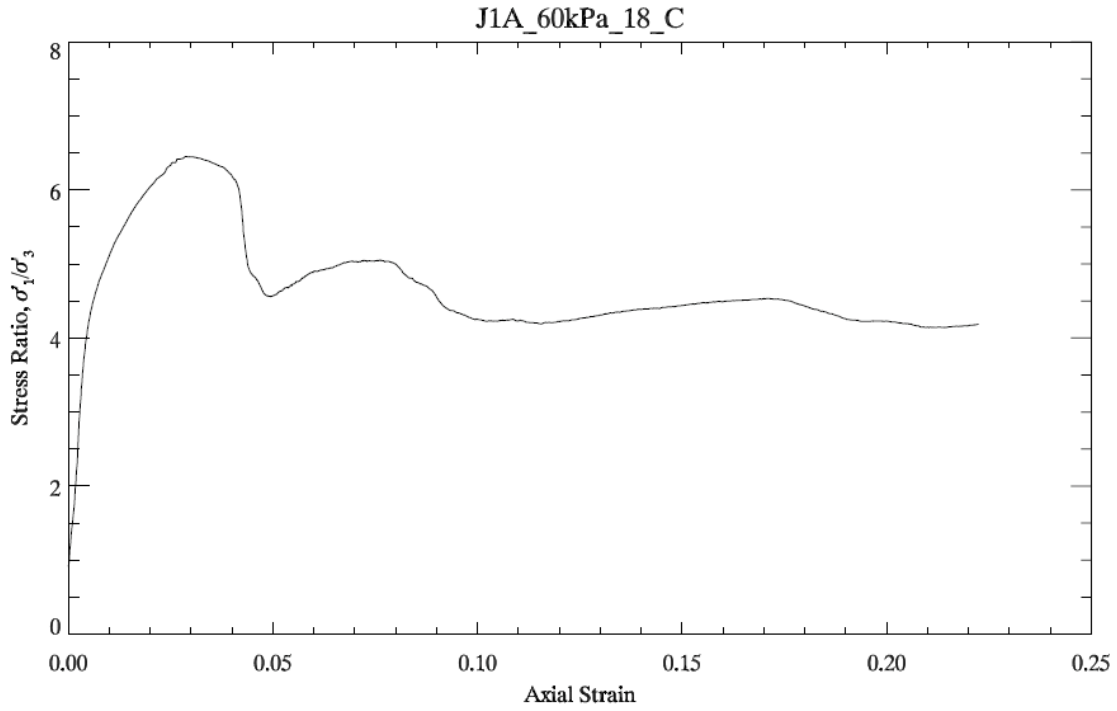

Figure C-13. Behavior of stress ratio as a function of axial strain for density of 1.8 g/cm^3 at 60 kPa confining stress.

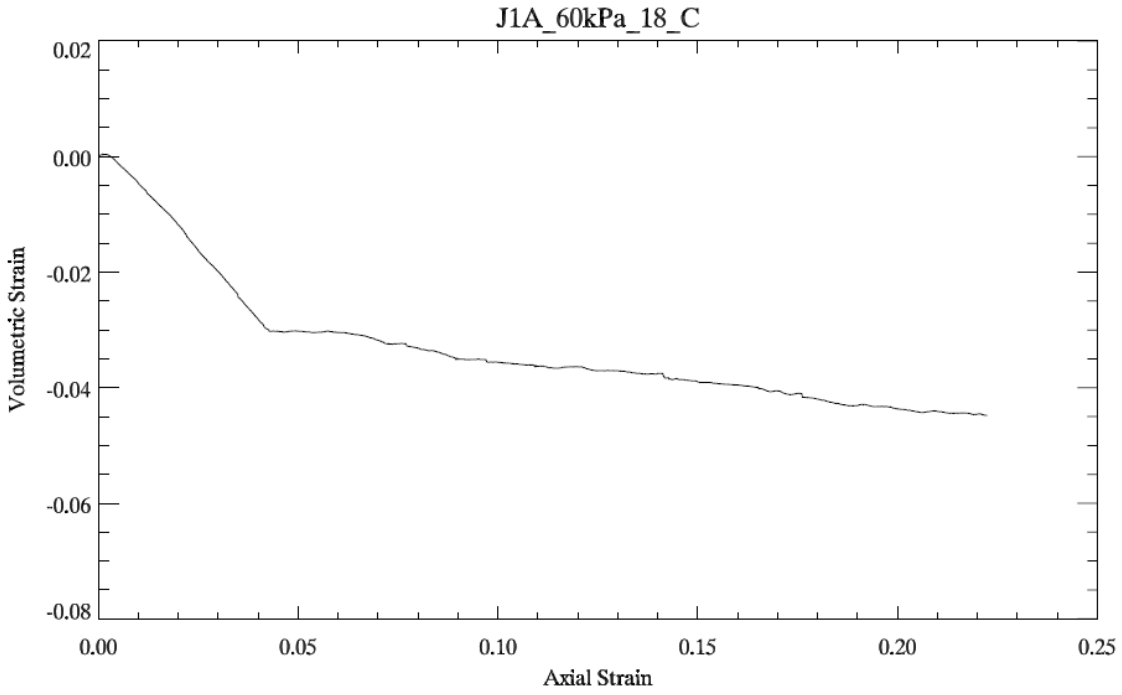

Figure C-14. Volumetric behavior for density of 1.8 g/cm^3 at 60 kPa confining stress

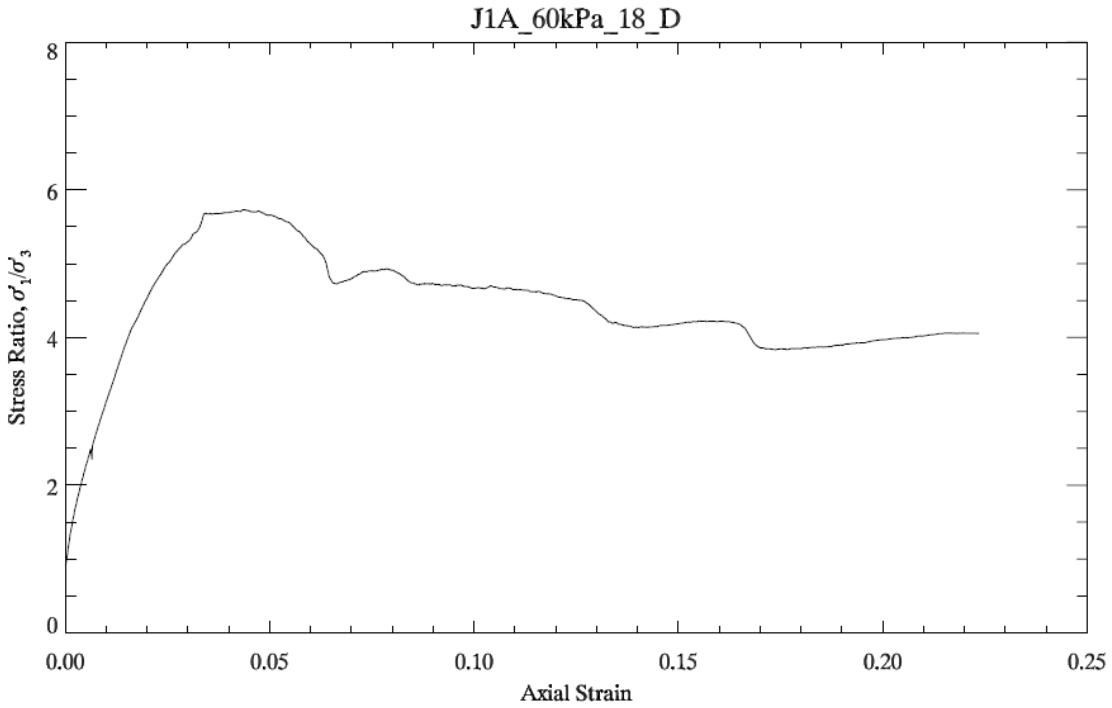

Figure C-15. Behavior of stress ratio as a function of axial strain for density of 1.8 g/cm^3 at 60 kPa confining stress.

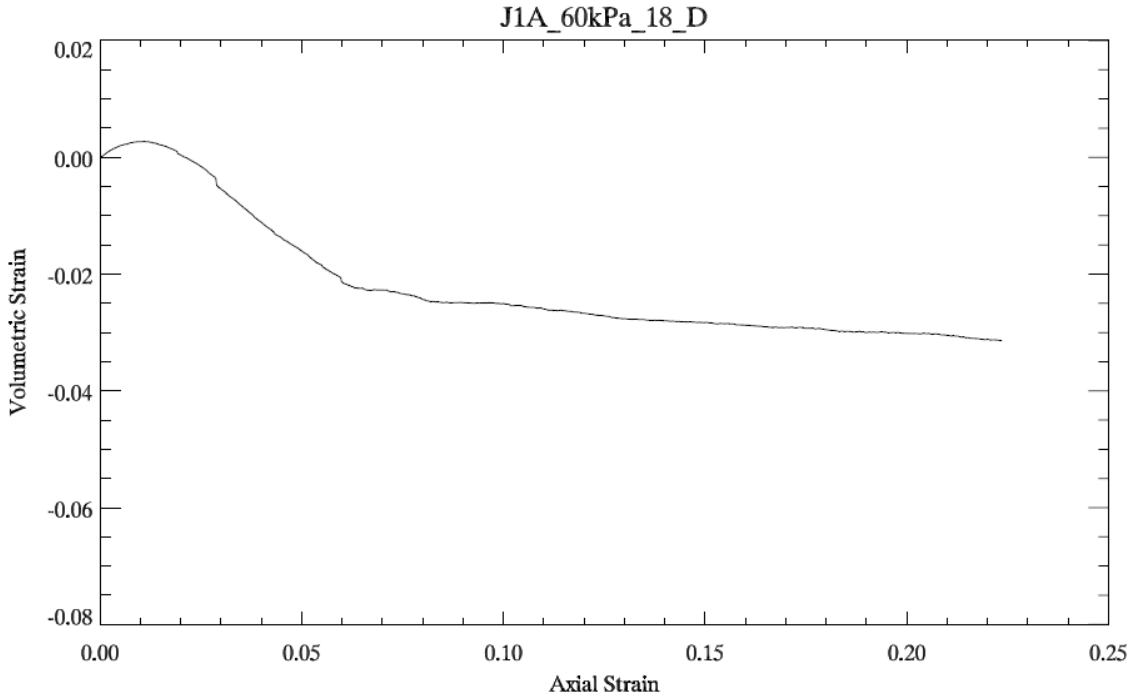

Figure C-16. Volumetric behavior for density of 1.8 g/cm^3 at 60 kPa confining stress

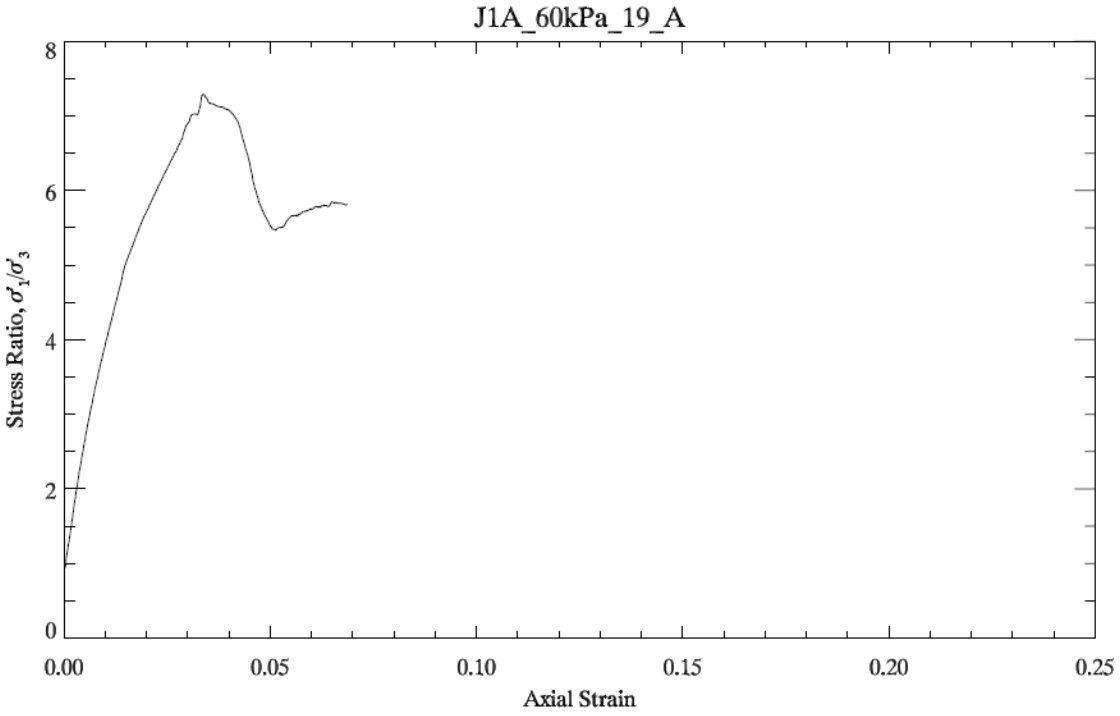

Figure C-17. Behavior of stress ratio as a function of axial strain for density of 1.9 g/cm^3 at 60 kPa confining stress.

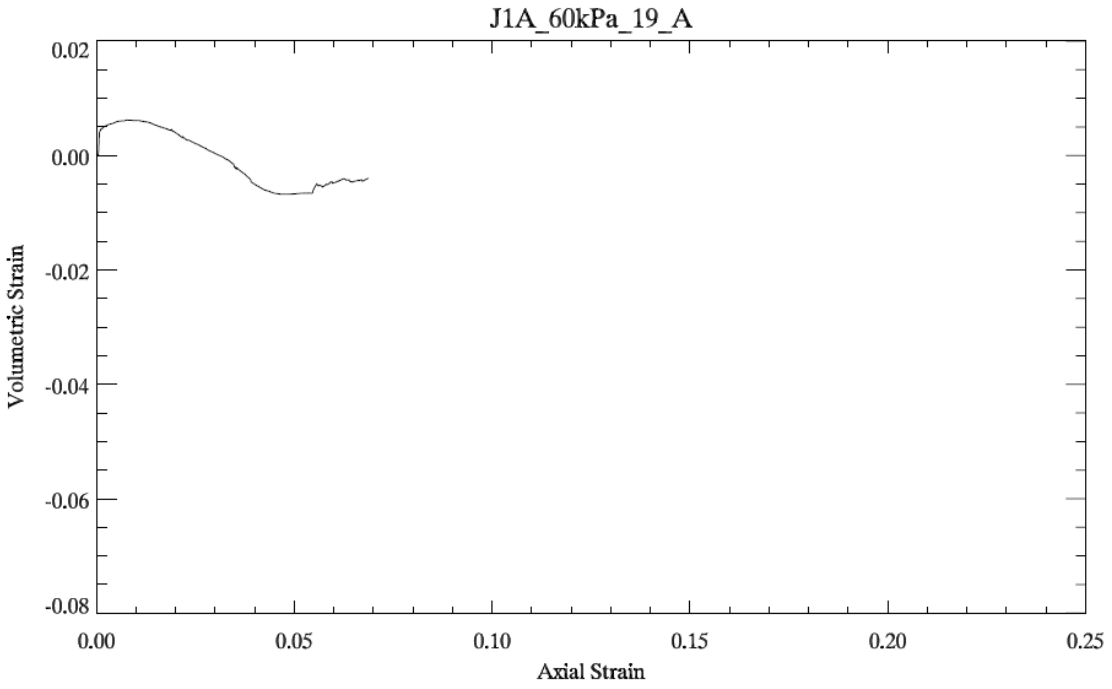

Figure C-18. Volumetric behavior for density of 1.9 g/cm^3 at 60 kPa confining stress

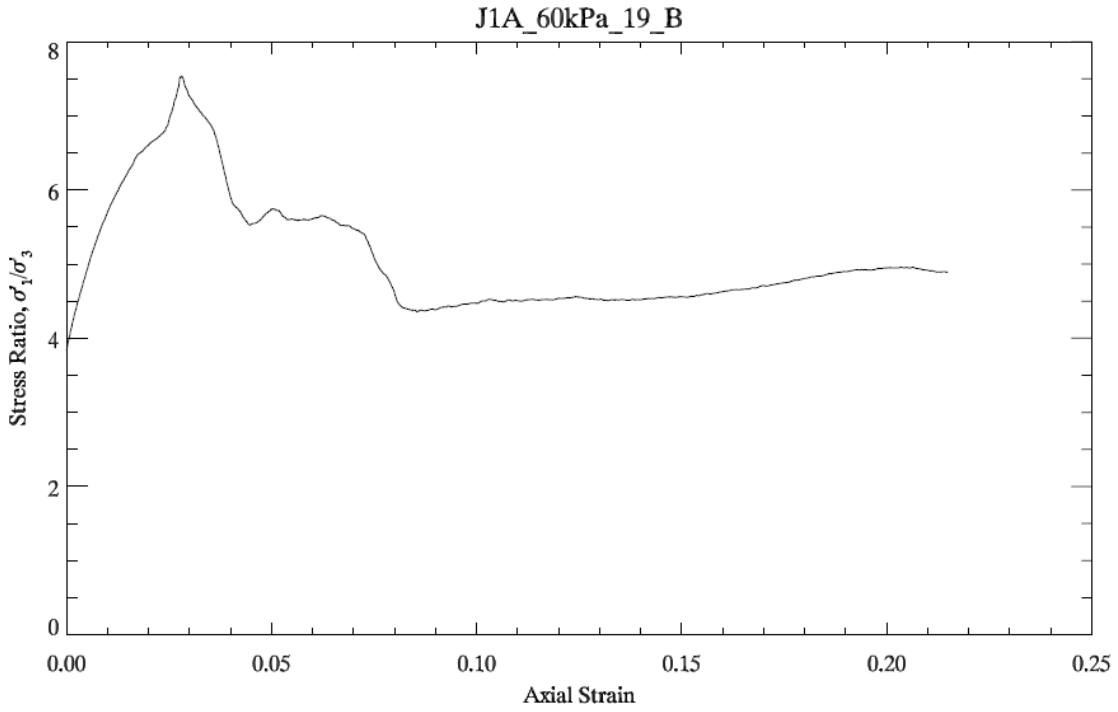

Figure C-19. Behavior of stress ratio as a function of axial strain for density of 1.9 g/cm^3 at 60 kPa confining stress.

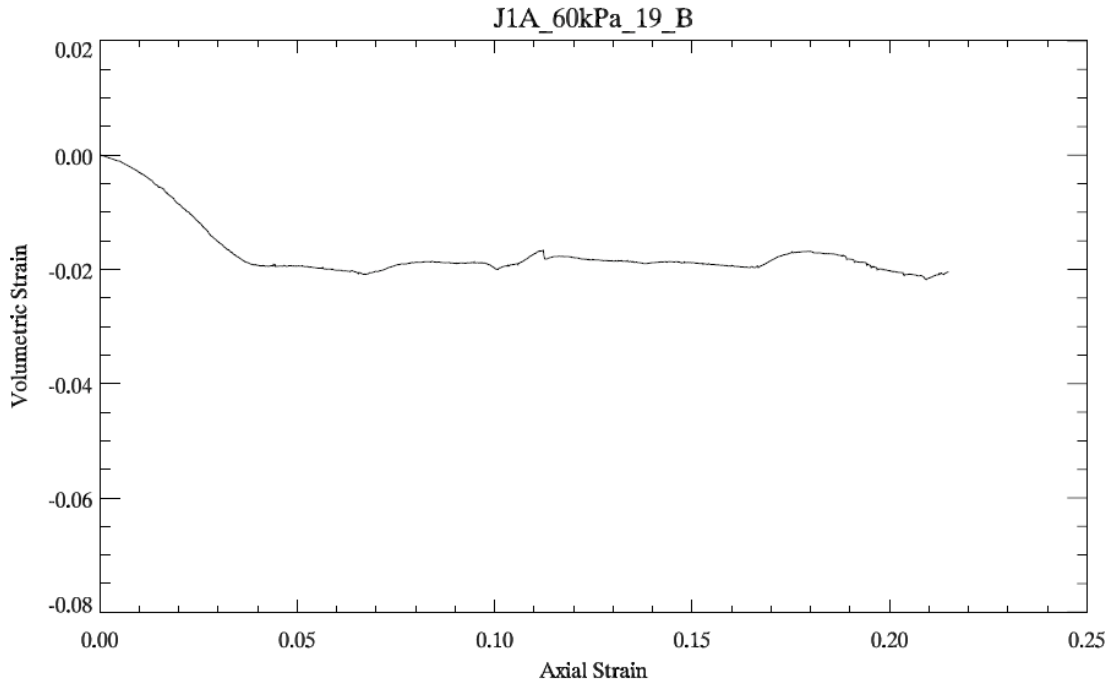

Figure C-20. Volumetric behavior for density of 1.9 g/cm^3 at 60 kPa confining stress

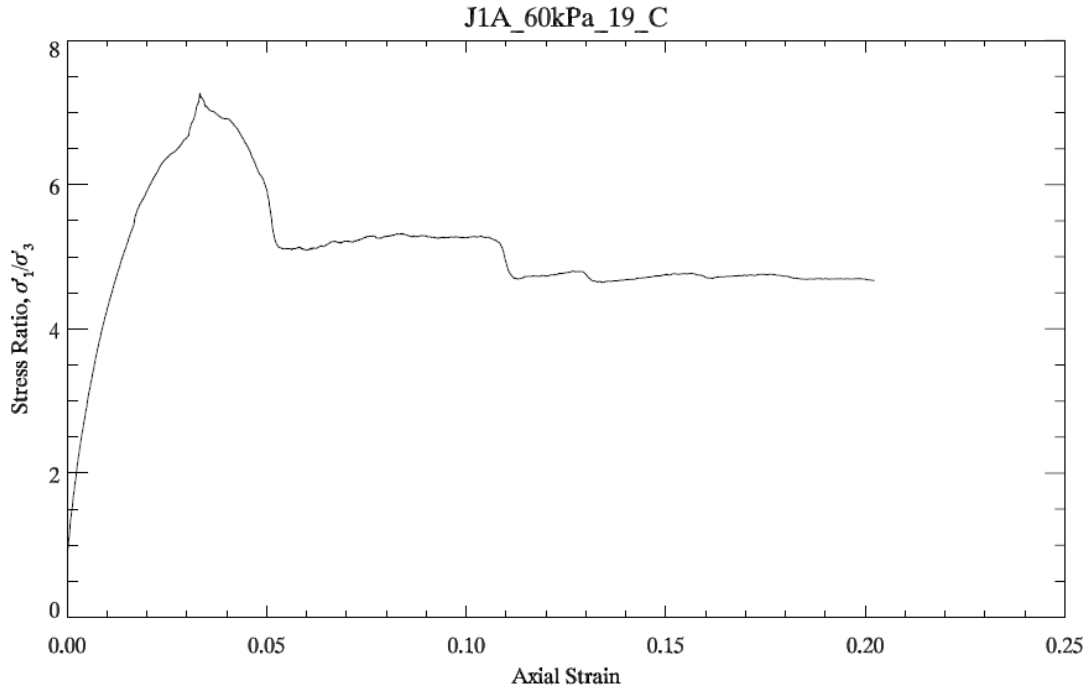

Figure C-21. Behavior of stress ratio as a function of axial strain for density of 1.9 g/cm^3 at 60 kPa confining stress.

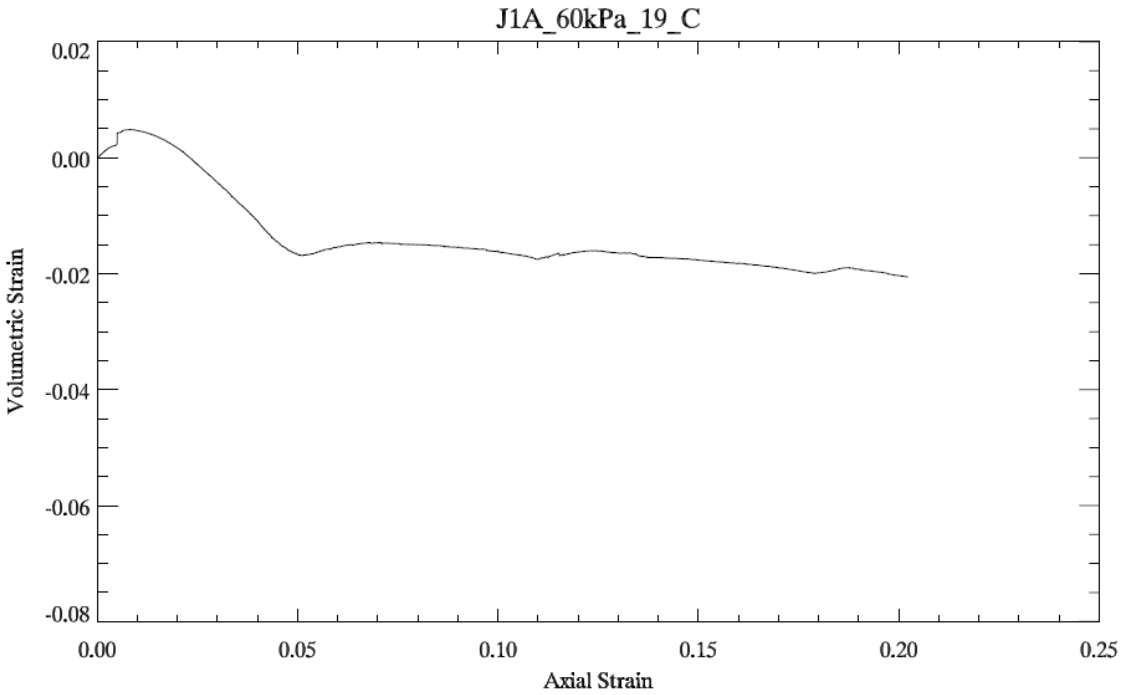

Figure C-22. Volumetric behavior for density of 1.9 g/cm^3 at 60 kPa confining stress

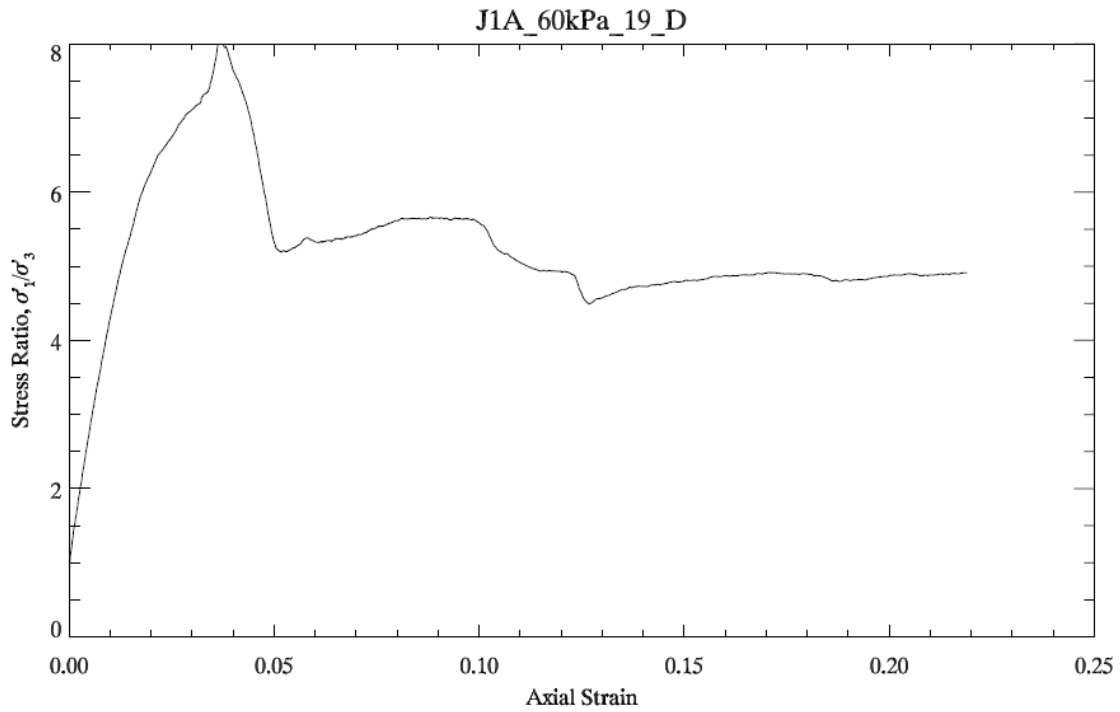

Figure C-23. Behavior of stress ratio as a function of axial strain for density of 1.9 g/cm^3 at 60 kPa confining stress.

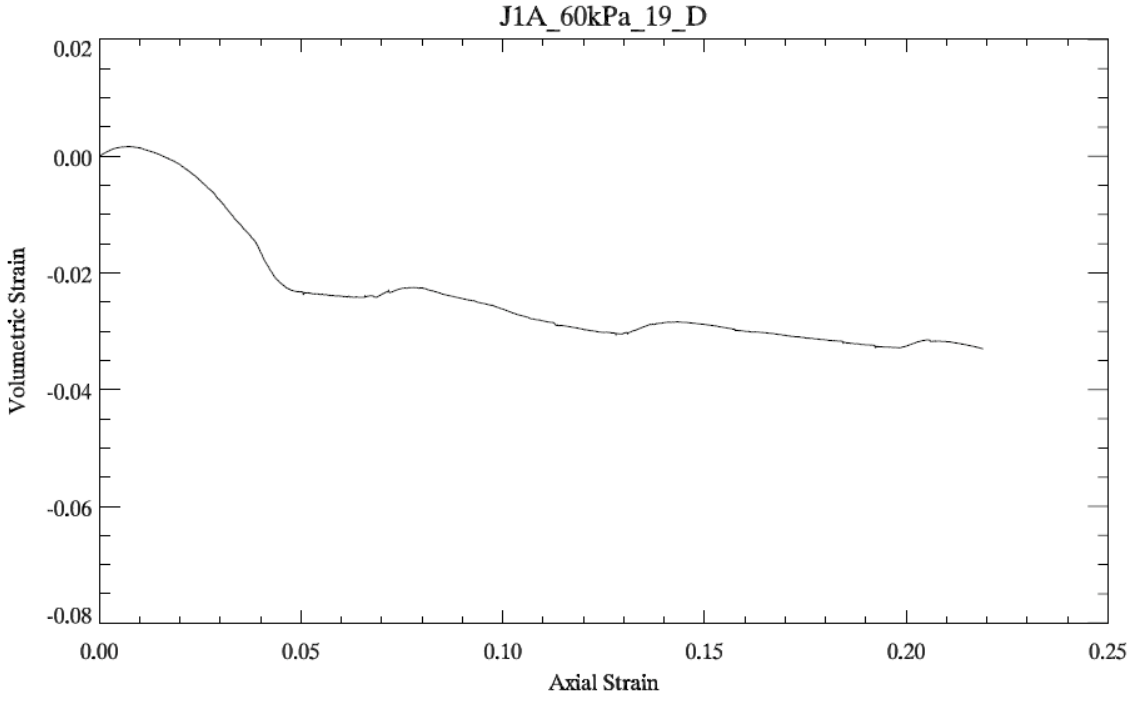

Figure C-24. Volumetric behavior for density of 1.9 g/cm^3 at 60 kPa confining stress

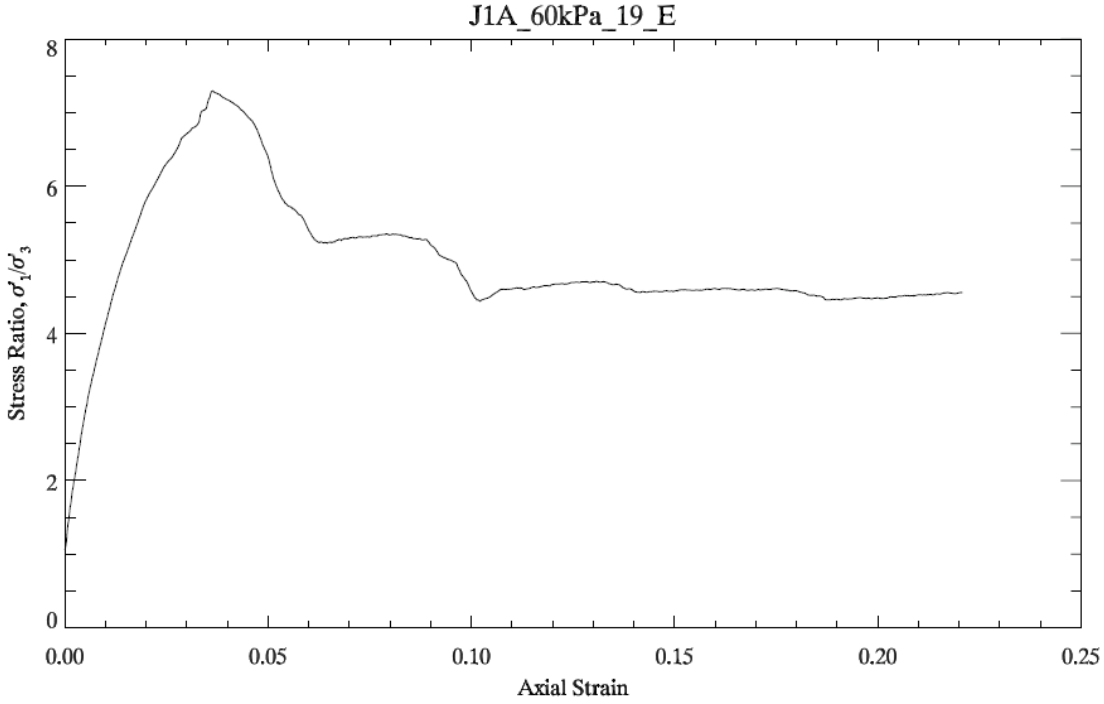

Figure C-25. Behavior of stress ratio as a function of axial strain for density of 1.9 g/cm^3 at 60 kPa confining stress.

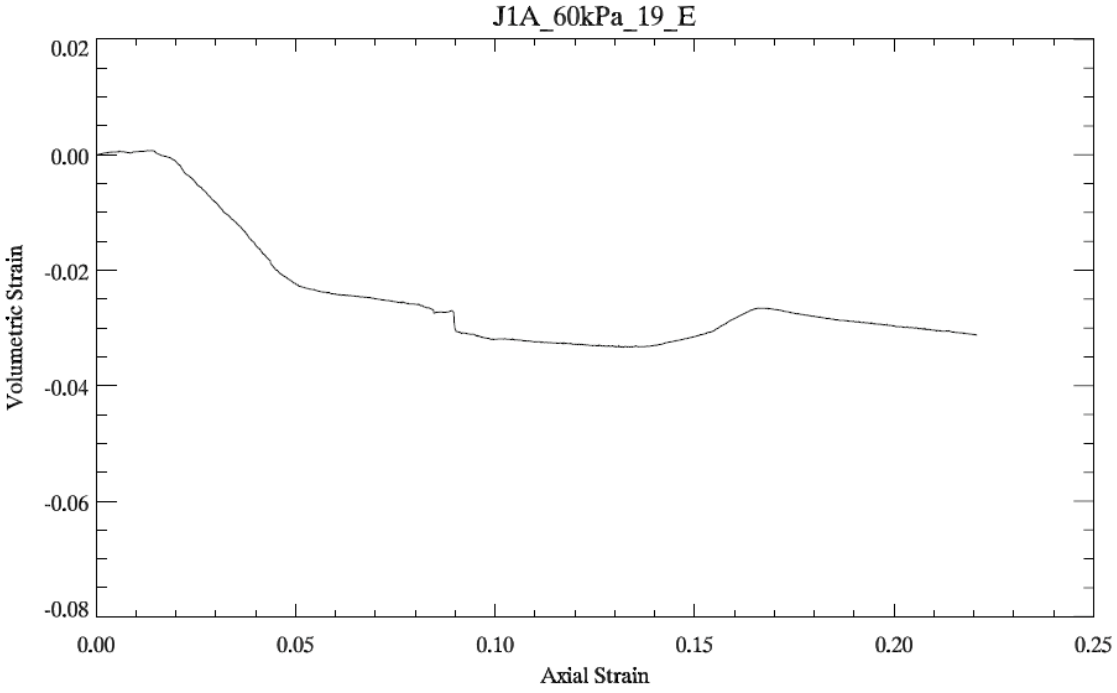

Figure C-26. Volumetric behavior for density of 1.9 g/cm^3 at 60 kPa confining stress

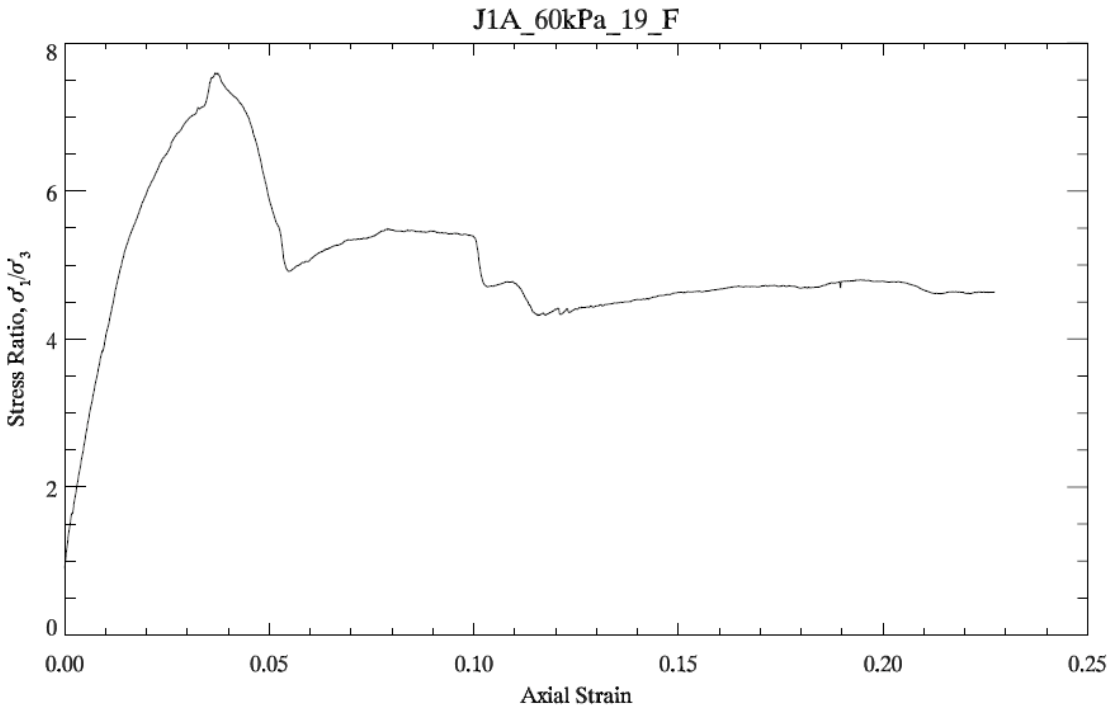

Figure C-27. Behavior of stress ratio as a function of axial strain for density of 1.9 g/cm^3 at 60 kPa confining stress.

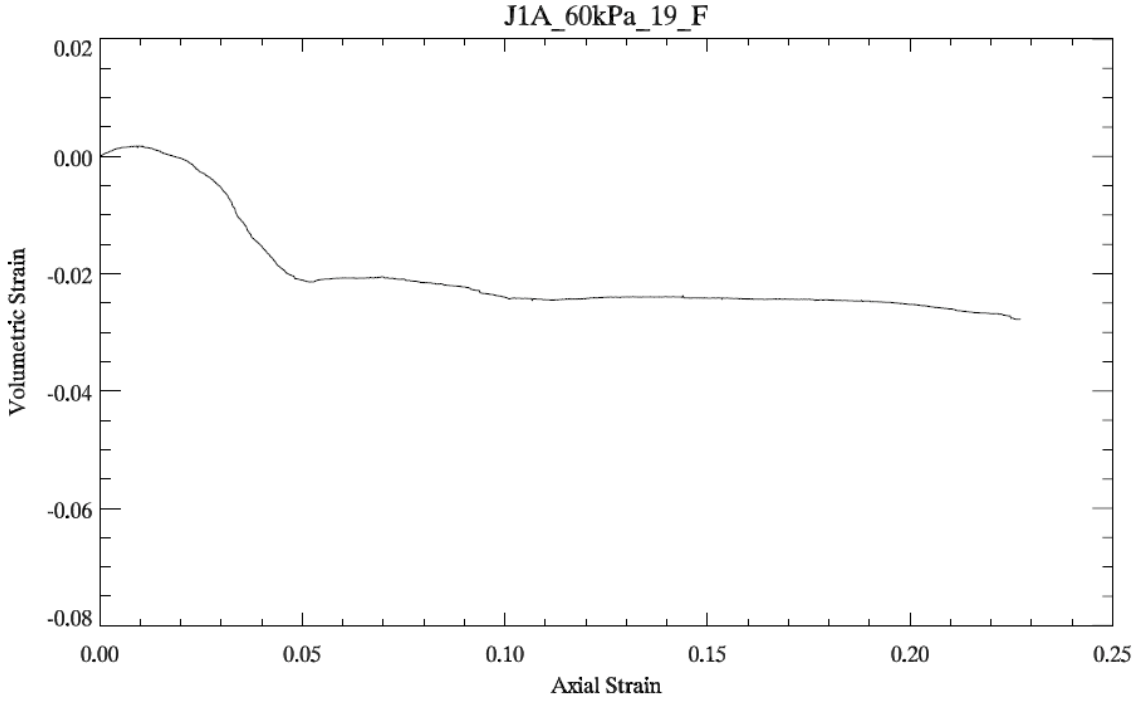

Figure C-28. Volumetric behavior for density of 1.9 g/cm^3 at 60 kPa confining stress

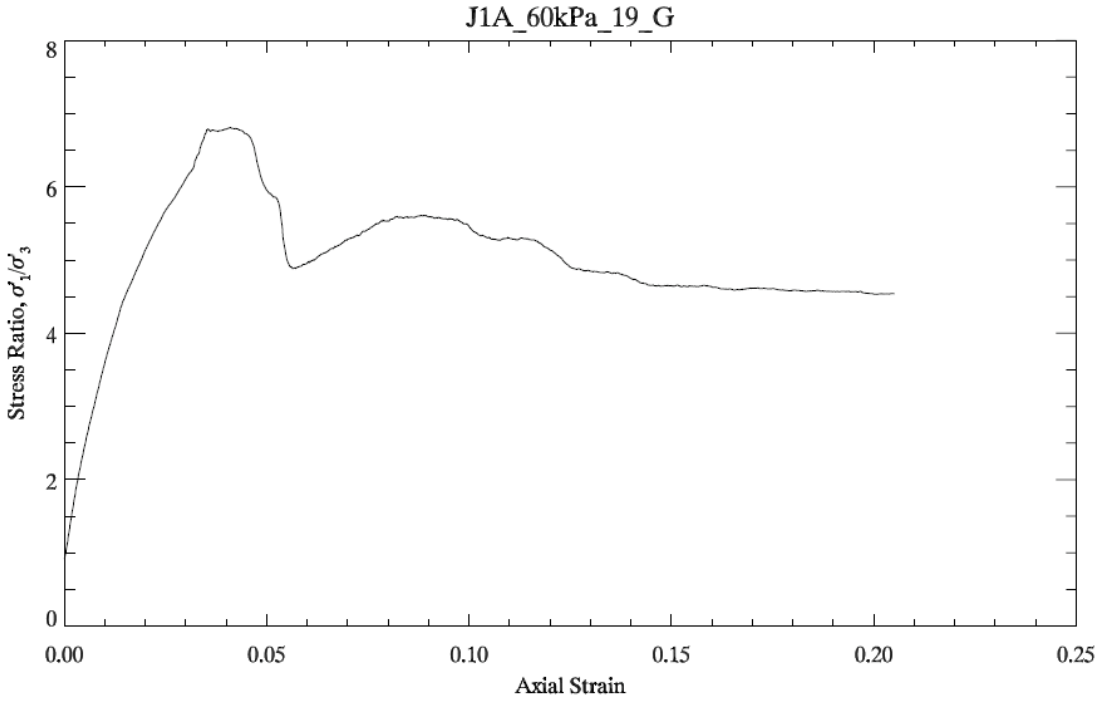

Figure C-29. Behavior of stress ratio as a function of axial strain for density of 1.9 g/cm^3 at 60 kPa confining stress.

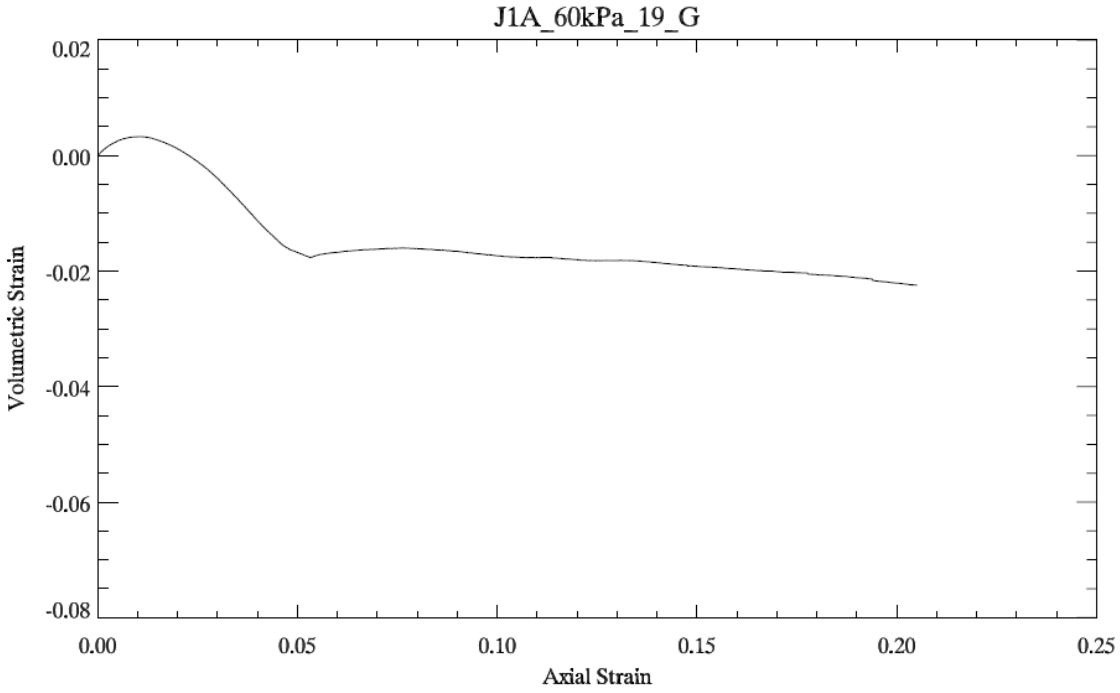

Figure C-30. Volumetric behavior for density of 1.9 g/cm^3 at 60 kPa confining stress